University of Groningen

Self-assembly, structure, and optical properties of molecular aggregates

Haverkort, Frank

IMPORTANT NOTE: You are advised to consult the publisher's version (publisher's PDF) if you wish to cite from it. Please check the document version below.

Document Version
Publisher's PDF, also known as Version of record

Publication date:
2014

Link to publication in University of Groningen/UMCG research database

Citation for published version (APA):
Haverkort, F. (2014). *Self-assembly, structure, and optical properties of molecular aggregates*. [S.n.].

Copyright
Other than for strictly personal use, it is not permitted to download or to forward/distribute the text or part of it without the consent of the author(s) and/or copyright holder(s), unless the work is under an open content license (like Creative Commons).

The publication may also be distributed here under the terms of Article 25fa of the Dutch Copyright Act, indicated by the “Taverne” license. More information can be found on the University of Groningen website: https://www.rug.nl/library/open-access/self-archiving-pure/taverne-amendment.

Take-down policy
If you believe that this document breaches copyright please contact us providing details, and we will remove access to the work immediately and investigate your claim.

Downloaded from the University of Groningen/UMCG research database (Pure): http://www.rug.nl/research/portal. For technical reasons the number of authors shown on this cover page is limited to 10 maximum.

Download date: 04-06-2022

Self-assembly, Structure, and Optical Properties of Molecular Aggregates

Zernike Institute PhD thesis series 2014-20
ISSN: 1570-1530

ISBN: 978-90-367-7270-9 (printed version)
ISBN: 978-90-367-7269-3 (electronic version)

The work described in this thesis was performed at the Zernike Institute for Advanced Materials and the Centre for Theoretical Physics of the Rijksuniversiteit Groningen.

Printed by Ipskamp Drukkers

rijksuniversiteit
groningen

Self-assembly, Structure, and Optical Properties of Molecular Aggregates

Proefschrift

ter verkrijging van de graad van doctoraat aan de
Rijksuniversiteit Groningen
op gezag van de
rector magnificus prof. dr. E. Sterken
en volgens besluit van het College voor Promoties.

De openbare verdediging zal plaatsvinden op

vrijdag 17 oktober 2014 om 11.00 uur

door

Frank Haverkort

geboren op 20 maart 1986
te Maastricht

Promotor
Prof. dr. J. Knoester

Copromotor
Dr. A. U. Stradomska-Szymczak

Beoordelingscommissie
Prof. dr. D. Beljonne
Prof. dr. M. A. Loi
Prof. dr. E. W. Meijer

Contents

Chapter 1

Introduction

1.1 Molecular aggregates

Molecular aggregates are assemblies of molecules that are held together by non-covalent forces, such as van der Waals forces, electrostatic forces, $\pi-\pi$ interactions, hydrophobic interactions, or hydrogen bonds. When the assembled molecules are dyes, the resulting structures acquire special optical properties, which are fundamentally different from those of the single dye molecule [1, 2]. The origin of these special optical properties lies in the creation of delocalized electronic excitations, called Frenkel excitons [3, 4]. Frenkel excitons occur in materials with a small dielectric constant, so that weak screening causes the Coulomb force between the electron and the hole to be strong, and a weak electron orbital overlap between neighboring molecules. The result is a tightly bound electron-hole pair with a spacing between electron and hole that is smaller than the intermolecular distance. On the other hand, in materials with larger dielectric constants and orbital overlaps, such as semiconductors, the electron and hole are located on different molecules; this type of excitation is called either a charge transfer exciton (when the separation between electron and hole is at most a few lattice spacings) or a Wannier exciton (when the separation corresponds to a large number of lattice spacings). Experimentally, molecular aggregates are characterized by an absorption band that is shifted with respect to the monomer. Depending on the way the molecules are stacked in the aggregate and the resulting relative orientation of the molecular transition dipoles, the aggregates' absorption spectrum can be either redshifted with respect to the monomer (in this case we speak of a J-aggregate), or blueshifted (an H-aggregate).

Man-made dye aggregates are produced by the self-aggregation of synthetic dye molecules in solution. Indeed, the unexpected self-aggregation of a synthetic dye was how dye aggregates were independently discovered by Scheibe and Jelley in the 1930's. The direction of the self-aggregation process is highly dependent on the type of dye, the type of counterion (if the dye is charged), dye concentration, temperature, the type of solvent, and the method by which the starting solution is prepared. A great diversity of aggregates have been created in this way, and it is expected that a multitude of structures can be formed even for a single type of dye. The special optical properties of synthetic aggregates led to their application as sensitizers in traditional photography [5, 6]. Also, the nonlinear optical properties of these aggregates have been the extensively investigated [7–12]. In nature, aggregates of chlorophyll dyes play an essential role in the photosynthetic process of plants and light-harvesting bacteria [13–15]. Not only are the chlorophyll aggregates important for the absorption of sunlight, they also transport the resulting electronic excitation energy to the reaction center, where the electronic excitation is converted into chemical energy. Inspired by the discovery of natural light harvesting, the possibility of using molecular aggregates for artificial light harvesting is currently being investigated [16, 17]. In addition, molecular aggregates might also be used as building blocks for other nanoscale materials with optical functionality, with applications such as lasing [18, 19] and molecular wires [20, 21].

1.2 Aims of this thesis

There are still many open questions in the field of aggregates formed by synthetic dyes [1, 2]. We will discuss here the main questions that this thesis tries to answer. Our most fundamental lack of information concerns the shape of the aggregates and their internal structure, which is sometimes known, but often uncertain. For example, it is suspected that the most-studied dye, pseudo-isocyanine (PIC, see Figure 1.1a), can form multiple structures. In one experiment, electron microscopy images of shock-frozen aggregate specimens have revealed a tubular structure, but the microscope was not able to visualize the internal structure of the tubes [22]. In other experiments, it is unclear whether the PIC dyes self-aggregate into a tube, a linear aggregate of smaller diameter, or an altogether different structure. Since the aggregates' shape and internal structure determines the relative orientation of the molecular transition dipoles, which is central to the size and sign of the excitonic couplings, and thus to the optical and energy transport properties of the aggregates, knowing the structure will greatly aid our understanding of these properties. As an extension of the question of the aggregate structure, we can ask ourselves how

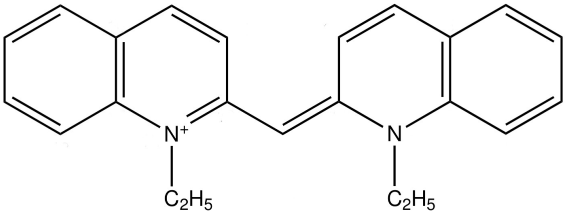

(a) The PIC dye.

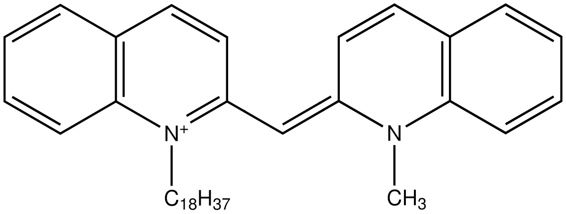

(b) The amphi-PIC dye.

Figure 1.1: The two dye molecules studied in this thesis: (a) pseudo-isocyanine (PIC), and (b) its amphiphilic derivative amphi-pseudoisocyanine (amphi-PIC).

much structural variation the aggregates exhibit, and whether this structural variation shows dynamics. A second question, connected to that of the aggregate structure, concerns the molecular transition energies and the excitonic couplings, which together determine the nature of the excitonic states. As is the case for the aggregate structure, knowledge of the transition energies and the couplings varies greatly from aggregate to aggregate. Thirdly, the details of the self-aggregation process are far from clear. For example, it is mostly not known which kind of structures are formed as intermediaries between the monomer and the aggregate.

In this thesis, we use first-principles simulations to find answers to some of the questions posed above. These simulations are an important addition to the more traditional approaches of experiments and phenomenological modeling. The first step of our first-principles approach is to use classical molecular dynamics (MD) simulations to obtain the aggregate structure; this can be done either through simulations of the self-aggregation process or by initializing the MD simulation with a model structure, obtained either from phenomenological models that are fitted to experimental data or guessed from another source, for example from a crystal structure. As a next step, the structures obtained from MD simulation are used as an input for quantum-chemical calculations of the molecular transition energies and the excitonic couplings, which are the parameters of our exciton Hamiltonian. In the end, we have gained knowledge of the time-dependent Hamiltonian of the Frenkel excitons in the aggregate, which can be used to simulate and understand the aggregate's optical and energy transport properties.

Of course, our first-principles approach assumes that it is possible to perform accurate, large-scale molecular dynamics simulations of dye aggregates, as well as quantum-chemical simulations of the parameters of these aggregates' exciton Hamiltonian. Therefore, an important secondary aim of this thesis is to determine whether such MD and quantum-chemical simulations can be accurately performed. It is well-established that there are quantum-chemical methods, for calculating molecular transition energies and excitonic couplings, that are accurate and computationally cheap enough to treat relatively small structures of about 20 dyes [23, 24]; we need to demonstrate that these methods can also be applied to considerably larger systems. On the other hand, performing molecular dynamics simulations of dye aggregates or their self-aggregation process is a much more formidable task. One reason is that the aggregate structure is determined by the interplay of several types of forces, and is very sensitive to the balance between these forces; this places high demands on the accuracy of the force field. A second reason is that current force fields were not designed to simulate dye molecules, but are mostly aimed at biomolecules such as proteins, lipids and nucleic acids; in addition, current force fields were not designed to reproduce optical properties. Finally, experiments show that the self-aggregation process can take minutes, a time scale that is extremely long in the context of MD simulations; ways must thus be found to speed up the MD simulations, such as using artificially high dye concentrations. Taken together, these challenges present conflicting requirements: on the one hand a more accurate force field is needed, but this force field will then necessarily be more computationally expensive; on the other hand, the longer time spans and larger systems need to be simulated, but the required computationally cheaper force field will be less accurate as a result.

In this thesis, two distinct force fields were chosen which form the best compromise between speed and accuracy. In Chapters 2 and 3, we used a modification of the GROMOS force field, which includes polarization in an implicit manner (through the other forces) and is thus relatively cheap computationally. In Chapter 4, we used a modification of the relatively accurate CHARMM Drude force field, which describes electronic polarization in an explicit manner. These force fields gave results of varying accuracy. Using the

CHARMM Drude force field, we succeeded in accurately simulating the initial steps of the self-aggregation process of the dye pseudo-isocyanine, as we verified by comparing the absorption spectrum of the self-aggregated dimer to experiment. However, both force fields were unable to provide a structure for the molecular aggregate that was compatible with spectroscopic measurements, although for an amphiphilic derivative of the PIC chromophore, the GROMOS force field provided us with two realistic candidates for aggregate shapes and structures.

1.3 Thesis overview

In Chapter 2, we investigate the structure of aggregates of the amphi-PIC dye (depicted in Figure 1.1b), which is an amphiphilic relative of the well-known PIC dye. We perform molecular dynamics simulations of the self-aggregation process, starting with dye molecules randomly placed in water. In these simulations, a cylindrical aggregate forms, with the hydrocarbon tails of the amphi-PIC dyes in the center, shielded from the water. The walls of the cylinder consist of a very disordered stacking of amphi-PIC headgroups, with only irregular $\pi - \pi$ stacking. When a simulated annealing procedure is applied in an attempt to induce a more orderly $\pi - \pi$ stacking, instead the cylinders widen into a ribbon-like shape. The very slow dynamics of these aggregates, compared to the time scales that are accessible in MD simulations, make it impossible to decide whether the cylindrical or ribbon-like state are the equilibrium MD structure. Finally, when acetate counterions are used instead of perchlorate, the self-aggregation process changes dramatically, resulting in the formation of micelles rather than cylinders.

Chapter 3 proceeds where Chapter 2 ends, and studies the excitonic states and optical properties of the molecular aggregates found in Chapter 2. We find the relevant time scales for the fluctuations of the molecular transition energies and the excitonic couplings, which underlie the aggregates' excitonic states; these time scales range from tens of femtoseconds to tens of picoseconds. The time scales of up to 100 fs can be attributed to the internal motions of the dye molecules, while the slower time scales are a result of environmental (solvent) motions. The absorption spectrum of both cylindrical and ribbon-shaped aggregates turns out to be almost identical, due to their large structural disorder. Their spectra carry considerable oscillator strength over the entire range of the exciton band, in addition to a relatively weak peak that is blueshifted with respect to the monomer absorption. Compared to experiment, the simulated lineshapes are much too wide, which can be attributed to too much disorder in the cylinder wall.

Chapter 4 studies the initial phase of the self-aggregation of the PIC dye (shown in Figure 1.1a). We perform molecular dynamics simulations of the self-aggregation process, starting with dye molecules randomly placed in a water solvent. The dyes then combine to form pile-of-coin stacks of up to about 20 molecules, which form the link between the monomer and large aggregates. Our pile-of-coin structures are corroborated by the favorable comparison of the dimer spectrum to experiment. We go on to study the structure and absorption spectrum of the formed dimers and trimers. The absorption spectra of the dimer and trimer are blueshifted with respect to the monomer, making them H-oligomers; their spectral structures can be understood as arising from the intermediate-strength coupling between the excitons and one dominant vibrational mode. All structures are found to be very flexible; for example, dimers are interchangeably orderly $\pi - \pi$ stacked state or more loosely coupled, with transitions between both forms occurring on a nanosecond time scale. The flexible nature of the dimers and trimers is found to make an important contribution to their absorption spectra. We also investigate candidate structures for the PIC aggregate by testing the stability of several model structures in MD simulation, but none of the tested structures is found to be stable.

In Chapter 5, we analyze exciton transport in a linear molecular aggregate. The focus is on the long-time behavior of this transport. More specifically, we analyze two methods to simulate exciton transport, which have their own advantages and disadvantages: the Numerical Integration of the Schrödinger Equation (NISE) method, and the Pauli Master Equation Approach (PMEA). A major advantage of the NISE method is that it is able to model both coherent and incoherent exciton motion, while a strong point of the PMEA is that it predicts the correct thermalization in equilibrium. We investigate the diffusion constant predicted by the NISE method, and find that diffusion is fastest for site transition energies with dynamic and static disorder components of the same order of magnitude. Also, the diffusion constant increases monotonically when the memory time of the dynamic disorder component is decreased. In contrast to the NISE method, which always predicts long-time diffusive motion, the PMEA is found to predict slightly subdiffusive motion at long times for a set of parameters that are realistic for a molecular aggregate. However, when increasing the amount of static disorder, the predicted transport becomes much more strongly subdiffusive.

Chapter 2

Investigating the structure of aggregates of an amphiphilic cyanine dye with molecular dynamics simulations[1]

We perform molecular dynamics (MD) simulations of the self-assembly process of pseudoisocyanine dye molecules with amphiphilic substituents (*amphi*-PIC). The spontaneous aggregation of cyanine molecules into large molecular J-aggregates with optical functionality has drawn attention for many decades already, but the shape and molecular structure of the aggregates remain issues of debate, as current imaging techniques still lack molecular scale resolution. Our MD simulations for *amphi*-PIC predict the existence of aggregates with the shape of either a single-walled cylinder or a ribbon. We characterize the internal structure of these aggregates using the π - π stacking and the average orientation of the long axis of the *amphi*-PIC molecule's chromophore. The molecular arrangement obtained exhibits much disorder, which may explain the wide absorption band observed for aggregates of *amphi*-PIC. We show that changing the counterion of the positively charged *amphi*-PIC dye can change the equilibrium aggregate shape. In addition, we demonstrate that the cylindrical aggregates attract each other and form bundles.

---

[1] This chapter is based on F. Haverkort, A. Stradomska, A. H. de Vries, and J. Knoester, *J. Phys. Chem. B* **117**, 5857 (2013)

2.1 Introduction

Self-assembly of molecules into large aggregates with specific functionalities is widely perceived as a promising method to prepare nanometer scale functional materials. Amongst such systems, assemblies of cyanine dye molecules take a special place. It has been known for a long time that in solution these molecules spontaneously form assemblies of many 1000's of molecules, referred to as J-aggregates, with interesting optical properties [25–30]. J-aggregates of cyanine molecules often exhibit very narrow optical lineshapes at tunable frequencies [31] and ultrafast spontaneous emission [32–34]. In addition, they may exhibit a strong nonlinear optical response [7–10, 35] and fast electronic energy transfer [36–38]. All these special properties arise from a close packing of the molecules within the assembly, which gives rise to strong dipole-dipole interactions between their optical transitions. This drives the creation of Frenkel excitons, collective excited states coherently shared by a (possibly large) number of molecules, as well as fast transport of the electronic excitation.

Owing to their strong optical transitions and their use in traditional photography [5, 6], cyanine molecules have historically drawn most attention in the field of optically active aggregates, but many other classes of synthetic dye molecules exhibit self-assembly (for instance, porphyrin derivatives [39], perylene bisimides [40] and merocyanines [41]). In addition, self-assembled structures of dye molecules play an essential role in Nature, in particular to form light-harvesting antennae of chlorophyll molecules in bacteria and higher plants [13, 15, 42–47].

The optical properties and excited state dynamics of both synthetic and natural dye molecules are studied in ever increasing detail. Lately, ultrafast two-dimensional optical spectroscopy has been added as a tool to get deeper insight into the molecular scale electronic processes in these systems [48–52]. In order to interpret these experiments and to inspire new experimental protocols as well as new design principles, it is essential to obtain a solid understanding of the structure-property relationships of molecular aggregates. Progress in this endeavor is hindered by a general lack of knowledge of the molecular arrangement within the aggregate. In some cases, the overall morphology of molecular aggregates has been revealed by (transmission) electron microscopy ((T)EM) [15, 53–59], but this technique lacks the resolution needed to image the molecular packing. Even for the best studied aggregates, those of the dye pseudo-isocyanine and its derivatives, it is not clear how this packing is [1]. This is remarkable, as the packing dominates the intermolecular interactions, which in turn drive all the special optical properties mentioned above. The current level of modeling of these properties necessarily consists of working with model structures that fit the overall morphology (if known at all) and where the packing is described by a number of parameters which are obtained by fitting predictions of the optical spectroscopy to experimental data. While this has led to remarkable successes [54, 59–64] and the prediction of intriguing phenomena of collective excited states (such as exciton superradiance [32] and quantum level repulsion [65, 66]), the call for more precise and predictive modeling requires molecular scale knowledge of the aggregate's structure.

In this chapter, we aim at initiating a new approach to obtain molecular scale structure of dye aggregates, namely molecular dynamics (MD) simulations of the spontaneous aggregation process. Molecular dynamics simulations have already been successfully used to simulate spontaneous aggregation of lipid bilayers [67, 68]. Although such simulations of large systems are hard, we believe that with current MD methods and computer power, MD simulations form a promising tool to reveal the internal structure of aggregates of dye molecules, in particular if its outcomes are used in combination with spectroscopic modeling [69, 70].

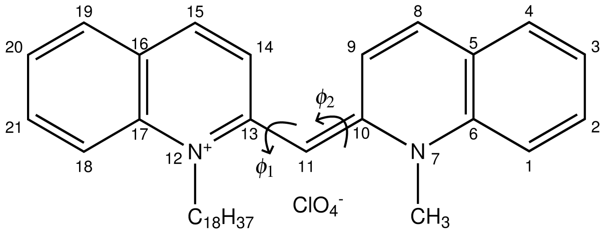

Figure 2.1: The *amphi*-PIC cation with its perchlorate counterion. Also shown are the dihedral angles ϕ_1 and ϕ_2 (defined in section 2.2.1), and the numbering of the atoms in the PIC moiety (used for analysis).

We have chosen to study aggregates of the amphiphilic cyanine dye 1-methyl-1'-octadecyl-2,2'-cyanine perchlorate, also known as *amphi*-pseudoisocyanine (*amphi*-PIC, see Figure 2.1). This dye is very similar to the well-known PIC dye, the only difference being in the two hydrocarbon tails. The headgroup of the *amphi*-PIC molecule is 1.4 nm long and its $C_{18}H_{37}$ tail has a length of 2.6 nm (when fully stretched). Several microscopic images of *amphi*-PIC aggregates exist. Cryo-TEM images at relatively high *amphi*-PIC concentrations show double-walled cylinders and spherical aggregates [55]. Malyukin *et al.* recently also reported a TEM image obtained at low dye concentration and interpreted their data as single-walled cylindrical aggregates [71]. While the latter images may also have been crystals formed by the contrast agent [72], the formation of tubular aggregates in itself is a logical option for aggregates of amphiphilic dye molecules where the hydrophobic side groups should be shielded from the water solvent, either by placing them in the interior of a structure (single-walled tubes or spherical micelles), or between two layers (bilayers or double-walled tubes). Aggregates of tubular morphologies have attracted much attention lately; double-walled aggregates have been observed and studied with a variety of spectroscopic tools for another amphiphilic cyanine dye molecule 3,3'-bis(2-sulphopropyl)-5,5',6,6'-tetrachloro-1,1'-dioctylbenzimidacarbocyanine, known as C8S3 [16, 54, 56, 59, 73, 74], single-walled aggregates are formed by the porphyrin derivatives meso-tetra(4-sulfonatophenyl)porphyrin (TPPS4) [58, 75–78], while it seems that multilayered tubular aggregates of bacteriochlorophyll exist in the light-harvesting systems of green sulphur bacteria [15]. We have chosen to study aggregates of the *amphi*-PIC dye because the optical and energy transport properties of these aggregates have been extensively studied in recent years [55, 71, 79].

The outline of this chapter is as follows. In section 2.2, we design the force field for *amphi*-PIC and describe the MD simulations. Section 2.3 discusses the results of the MD simulations. In particular, subsection 2.3.1 deals with the global aggregate structure, 2.3.2 with the internal order of the aggregates, 2.3.3 investigates the effects of using an acetate instead of a perchlorate counterion, and 2.3.4 deals with the bundling of cylindrical aggregates. Finally, we summarize and conclude in section 2.4.

2.2 Computational details

2.2.1 Force field parametrization

The force field used for the *amphi*-PIC molecules was based on GROMOS53A6 [80] and differs from it in two ways. Firstly, since the standard version of GROMOS53A6 lacks specific parametrization for the twisting around the central bond of the *amphi*-PIC molecule, potential energy terms were added to it for the two dihedral angles ϕ_1 and ϕ_2, defined by atoms 10-11-13-14 and 13-11-10-9, respectively (see Figure 2.1). Secondly, the atomic charges of the *amphi*-PIC molecule were based on the results of the quantum chemical CHELPG method [81], which fits the charges to represent the molecular electrostatic potential (for details, see Appendix 2.5). For the perchlorate ion, atomic charges and equilibrium bond lengths were taken from Cadena et al. [82]. For the water molecules, the SPC water model was used [83].

The additional potential energy terms for parameterizing the central bond of the *amphi*-PIC molecule were determined by fitting the force field potential energy surface to the results of quantum chemical calculations. We consid-

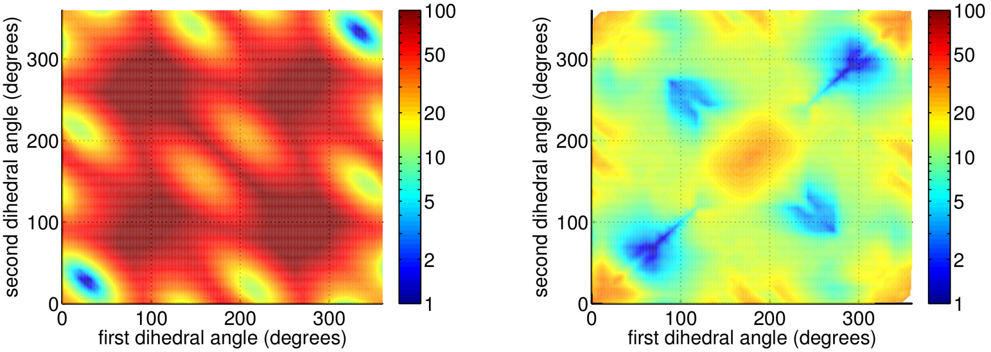

(a) quantum chemistry

(b) standard force field

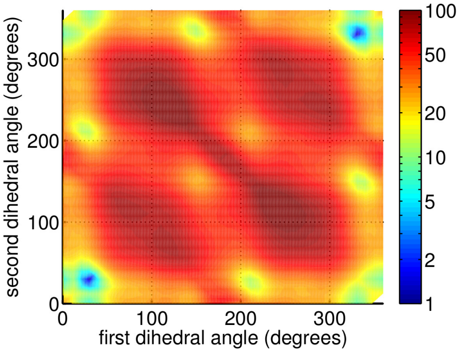

(c) modified force field

Figure 2.2: The potential energy surface as a function of two dihedral angles of the *amphi*-PIC molecule, calculated using (a) the quantum chemical DFT method, (b) the GROMOS53A6 force field, and (c) the GROMOS53A6 force field with extra energy terms, given in Eq. 2.1, which were fitted to reproduce the quantum chemical results. Energy scale in kJ mol^{-1}, with the lowest energy value of each plot set to 1 kJ mol^{-1}.

ered a simplified (symmetrized) model of the *amphi*-PIC molecule, with the $C_{18}H_{37}$ tail replaced by a methyl group. All calculations were done for a single molecule in the gas phase. The reference data, to which the force field was fitted, was a two-dimensional potential energy surface, where for each point on the surface the two dihedrals, ϕ_1 and ϕ_2, were constrained and the other molecular coordinates were obtained from an energy minimization calculation (see Figure 2.2a). These calculations were performed using density functional theory, with the B3LYP functional [84, 85] and Pople's 6-31G* basis set, as implemented in the QChem program version 3.2 [86]. In the force field calculations, dihedral angles were restrained using a harmonic restraint force with a force constant of $500\,\mathrm{kJ\,mol^{-1}\,nm^{-2}}$.

The added potential function was chosen to have the form of a sum of cosines $U(\phi_1, \phi_2) = \sum_{n=1}^{\infty} a_n(\cos(n\phi_1) + \cos(n\phi_2))$, because this function has the required periodicity in 360° and has the same symmetries as the simplified *amphi*-PIC molecule. Furthermore, a potential of this form can be easily added to the GROMOS force field in the form of a proper dihedral energy term.

The fitting was performed in two steps. First, an estimate for the additional energy terms was obtained from a series of geometry optimization calculations in which only one of the dihedrals was fixed. The resulting one-dimensional potential energy surface made the fitting procedure much easier than if the two-dimensional energy surface (i.e. dependent on both dihedrals) was used. In the second step, the additional energy terms were verified in a series of geometry optimization calculations in which both dihedrals were fixed, yielding the potential energy surface as a function of both dihedral angles (see Figure 2.2).

During the fitting procedure it turned out that it was sufficient to use three potential energy terms per dihedral, with estimated periods n. The coefficients a_n were varied until a good fit to the quantum chemical potential energy surface was obtained. By comparing the quantum mechanical and force field potential energies as a function of the dihedral angle, we added the following potential energy function to the force field potentials to best reproduce the quantum chemical potential,

$$\begin{aligned} U(\phi_1, \phi_2)/(\mathrm{kJ\,mol^{-1}}) = {} & -1.5\cos(\phi_1) - 30\cos(2\phi_1) + 3\cos(6\phi_1) \\ & -1.5\cos(\phi_2) - 30\cos(2\phi_2) + 3\cos(6\phi_2). \end{aligned} \tag{2.1}$$

As a result of this additional term, the global minimum of the potential energy surface is shifted from $(\phi_1, \phi_2) = (63.2°, 63.3°)$ to $(\phi_1, \phi_2) = (27.6°, 27.7°)$, close to the quantum chemical result of $(\phi_1, \phi_2) = (27.0°, 27.0°)$. Moreover, the width of the global energy minimum, as well as the position and relative energies of the other minima are also approximated reasonably well (see Figure 2.2). For additional details on the force field parametrization, see Appendix 2.6.

2.2.2 Molecular dynamics

Our system consisted of an equal number of positive *amphi*-PIC and negative perchlorate or acetate ions (see Figure 2.1), typically of the order of 100, in

sim.	number of *amphi*-PICs	number of waters	box size x (nm)	box size y (nm)	box size z (nm)	simulation time (ns)
1	160*	17 890	10.2	10.2	6.8	660
2	80	8953	9.0	9.0	4.3	194
3	180	6312	5.7	5.7	11.3	534
4	90	41 260	11.1	11.1	11.1	185
5	160*	17 890	14.0	14.0	3.6	781
6	160*	14 000	12.0	12.0	4.0	235
7	80	9142	7.1	7.1	7.1	298
8	320*	51 360	16.5	16.5	6.9	248

Table 2.1: Simulation details: number of *amphi*-PIC molecules (equal to the number of counterions) and number of water molecules in the simulation box, the box size in x-, y- and z-directions, and the simulation time. The given values refer to the end of each simulation.

* Because of a duplication of the simulation box, the final number of molecules given here is twice the initial number.

water. Initial configurations were created by placing *amphi*-PIC ions and the counterions in a simulation box with a random position and orientation, and then filling the remaining space with water molecules. Periodic boundary conditions were used for the box. Out of the tens of MD simulations that were performed, eight representative simulations are presented in this chapter; their parameters are given in Table 2.1 (see Appendix 2.8 for an overview of all performed simulations). The eight simulations presented here were started in a cubic box with 7 nm sides, except for simulation 4, which started in an 11 nm box. All eight simulations contained perchlorate counterions, except for simulation 7, for which acetate counterions were used. The molecular dynamics simulations were performed using the GROMACS program [87]. Newton's equations of motion were integrated using the leapfrog algorithm [88], with a time step of 2 fs. We used an atomistic description, except for the CH_3 and $C_{18}H_{37}$ side groups of the *amphi*-PIC molecules, where the basic building blocks were CH_2 and CH_3 groups.

The LINCS method [89] was applied to constrain all bond lengths. The non-bonded interactions were calculated using a twin-range cutoff scheme. All Lennard-Jones and electrostatic interactions within the short-range cutoff distance of 0.9 nm were evaluated at each time step, based on a pair list recalculated every 5 steps. The Lennard-Jones and electrostatic interactions within the long-range cutoff of 1.4 nm were calculated simultaneously with each pair list update and assumed constant in between. Electrostatic interactions beyond the 1.4 nm cutoff radius were corrected with a reaction field potential, with a relative electric permittivity ϵ_r of 54 [90].

The *amphi*-PIC molecules on the one hand, and the water molecules and counterions on the other, were coupled separately to a heat bath, using a Berendsen thermostat [91] with a relaxation time of 0.1 ps. The temperature was kept constant at 298 K, except in simulations 5 and 6. Simulation 5 used the configuration of simulation 1 at 557 ns as a starting point. Twenty simulated annealing cycles with a period of 10 ns were performed. In each cycle, the temperature was increased from 298 K to 400 K in 100 ps, then kept constant for 400 ps, subsequently lowered back to 298 K in 6.5 ns, and finally kept constant for 3 ns. Simulation 6 started at 400 K; after the aggregation had taken place, the temperature was linearly reduced to 298 K in 50 ns.

For the pressure coupling the Berendsen scheme [91] was used, with a reference pressure of 1 bar in all directions and a relaxation time of 0.5 ps. Runs started with a compressibility of 4.6×10^{-6} bar^{-1}, which was changed to 4.6×10^{-5} bar^{-1} after equilibration. All simulations were started with isotropic pressure coupling, and in simulations 4 and 7 the pressure coupling remained isotropic for the entire simulation. In the other simulations, semi-isotropic pressure coupling was applied after an aggregate had formed, so that the box side(s) through which the aggregate was connected to its periodic image were separately coupled to a pressure bath. After semi-isotropic pressure coupling was switched on, the aggregates contracted in the direction in which they were attached to their periodic image, making the box shorter in this direction. To prevent a small box dimension from causing boundary effects, the simulation box was duplicated in the shortened direction in simulations 1, 5, 6, and 8.

The starting point of simulation 8 was a simulation box containing two cylindrical aggregates. It was obtained by duplicating the configuration of simulation 1 at 350 ns in both directions perpendicular to the cylinder axis, and then removing two of the cylinders so that two remained. To save computational time, about a quarter of the water molecules were removed.

The results of simulations 1-4 are discussed in section 2.3.1, the results of simulations 5 and 6 in section 2.3.1, simulation 7 is discussed in 2.3.3, and simulation 8 in 2.3.4.

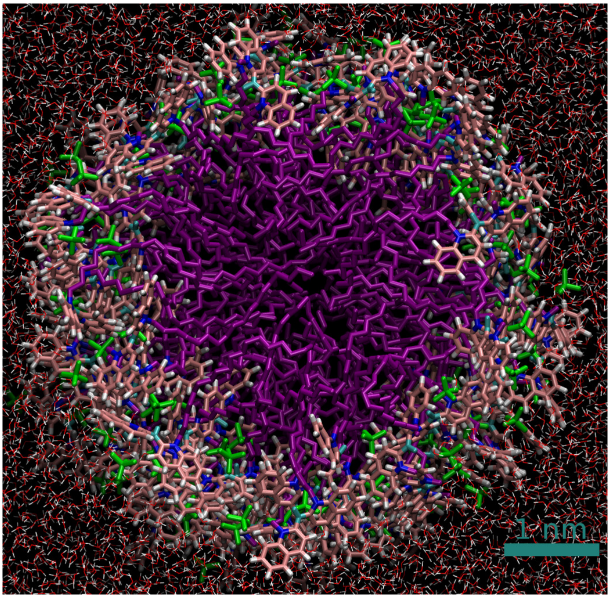

Figure 2.3: View along the cylinder axis of a cylindrical aggregate. Snapshot of simulation 1 taken at 660 ns. *Amphi*-PIC and perchlorate molecules are drawn with thick lines, while water is drawn with thin lines. The coloring scheme is as follows. For the *amphi*-PIC molecule, the CH_3 and $C_{18}H_{37}$ tails are purple; the nitrogen atoms are dark blue; the aromatic carbons are pink; the linker between the aromatic rings is light blue; and hydrogens connected to aromatic carbons are white. Perchlorate molecules are shown in green. For the water molecules, oxygen atoms are red and hydrogen atoms are white. All figures displaying aggregates were made with the VMD program [92].

2.3 Results and discussion

2.3.1 Aggregate geometries obtained from MD simulations

Simulations at room temperature

Depending on the initial concentration of *amphi*-PIC molecules in our MD simulations of spontaneous aggregation, aggregates with different geometries were formed. A micelle formed when a simulation box with 7 nm sides contained 40-60 *amphi*-PIC molecules (corresponding to one *amphi*-PIC molecule per 162-254 water molecules, results not shown), a cylinder when the simulation box contained 70-100 molecules (one *amphi*-PIC molecule per 84-132 water molecules, see Figures 2.3 and 2.4), and a layer when the simulation

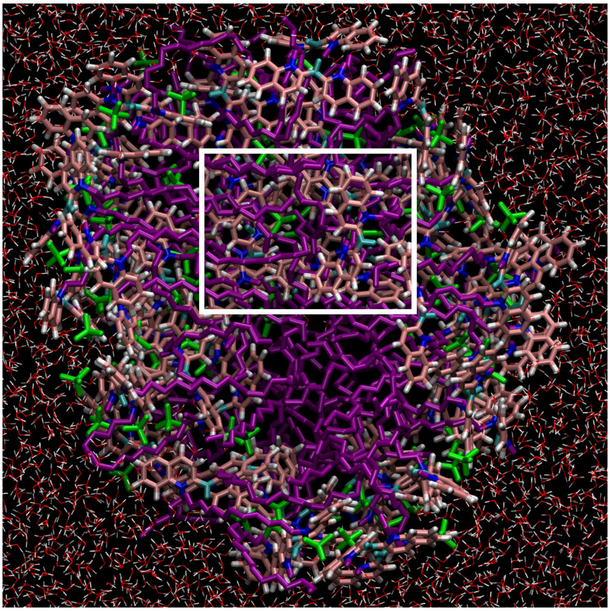

Figure 2.4: View along the cylinder axis of a cylindrical aggregate with salt formation in its interior (enclosed by the white box). Snapshot of simulation 2 taken at 194 ns. Color scheme as in Figure 2.3.

box contained 120-180 molecules (one *amphi*-PIC molecule per 34-66 water molecules, see Figure 2.5). The *amphi*-PIC concentrations used in our simulations correspond to 0.19-0.87 M (to save computer power, we used a much higher *amphi*-PIC concentration than the 10^{-5}-10^{-2} M used in spectroscopic and cryo-TEM measurements [55, 79]). Of the geometries listed above, the preferred geometry seems to be the cylindrical one, except maybe at very high *amphi*-PIC concentrations. Micelles form when there are not enough dye molecules in the simulation box for the aggregate to make a connection to its periodic image. This was also the case in simulation 4 (see Figure 2.6), which started with a larger simulation box, with 11 nm sides and 90 *amphi*-PIC molecules (one *amphi*-PIC molecule per 458 water molecules). Comparable simulations, with a smaller simulation box but the same number of *amphi*-PIC molecules, gave rise to a cylinder. An indication that micelles are not the equilibrium configuration is given by the cylindrical aggregates, which do not show pronounced variations in the radius along their length that would signal that the cylinder may break apart if given enough time. A layer is formed when there are so many molecules in the simulation box that the time needed to break one of the two connections to its periodic image is much longer than the simulation time.

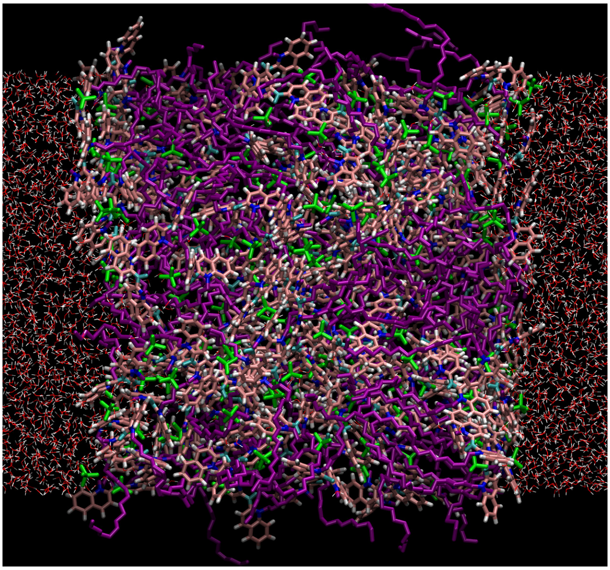

Figure 2.5: A layer-like aggregate, which is connected to its periodic image along the vertical and out-of-plane directions. Snapshot of simulation 3 taken at 534 ns. Color scheme as in Figure 2.3.

The initial aggregation was completed in only a few nanoseconds for boxes with 7 nm sides, and lasted somewhat longer for the box with 11 nm sides. In contrast, the relaxation of the shape and internal ordering of the aggregates took hundreds of nanoseconds (see Appendix 2.7 for details). We conclude that the forces driving the separation of hydrophobic hydrocarbon tails and water are much stronger than those driving the internal ordering of an aggregate. Similar separation of aggregation and reorganization time scales is seen in phospholipid aggregation [67, 68].

In all but one of the tens of cylinders and in all of the layers that we obtained, some head groups and counterions resided in the aggregate's interior, forming a disordered salt-like structure. Simulation 1 was the only instance where no headgroup of an *amphi*-PIC molecule resided in the aggregate interior. We believe these salt-like structures to be defects, caused by the trapping of the *amphi*-PIC and perchlorate ions in the aggregate interior during the fast initial aggregation. The disordered salt did not disappear on the timescale of our simulations (several hundred nanoseconds) and apparently forms a reasonably stable state.

The radius of the cylindrical aggregate of simulation 1 (depicted in Fig-

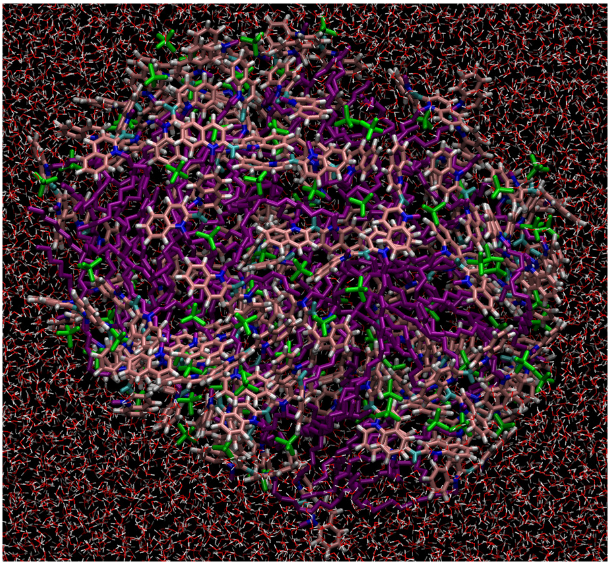

Figure 2.6: A micelle-like aggregate. Snapshot of simulation 4 taken at 185 ns. To enhance the visibility of the aggregate, water in the foreground is not shown. Color scheme as in Figure 2.3.

ure 2.3) is estimated to be 2.2 nm. This value is the radius of gyration of the *amphi*-PIC's nitrogen atoms about the cylinder axis, which went through the center of mass of the nitrogen atoms of all the *amphi*-PIC molecules and was assumed to be parallel to the z-axis. Applying the value of the cylinder radius and the fact that there are 160 *amphi*-PIC molecules in a cylinder section of length 6.8 nm (see Table 2.1), we obtained 0.6 nm^2 for the surface area taken up by a single *amphi*-PIC molecule. This value compares well to 0.55 nm^2 obtained from electron diffraction experiments on two-dimensional *amphi*-PIC crystals [93]. The thickness of the layer of simulation 3 (depicted in Figure 2.5) is estimated as 5.9 nm; the micelle of simulation 4 (depicted in Figure 2.6) has an estimated size of 4.0 nm × 5.0 nm × 6.5 nm.

Simulated annealing and high temperature simulations

In simulation 5, we performed simulated annealing on the only cylinder without defects that was obtained at room temperature in simulation 1, repeatedly increasing the temperature to 400 K and then cooling down again to room temperature. The annealing caused the cylinder to widen into a ribbon-like shape, as shown in Figure 2.7a (with a ribbon, we mean a cylindrical aggregate

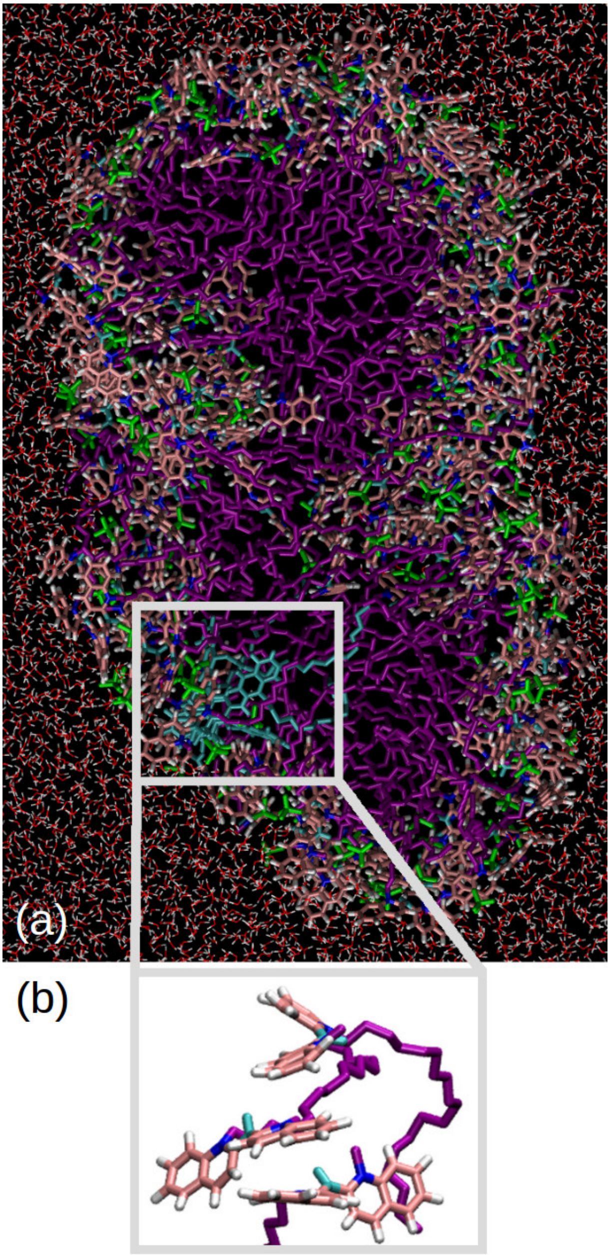

Figure 2.7: Simulated annealing of the cylindrical aggregate from Figure 2.3 results in an aggregate with the shape of a ribbon. Snapshot of simulation 5 taken at 760 ns. (a) Top view. (b) Side view of three π - π stacked *amphi*-PIC molecules shown in light blue in (a). Color scheme as in Figure 2.3.

strongly elongated in one of the directions perpendicular to the long axis). The size of this aggregate is estimated to be 5.7 nm by 9.8 nm, in the directions perpendicular to the long axis. Aggregates with a similar ribbon-like shape have been observed experimentally using cryo-TEM, for J-aggregates of the dyes C8S2 [94], C8S3 [56], and C8O4 [95].

To obtain more aggregates that lack salt formation in their interior, we performed simulations with an initial temperature of 400 K and cooled the system down to room temperature after the spontaneous aggregation had taken place. Many of these simulations indeed gave rise to aggregates without salt-like structures in their interior, in contrast to the runs that started at room temperature. Simulation 6 represents a typical result, in which a ribbon-like aggregate without salt-like arrangement in the interior was formed (the resulting geometry was similar to that of simulation 5, depicted in Figure 2.7a). Note that, except for the temperature, the simulation conditions were the same as in simulation 1, where a cylindrical aggregate formed.

Increasing the temperature to 400 K did not eliminate the salt-like structures in the interior of aggregates that had previously formed at room temperature. The salt-like structures were not noticeably reduced after tens of nanoseconds of simulation time. Apparently, the salt-like structures are quite stable, which also agrees well with our finding that they do not disappear after hundreds of nanoseconds of simulation time at room temperature.

It is not clear whether the equilibrium aggregate structure, with the minimal Gibbs free energy, is the cylindrical aggregate of simulation 1 or the ribbon-like aggregate of simulations 5 and 6. One possibility is that the cylindrical geometry represents only a local minimum of Gibbs free energy, and that the higher temperature allows the system to overcome energy barriers and reach the ribbon-like state, which would then be the global minimum. Alternatively, the ribbon geometry might be an artifact, caused by lowering the temperature too fast. This view is corroborated by the observed strong contraction of aggregates along the connection to their periodic image when the temperature is raised. It would mean that the relaxation time of the global aggregate structure is longer than 50 ns, which is the time span used to cool down the ribbon-like aggregate in simulation 6. A third possibility is that the ribbon-like aggregates are an intermediate state between the cylinder and two coupled cylinders (which are discussed in section 2.3.4).

Cylindrical and ribbon-like aggregates were always observed to be parallel to the z-axis, not tilted. The box dimension in the z-direction (see Table 2.1) thus equals the length of one periodic cylinder unit. To understand the meaning of the box dimensions, note that the system formed by a simulation box with periodic boundary conditions can alternatively be viewed as a system consisting of an infinitely large number of copies of the simulation box, thus having an infinite extent in all directions. Therefore, a simulation box containing a cylindrical aggregate corresponds to a system containing an infinite number of infinitely long cylinders, with repetition periods given by the box dimensions.

2.3.2 Quantifying the internal order in the cylindrical aggregates

As is apparent from all figures presented above, there is a large degree of structural disorder in the aggregates. While it is not clear yet whether this disorder would survive even much longer simulation times, this result is consistent with the large width ($650\,\mathrm{cm}^{-1}$) of the measured absorption band of *amphi*-PIC aggregates [79]. This is in fact one of the largest widths experimentally observed for any aggregate of dye molecules. The large width of the absorption spectrum may be caused by disorder in the excitonic couplings and the transition energies, which are, in turn, caused by the disordered stacking of the molecules in the aggregate. In this section, we quantify the amount of (dis)order in the internal structure of the aggregates.

Quantifying the π - π-stacking

π - π stacking is of fundamental importance for the structure of aggregates of dye molecules, and thus for their optical and electronic energy transport properties. It leads to strong excitonic coupling, resulting in large exciton delocalization and efficient energy transport. An example of the π - π stacking observed in *amphi*-PIC aggregates is shown in Figure 2.7b, which depicts three molecules in the ribbon-like aggregate of simulation 5. We use three quantities to describe the π - π stacking in *amphi*-PIC aggregates. Firstly, for an arbitrary quinoline ring, the pair separation distribution function gives the average number of quinoline neighbors per unit separation distance, and is used as a measure for the quantity of stacking. Secondly, two order parameters, namely a measure for the alignment of the quinoline rings and for the relative shift of nearby quinoline rings, describe the quality of π - π stacking.

The pair separation distribution function is defined as the number of quinoline ring pairs per unit of separation distance, normalized by dividing by the number of quinoline rings. Quinoline pairs belonging to the same *amphi*-PIC molecule are not taken into account. To determine the separation between quinoline rings, we defined their position $\mathbf{r}$ to be the middle of the central

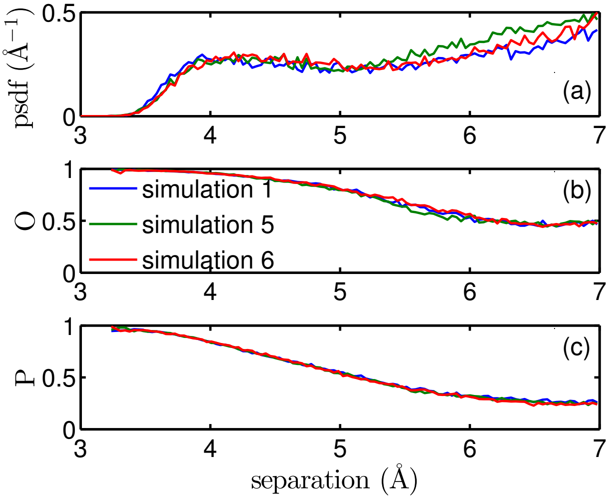

Figure 2.8: (a) The pair separation distribution function (psdf), which is used as a measure for the quantity of π - π stacking. (b,c) The two order parameters O and P, defined in Eqs. 2.2 and 2.3, which are a measure for the quality of π - π stacking. For each simulation, average values are given for 101 snapshots of the aggregate geometry, obtained from the final 20 ns of the respective trajectories.

C-C bond, $\mathbf{r} = (\mathbf{r}_5 + \mathbf{r}_6)/2$ or $\mathbf{r} = (\mathbf{r}_{16} + \mathbf{r}_{17})/2$, depending on which of the two quinoline rings of the *amphi*-PIC molecule is considered. Here $\mathbf{r}_n$ is the position of the n-th atom (see Figure 2.1). The pair separation distribution functions for three aggregates are given in Figure 2.8a. We observe that the minimal distance between two quinoline rings is approximately 3.4 Å. This compares well to the crystal structure of the PIC molecule obtained from X-ray diffraction measurements [96], where the interplanar distance between quinoline rings, which is a lower bound for their separation due to a shift between the quinoline ring planes, is either 3.29 Å or 3.57 Å (there are two types of quinoline ring stacking in the crystal). The expected first peak in the pair separation distribution function, corresponding to nearest neighbors, is seen around 4 Å.

The first order parameter is a measure for the alignment of the quinoline rings and is defined as

$$O = \langle |\hat{\mathbf{a}}_i \cdot \hat{\mathbf{a}}_j| \rangle, \tag{2.2}$$

where the average is taken over all pairs of quinoline rings i and j at a specific separation. The unit vector perpendicular to the quinoline ring plane is defined as $\hat{\mathbf{a}} = (\mathbf{r}_6 - \mathbf{r}_3) \times (\mathbf{r}_6 - \mathbf{r}_9)/|(\mathbf{r}_6 - \mathbf{r}_3) \times (\mathbf{r}_6 - \mathbf{r}_9)|$ or $\hat{\mathbf{a}} = (\mathbf{r}_{17} - \mathbf{r}_{20}) \times (\mathbf{r}_{17} - \mathbf{r}_{14})/|(\mathbf{r}_{17} - \mathbf{r}_{20}) \times (\mathbf{r}_{17} - \mathbf{r}_{14})|$. O equals 0 when all planes under consideration are perpendicular (no alignment), and 1 when all planes are parallel (perfect alignment). When the planes of two quinoline rings are nearly parallel, a second order parameter is a measure of their relative shift. It is defined as

$$P = \langle |\hat{\mathbf{a}}_i \cdot \hat{\mathbf{r}}_{ij}||\hat{\mathbf{a}}_j \cdot \hat{\mathbf{r}}_{ij}| \rangle, \tag{2.3}$$

where again the average is taken over all pairs at a specific separation, and the normalized displacement vector $\hat{\mathbf{r}}_{ij} = (\mathbf{r}_i - \mathbf{r}_j)/|\mathbf{r}_i - \mathbf{r}_j|$ connects two quinoline rings. The order parameter P assumes the value of 1 when all quinoline ring planes are parallel and have no relative shift, and 0 when all quinoline rings lie next to each other in the same plane instead of face to face.

Figure 2.8 shows that the π-π stacking does not depend on the aggregate shape. Even though the aggregate of simulation 1 had a different overall shape than the aggregates of simulations 5 and 6, both the number of stacked molecules (quantified by the pair separation distribution function) and the quality of the π-π stacking (given by the order parameters) are the same for all three aggregates under consideration. This suggests that the internal structure of cylindrical and ribbon-like aggregates is the same. In a future publication, we will investigate this statement further by comparing the absorption and linear dichroism spectra of cylindrical and ribbon-like aggregates.

In addition, Figure 2.8 shows that both order parameters are close to unity for the closest quinoline ring pairs. Their planes are thus almost parallel and facing each other, indicating that these pairs are perfectly π-π stacked. This is exactly what one would expect, because for the closest quinolines there is no room to tilt one of the quinoline planes, and quinolines with a relative shift as a consequence have a larger than minimal separation; thus the closest quinolines must be π-π stacked. The larger the separation between two quinoline rings, the worse the π-π stacking becomes.

Distribution of dipole orientations

The orientation of the transition dipoles between the electronic ground state and the first excited state of the *amphi*-PIC molecules is important for the intermolecular couplings and the polarization of the optical excitations of the aggregate. To analyze the transition dipoles, we assign a 'molecular vector' to each *amphi*-PIC molecule. This molecular vector has unit length and points along the long axis of the *amphi*-PIC headgroup, from one nitrogen atom to the other (see Figure 2.1),

$$\hat{\mathbf{v}} = (\mathbf{r}_7 - \mathbf{r}_{12})/|\mathbf{r}_7 - \mathbf{r}_{12}|. \tag{2.4}$$

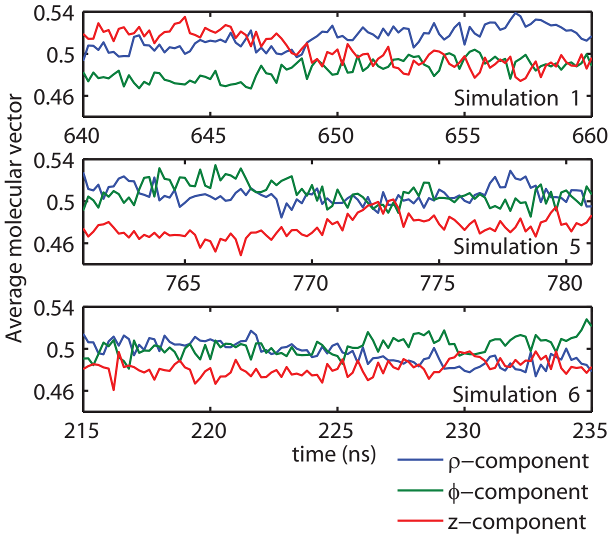

Figure 2.9: Average molecular vector (defined in Eq. 2.4) as a function of time, in cylindrical coordinates. For each graph, 101 snapshots of the aggregate geometry have been taken from the final 20 ns of the respective trajectories.

The molecular vector approximates the transition dipole to the first excited state to a good degree: for the optimized gas-phase molecular geometry, the angle between the molecular vector and the transition dipole is only 9°. To determine this angle we performed time-dependent density functional theory calculations, using the B3LYP functional and 6-31G* basis set, with the QChem program version 3.2.

The average molecular vector is plotted as a function of time in Figure 2.9. Because we consider aggregates with the shape of a cylinder or ribbon, it is natural to express the molecular vector in cylindrical coordinates (ρ, ϕ, z). The local cylindrical reference frame is obtained by shifting the origin in the x- and y-direction (i.e. in the direction perpendicular to the cylinder), so that the new z-axis goes through the center of mass of the *amphi*-PIC molecule's nitrogen atoms. We can conclude that the molecular vector, and thus the transition dipole, does not have a preferential direction. The observed differences in the average vector components may be explained as being statistical fluctuations.

Our result, indicating the isotropic orientation of the transition dipoles, may explain the fact that the polarization dependent absorption spectra measured for *amphi*-PIC aggregates in a stretched PVA film [79] show only weak polarization of the spectral features.

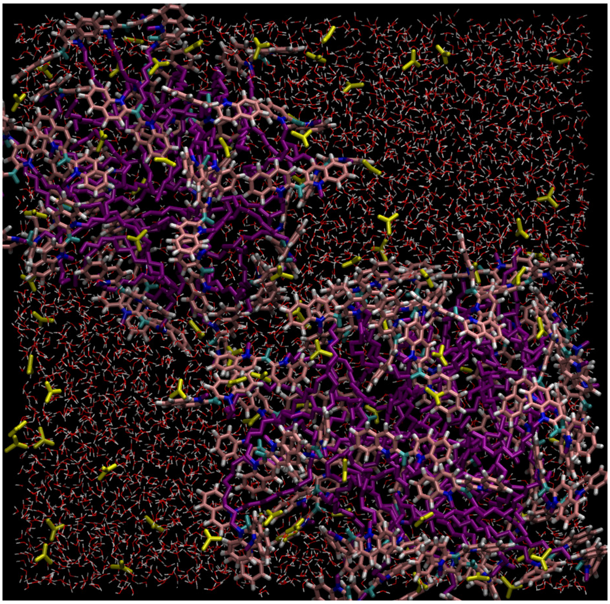

Figure 2.10: Two micelles form when acetate instead of perchlorate is used as a counterion. Snapshot of simulation 7 taken at 298 ns. Color scheme as in Figure 2.3, with the addition that acetate molecules are shown in yellow. To enhance the visibility of the aggregates, water in the foreground is not shown.

2.3.3 Effect of the choice of counterion

One of the difficulties encountered in our simulations is that strong interaction between the *amphi*-PIC headgroups and perchlorate counterions leads to salt-like structures and thus to slow dynamics. Therefore, we investigated the effect of a weaker interaction between headgroups and counterions by using a different counterion. It is known that the binding strength of ions to lipid membranes follows a Hofmeister series [97], also when the lipid headgroups carry a positive charge, like *amphi*-PIC headgroups. We thus expect that a Hofmeister series also holds for the binding of counterions to *amphi*-PIC aggregates. Since perchlorate and acetate are on the opposite side of the Hofmeister series, we performed several simulations with an acetate counterion (CH_3COO^-) instead of a perchlorate counterion. A typical result is simulation 7, with its final geometry shown in Figure 2.10. Indeed, we observe that the binding of acetate counterions to the headgroups is weaker than for perchlorate counterions, since many acetate ions are now located in the solvent. Except for the counterion, the initial conditions in simulation 7 are the same as those in simulations 1 and 2. However, instead of a cylindrical aggregate as in simulations 1 and 2, two micelles are formed. When using an acetate counterion, our simulations thus predict that the most stable geometry is the micelle. Since in our simulation the *amphi*-PIC concentration has the very high value of 0.4 M, this prediction also holds for high concentrations.

The micelle formation can be understood from Israelachvili's theory on the influence of molecular shape on aggregates [98]. This theory states that for an aggregate consisting of amphiphilic molecules, the equilibrium aggregate geometry is determined by the relative sizes of the molecules' headgroups and tails. The reason is that the surface to volume ratio differs for the different shapes an aggregate can have. If the headgroups are relatively large, micelles are formed; when they are smaller, cylinders. It can be seen that the space taken up by the headgroup of an *amphi*-PIC molecule must be bigger with an acetate counterion than with a perchlorate counterion. When using a perchlorate counterion, all the counterions were located on the aggregate, near the headgroups. Acetate counterions, on the other hand, partly resided in the bulk solvent instead of being in the direct vicinity of the aggregate (contrast Figure 2.10 with the others), and thus not fully compensated the charge of the *amphi*-PIC's headgroups. The resulting electrostatic repulsion between the headgroups effectively increases their volume, promoting the formation of micelles.

2.3.4 Bundling of cylindrical aggregates

Bundled cylindrical aggregates of the C8S3 dye have been observed with scanning force microscopy [73] and in cryo-TEM experiments [56], where, depending on the experimental conditions, the cylinders are bundled either in parallel or as intertwined helices. Furthermore, cryo-TEM images of cylindrical C8O3 aggregates show bundles of intertwined helices [95]. Motivated by these experiments, we studied bundling of *amphi*-PIC aggregates by placing multiple cylindrical aggregates in the same simulation box. Simulation 8 represents a typical result.

This simulation predicts that cylindrical *amphi*-PIC aggregates form bundles (see Figure 2.11). Initially, the simulation box contained two cylindrical aggregates separated by water (with a center-to-center distance of 13.6 nm), undergoing Brownian motion. When the Brownian motion caused the aggregates to come near each other after 25 ns, they formed a bundle. Apparently, there is a short-range attractive force between the aggregates. The cylinders stayed attached for the remaining 225 ns of the simulation duration. Initially, many water molecules resided between the walls of the bundled cylinders.

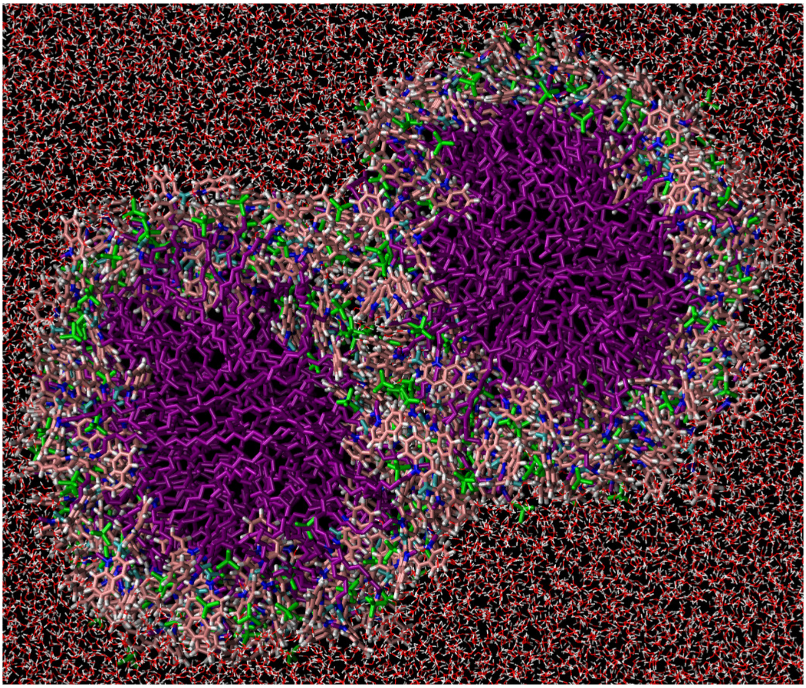

Figure 2.11: Two bundled cylindrical aggregates viewed along the cylinder axis. Snapshot of simulation 8 taken at 248 ns. Color scheme as in Figure 2.3.

Their number decreased during the simulation, but at the end several tens of water molecules remained between the cylinders. In order to understand the bundling of *amphi*-PIC cylinders, it is important to note that the perchlorate counterions are located in the aggregates instead of being dissolved in the bulk water, making the aggregates neutral and reducing the Coulomb repulsion between them. In fact, the interface between the cylindrical aggregates forms a salt-like structure, similar to the structures observed in simulations 2 and 3. Because of the short length of the cylindrical aggregates in simulation 8, we can not make a prediction about possible intertwining of bundles of *amphi*-PIC aggregates into helical superstructures.

2.4 Conclusions

We have used molecular dynamics simulations of spontaneous aggregation to determine the shape and internal structure of aggregates of the dye molecule *amphi*-PIC with perchlorate as counterion. In the MD simulations, which required extending known force field parametrizations to include rotations around the central bond of the *amphi*-PIC molecule, the initial aggregation takes place within several nanoseconds; however, the equilibration of the internal aggregate structure takes hundreds of nanoseconds. Two aggregate shapes, that of the cylinder and ribbon, are candidates for the equilibrium morphology; due to the slow dynamics we cannot determine which one of them is the real structure. Thus the MD simulations predict that either cylindrical or ribbon-like aggregates of the *amphi*-PIC dye exist in nature. The arrangement of the *amphi*-PIC molecules in the aggregate is very disordered and no difference in internal order is observed between the cylindrical and the ribbon structure.

We have investigated the internal order of the cylindrical and ribbon-like aggregates by quantifying the π - π stacking and the average orientation of the *amphi*-PIC molecule's transition dipole. Using two order parameters to describe the π - π stacking, we showed that the *amphi*-PIC molecules which are closest to each other are π - π stacked to a high degree; long-range order is lacking, however, at least it is not reached during the time scale of our simulations. We have also shown that the orientation of the transition dipoles is isotropic.

In simulations with acetate instead of perchlorate counterions, the equilibrium aggregate morphology turns out to be the micelle. The reason is that many counterions reside in the bulk solvent instead of in the aggregate, giving the aggregate a net charge and increasing the effective size of the *amphi*-PIC headgroups. It is well known that this promotes the formation of micelles rather than cylinders [98]. We hope that our prediction about the formation of micelles, as well as the predicted formation of cylindrical or ribbon-like aggregates when using the perchlorate counterion, may be tested in the future by microscopy experiments. Finally, we have demonstrated that cylindrical *amphi*-PIC aggregates form bundles, and our simulations show how the interface of such bundles may be organized.

Molecular dynamics simulations of spontaneous aggregation are a promising method for determining the structure of aggregates of dye molecules, and may be applied to aggregates of many types of dye molecules in the future. With the increasing availability of computational power, the system size that MD simulations can handle will grow as well. When combined with quantum chemical methods that relate the electronically excited states of the aggregate to its structure [99, 100], this will enable a first-principles modeling of the optical spectroscopy of molecular aggregates. A first application in this direction will be the calculation of the absorption and linear dichroism spectra for the

atom	charge (e)	atom	charge (e)	atom	charge (e)
C1	−0.46	C8	−0.14	H2	0.17
C2	0.23	C9	−0.14	H3	0.17
N3	0.08	C10	−0.14	H4	0.14
C4	0.09	C11	−0.14	H5	0.14
C5	0.14	C12	0.15	H6	0.14
C6	−0.17	H1	0.18	H7	0.14
C7	−0.22				

Table 2.2: Atomic charges of the *amphi*-PIC molecule. The atom labels are specified in Figure 2.12.

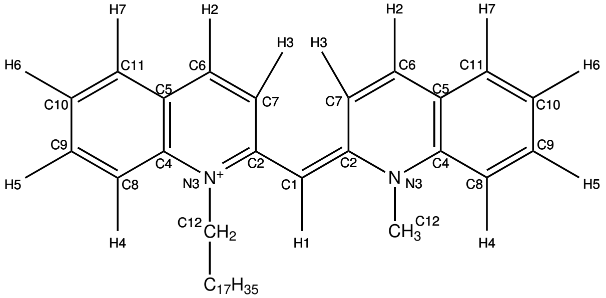

Figure 2.12: Atom labeling for the *amphi*-PIC molecule. Pairs of equivalent atoms have the same label. Note that the C12 label refers to the whole CH_2 or CH_3 group.

structures described here, which will be reported in a forthcoming publication. In the future, we hope that microscopic modeling will provide a deeper understanding of the wealth of optical and energy transport experiments that have been performed on aggregates of dye molecules (cf. Introduction).

2.5 Appendix: atomic charges of the *amphi*-PIC molecule

The atomic charges of the *amphi*-PIC molecule (see Table 2.2) were based on the results of the CHELPG method [81], which fits the charges to the molecular electrostatic potential. The regular grid used for the fitting had a spacing of 0.3 Å, with the extent of the grid determined by the conditions that the grid points lie within a distance of 6 Å from any atom and outside the COSMO van der Waals radii of the nuclei; this gave a total of 134635 grid points. A simplified model of the *amphi*-PIC molecule was used, with the $C_{18}H_{37}$ side chain replaced by a C_2H_5 group. Calculations were performed using density functional theory with B3LYP functional and 6-31G* basis set, for the equilibrium vacuum-phase geometry obtained at the same level of theory. The resulting charges were symmetrized to reflect the equivalence of the two quinoline units in the *amphi*-PIC molecule. All calculations were performed with the Orca program version 2.7.

2.6 Appendix: additional details about the force field parametrization

For the calculation of the potential energy as a function of only one of the dihedral angles, quantum mechanical and force field geometry optimization calculations were performed varying the constrained dihedral angle by intervals of 5°. Because the force field calculation sometimes did not find the global minimum, two series of calculations were performed. Both series start with the first dihedral angle constrained to 0°. In the first series, the value of the constrained dihedral angle was increased in steps of 5° until a value of 360° was reached, while in the second series it was decreased in steps of 5° until $-360°$ was reached. For the first calculation in the series, the initial geometry was taken from quantum-chemistry calculations; for all subsequent calculations, the starting geometry was the output of the previous optimization. Finally, the force field energy curve was obtained by taking the lowest energy result of both series at each value of the restrained angle.

For the calculation of the two-dimensional potential energy surface, points were sampled every 10°, except for points on the diagonal, which were sampled every 5°. In addition, the global minimum and the lowest local minimum were determined by a full (unconstrained) optimization. To avoid ending in a local minimum in the force field calculations, we used a scheme similar to the one outlined above for the calculation of the one-dimensional energy function. Moreover, the symmetry of the simplified *amphi*-PIC molecule, with its $C_{18}H_{37}$ tail replaced by a methyl group, was used to reduce the number of distinct points on the potential energy surface by a factor of four. Namely, the molecule is invariant under the transformation $(\phi_1, \phi_2) \to (\phi_2, \phi_1)$ and is transformed into its mirror image (with the same energy) by the transformation $(\phi_1, \phi_2) \to (-\phi_1, -\phi_2)$ (see the main text for the definition of the dihedral angles ϕ_1 and ϕ_2).

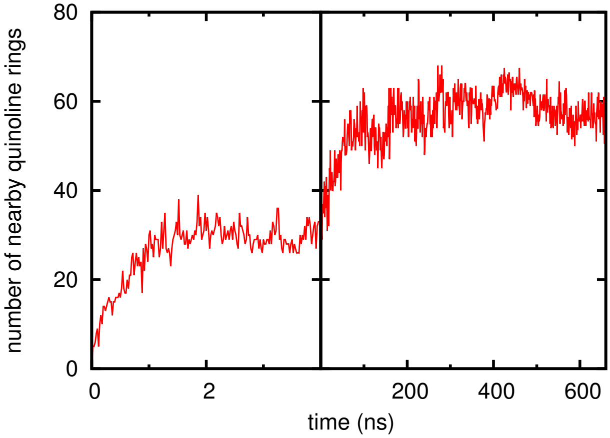

Figure 2.13: The number of quinoline ring pairs in the cylindrical aggregate (simulation 1 of the main text) that are separated by less than 0.5 nm, as a function of time. The left part of the graph visualizes the spontaneous aggregation of the dye molecules within the first few nanoseconds of the simulation, while the right part shows that it then takes hundreds of nanoseconds for the internal structure of the aggregate to equilibrate. Notice the change in the time axis after 4 ns.

2.7 Appendix: time scales of the spontaneous aggregation process

In order to get deeper insight into the dynamics and stability of the aggregation process, we consider various structural characteristics. We distinguish between the equilibration of the internal aggregate structure, which we quantify using the number of nearby quinoline pairs, and the equilibration of the global aggregate shape, which we describe by the aggregate's radius and the length of a periodic unit. For both analyses we used the cylindrical aggregate of simulation 1.

The time evolution of the number of closely spaced quinoline ring pairs, shown in Figure 2.13, is a measure for the amount of π-π stacking in the cylinder, which forms the only discernible internal structure. We can clearly distinguish two time scales. In the intial phase of the aggregation process, the *amphi*-PIC molecules combine within several nanoseconds. Then, over the following hundreds of nanoseconds, more and more dye molecules π-π stack until the internal structure has equilibrated.

The time dependence of the aggregate shape is shown in Figure 2.14. After

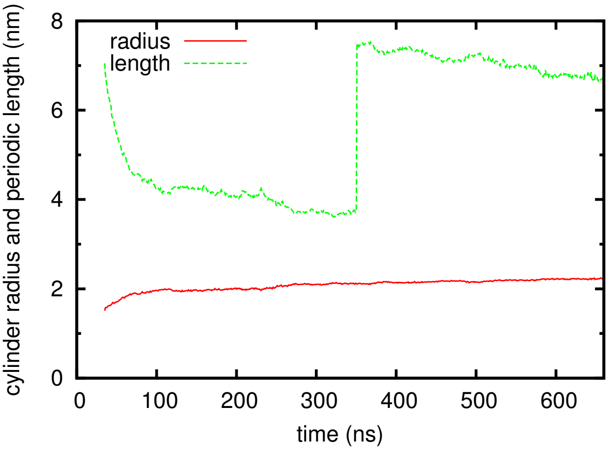

Figure 2.14: The time evolution of the shape of the cylindrical aggregate (simulation 1 of the main text), which is described by the radius of the cylinder and the length of a periodic unit in the direction of the cylinder axis. To prevent molecules from interacting with their periodic image, the simulation box is duplicated in the direction of the cylinder axis after 350 ns. This causes the length of a periodic cylinder image to double as well.

semi-isotropic pressure coupling was instated at 35 ns so that the box dimension along the cylinder axis was free to equilibrate separately from the other two box dimensions, the cylinder simultaneously became wider and contracted in the direction of its axis. At the end of the simulation at 660 ns, a slight drift in both the cylinder length and radius can still be observed. Apparently the shape of the cylindrical aggregate equilibrates slower than its internal structure.

Next to giving information on the equilibration of the molecular aggregate, Figures 2.13 and 2.14 also give information on aggregate stability. Figure 2.13 shows that over long time scales the aggregate structure is quite stable, while on shorter time scales a part of the quinoline ring pairs are periodically crossing the cutoff separation of 0.5 nm and then back again. From Figure 2.14 we see that the aggregate radius is extremely stable, while the length of a cylinder period fluctuates slightly due to the pressure coupling.

2.8 Appendix: an overview of all performed molecular dynamics simulations

In this chapter, the results of eight representative molecular dynamics simulations have been presented in detail. These eight simulations represent only a subset of the 82 simulations of spontaneous aggregation that were performed in total. An overview of all performed MD simulations of spontaneous aggregation, including the shape of the formed aggregate for each simulation, is given in Table 2.3 (note that the bundling simulations have been omitted). In the simulations performed at room temperature we observed varying degrees of salt formation in the aggregate's interior: the salt-like structures were formed in all layer-like aggregates, in all cylindrical aggregates except the cylinder that resulted from simulation 1 (as discussed in the main text), and in the micelles of bigger radius.

counterion	Temp. (K)	number of *amphi*-PICs	number of simulations	resulting aggregate shape
perchlorate	298	40	1	micelle
perchlorate	298	60	1	micelle
perchlorate	298	70	4	cylinder
perchlorate	298	70	1	two contacts
perchlorate	298	80	22	cylinder
perchlorate	298	80	19	two contacts
perchlorate	298	90	2	cylinder
perchlorate	298	90	1	micelle [a]
perchlorate	298	100	3	cylinder
perchlorate	298	100	2	two contacts
perchlorate	298	110	1	two contacts
perchlorate	298	120	2	layer
perchlorate	298	140	2	layer
perchlorate	298	160	2	layer
perchlorate	298	170	1	layer
perchlorate	298	180	1	layer
perchlorate	298	180	1	three contacts
perchlorate	298	180	1	two contacts [b]
perchlorate	400	80	2	micelle
perchlorate	400	80	7	cylinder
perchlorate	400	100	1	cylinder
perchlorate	500	100	1	cylinder
acetate	298	70	1	two micelles
acetate	298	80	1	two micelles
acetate	298	100	1	two micelles
acetate	298	160	1	one micelle

Table 2.3: An overview of the performed molecular dynamics simulations, listing the type of counterion used, the temperature, the number of *amphi*-PIC molecules in the simulation box, the number of independent simulations with the same starting conditions and resulting aggregate shape, and the shape of the aggregate which was spontaneously assembled. In some simulations, more contacts with the aggregate's periodic image remained than is to be expected on the basis of the *amphi*-PIC concentration. These cases are most likely artefacts caused by the limited time span of roughly 100 ns for which the simulations were run.

[a] Simulation box with 11 nm sides (when not otherwise noted, simulations were started in boxes with 7 nm sides). [b] Simulation box with 10 nm sides.

Chapter 3

First-principles calculation of the optical properties of an amphiphilic cyanine dye aggregate[1]

Using a first-principles approach we calculate electronic and optical properties of molecular aggregates of the dye *amphi*-pseudoisocyanine, whose structures we obtained from molecular dynamics (MD) simulations of the self-aggregation process. Using quantum chemistry methods, we translate the structural information into an effective time-dependent Frenkel exciton Hamiltonian for the dominant optical transitions in the aggregate. This Hamiltonian is used to calculate the absorption spectrum. Detailed analysis of the dynamic fluctuations in the molecular transition energies and intermolecular excitation transfer interactions in this Hamiltonian allows us to elucidate the origin of the relevant timescales: short timescales, of the order up to a few hundreds of femtoseconds, result from internal motions of the dye molecules, while the longer (a few picosecond) timescales we ascribe to environmental motions. The absorption spectra of the aggregate structures obtained from MD feature a blueshifted peak compared to that of the monomer, thus our aggragates can be classified as H-aggregates, although considerable oscillator strength is carried by states along the entire exciton band. Comparison to the experimental absorption spectrum of *amphi*-PIC aggregates shows that the simulated lineshape is too

---

[1] This chapter is based on F. Haverkort, A. Stradomska, A. H. de Vries, and J. Knoester, *J. Phys. Chem. A* **118**, 1012 (2014)

wide, pointing to too much disorder in the internal structure of the simulated aggregates.

3.1 Introduction

Self-assembled aggregates of synthetic dye molecules are widely seen as promising functional materials for nanotechnology. Inspired by the natural dye aggregates [13–15] that are responsible for the absorption of sunlight and the subsequent transport of the resulting electronic excitation energy to photosynthetic reaction centers in plants and bacteria, artificial aggregates might be used for light harvesting as well. More generally, molecular aggregates are of fundamental interest for the study of collective optical phenomena, since their optical properties are profoundly different from those of their monomeric building blocks. These special collective properties include very narrow optical lineshapes [31], ultrafast spontaneous emission [32–34], strong nonlinear optical response [7–10, 35], and fast electronic energy transfer [36–38].

In the past, great successes in modeling the optical properties of molecular aggregates have been obtained using a phenomenological approach [59, 64, 78]. In this approach, a model structure of the studied aggregate is proposed that yields good reproduction of experimental spectra. The molecules are characterized solely by their transition energies and dipole moments, while for the intermolecular interactions a model structure is assumed; no atomic-scale details on molecular packing are provided. Model parameters, structural as well as energetic, are obtained by fitting thus calculated spectra to experiment. However, this phenomenological approach has several drawbacks. First of all, a number of different structures may lead to a good reproduction of the experimental data. This is the case for J-aggregates of the dye pseudoisocyanine, for which the uncertainty about the aggregate structure remains, even after decades of research. [1]. Another drawback is that phenomenological modeling provides limited microscopic knowledge of the excitonic states which underlie the aggregates' optical properties. At the same time, novel spectroscopic techniques [48, 52, 55, 101] give new insights into the photophysics of the molecular aggregates which calls for increased detail in theoretical modeling as well. Complementary to the phenomenological modeling of molecular aggregates, growing computer power and more efficient computational methods are nowadays making first principles approaches a promising tool to study molecular aggregates' special optical and energy transport properties [24, 102–107]. Ideally, this first principles approach delivers detailed information on the aggregates' molecular structure and excitonic states with the input of only little experimental information.

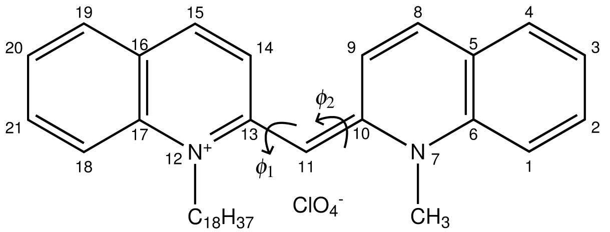

Figure 3.1: The *amphi*-PIC cation with its perchlorate counterion. The dihedral angles ϕ_1 and ϕ_2 are defined in Section 3.2.1.

In chapter 2, we have obtained for the first time the molecular structure of a dye aggregate from molecular dynamics (MD) simulations. In particular, we studied the spontaneous aggregation process of *amphi*-pseudoisocyanine (*amphi*-PIC, see Figure 3.1). The research presented in the current chapter is a next step on the route to modeling the optical response of molecular aggregates fully from first principles. First, we fine-tuned our force field until the experimental absorption spectrum of the *amphi*-PIC monomer was reproduced to reasonable accuracy. Next, the cylindrical and ribbon-like structures obtained previously were re-equilibrated using the updated force field and then used as a starting point for quantum-chemical calculations which provided us with the aggregates' Hamiltonian and the molecular transition dipole moments within the aggregates. These in turn yielded the aggregates' exciton states and optical properties. We found that the highly disordered nature of the studied aggregates results in very similar spectra of the cylindrical and ribbon-shaped aggregates, which can be explained by the isotropic orientation distribution of the individual molecules within the aggregate. We were able to identify timescales responsible for the memory effects in the Hamiltonian and ascribe the fast ones (11 fs, 120 fs and 260 fs) to internal motions of the molecules and the slower ones (6.9 ps and 11 ps) to fluctuations in the intermolecular positions (both within the aggregate and between aggregate and solvent).

The outline of this chapter is as follows. In Section II, we describe the force field, the MD simulations of an *amphi*-PIC monomer and aggregates in solution, and explain how the exciton Hamiltonian is obtained. In Section III, we first discuss our results on the *amphi*-PIC monomer, which is used as a test of our methodology. Then, we analyze our results for the Hamiltonian and excitonic states of the cylindrical aggregate. Next, the absorption and linear dichroism spectra of the cylindrical and ribbon-like aggregates are calculated and discussed. In the final Section IV, we summarize and conclude.

3.2 Computational details

3.2.1 Force field

As our starting point we have taken the force field used in chapter 2, which was based on GROMOS53A6 [80] but included two modifications for the *amphi*-PIC molecule. First, the atomic charges for the *amphi*-PIC molecule were calculated using the quantum-chemical CHELPG method [81]. Second, to properly describe the twisting of the *amphi*-PIC molecule around its central bond, potential energy terms were added for the two dihedral angles ϕ_1 and ϕ_2, defined by atoms 10-11-13-14 and 13-11-10-9, respectively (see Figure 3.1).

However, in the course of the current study we found out that the structures obtained with this force field resulted in the width of the *amphi*-PIC's monomer absorption spectrum being overestimated by approximately a factor of two, as compared to the experimental value. The main reason turned out to be too much flexibility of the bridge between the quinoline rings comprising the *amphi*-PIC chromophore. Therefore, we adjusted the force constant of the improper dihedral which keeps the *amphi*-PIC's linker carbon atom (atom 11 in Figure 3.1) in plane with both of the quinoline rings it is attached to. The new value for the force constant was determined from the accurate potential energy surface (PES) for this dihedral, obtained on the level of density functional theory. A series of constrained quantum-chemical geometry optimization calculations was performed with the Orca program version 2.9 [108], using the B3LYP functional [84, 85] and Pople's 6-31G* basis set. Throughout the calculations, a simplified version of the *amphi*-PIC molecule was used, with its $C_{18}H_{37}$ tail replaced by a C_2H_5 group. In each calculation, the dihedral angle 13-12-14-11 was fixed at a different value while the rest of the molecule was relaxed. The resulting one-dimensional PES was fitted with a quadratic potential function to yield the force constant. As a result of these calculations, the force constant for the dihedrals 10-7-9-11 and 13-12-14-11 was increased by a factor 4.5 to $753.4\,\mathrm{kJ\,mol^{-1}\,rad^{-2}}$. The effect of this stiffer bridge was a narrowing of the monomer absorption spectrum by roughly a factor two. Thus it turns out that using accurate force constants for the dihedrals that determine the bridge stiffness is crucial for reproducing spectral properties, and that the generic force constant for improper dihedrals that is used in the GROMOS53A6 force field to keep $\pi - \pi$ systems in plane is not sufficient.

Also the angles within aromatic rings turned out to have too much flexibility. This inaccuracy is probably due to insensitivity to these angles' force constant of the (infrared) spectroscopic properties of small molecules to which the GROMOS force fields were parametrized. Thus, a similar procedure as

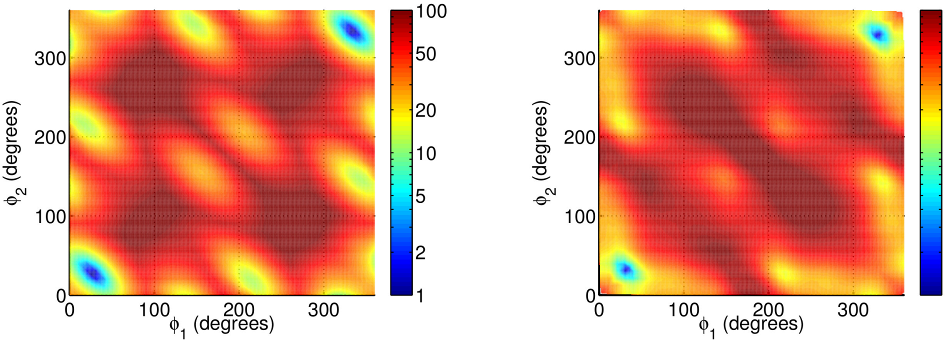

(a) quantum chemistry

(b) modified force field

Figure 3.2: The potential energy surface as a function of two dihedral angles ϕ_1 and ϕ_2 of the *amphi*-PIC molecule, obtained using (a) the quantum-chemical DFT method, and (b) the modification of the GROMOS53A6 force field used in this chapter. Energy scale in kJ mol^{-1}, with the lowest energy value of each plot set to 1 kJ mol^{-1}.

that for the stiffening of the *amphi*-PIC's bridge was applied to all angles in the aromatic rings defined by three carbon atoms. Since all these angles are slightly different in the *amphi*-PIC molecule, we simplified the calculations by using the benzene molecule as a model. Again, a one-dimensional PES was obtained from a series of quantum-chemical geometry optimization calculations, and the force constant of the bending motion of three adjacent carbon atoms in benzene was found to be 1855 kJ mol^{-1} rad^{-2}, a factor of 3.3 larger than the original value of 560 kJ mol^{-1} rad^{-2} for the GROMOS53A6 force field. As a check, we performed similar calculations for two angles of the *amphi*-PIC molecule itself. We obtained a force constant of 1894 kJ mol^{-1} rad^{-2} for the angle 18-21-20 and a force constant of 2075 kJ mol^{-1} rad^{-2} for the angle 19-16-17, corroborating the benzene result. Therefore, the force constants of all angles between three aromatic carbons of the *amphi*-PIC molecule were increased to 1855 kJ mol^{-1} rad^{-2}. The effect of this stiffening was a slight narrowing of the absorption spectrum.

In chapter 2, additional potential energy terms were added to the force field to improve the parametrization of the two dihedral angles ϕ_1 and ϕ_2. This was done by modifying the force field such that the quantum chemical PES was reproduced. To check whether these potential terms are still sufficient, we recalculated the PES for the new force field, without any changes to

	monomer	cylinder	ribbon
number of *amphi*-PICs	1	160	320
number of waters	7131	17890	35780
box size x (nm)	6.0	10.2	14.0
box size y (nm)	6.0	10.2	14.0
box size z (nm)	6.0	6.7	7.1

Table 3.1: Details of the MD simulations: number of *amphi*-PIC molecules (equal to the number of counterions) and number of water molecules in the simulation box, the box size in x-, y- and z-directions. The given values refer to the end of the respective equilibration runs.

the previously added potential energy terms for the dihedrals ϕ_1 and ϕ_2, as depicted in Figure 3.2 (see chapter 2 for the details of this calculation). Our new calculations show that both the location and the width of the minima of the quantum-chemical PES are well reproduced with the new force field, to approximately the same accuracy as in chapter 2, and thus the previously found terms for dihedrals ϕ_1 and ϕ_2 can be used without any further adjustments.

3.2.2 Molecular dynamics simulations

We performed simulations of both a single *amphi*-PIC monomer and of *amphi*-PIC aggregates. The starting configuration for the monomer simulations was obtained by randomly placing a single *amphi*-PIC molecule and a counterion in a cubic box with 6 nm sides, and then filling the remaining space with water molecules. First, a 10 ns equilibration run was performed (simulation details are provided in Table 3.1). The result was used as a starting point for four additional MD simulations: a 100 ns trajectory, with frames saved every 250 fs, was used to calculate the monomer's absorption spectrum, while three trajectories were used to calculate the autocorrelation function of the monomer's transition energies (see Section 3.3.1 for details).

In chapter 2, we obtained aggregate structures from MD simulations of the spontaneous aggregation process. Our system consisted of an equal number of positive *amphi*-PIC and negative perchlorate ions (see Figure 3.1) in water, typically of the order of 100. In the current study we calculate the electronic and optical properties of the cylindrical aggregate obtained in simulation 1 of chapter 2, and the ribbon-like aggregate obtained in simulation 5. However, since we have slightly modified the force field, 10 ns equilibration runs were performed for both the cylinder and the ribbon. As a starting point for the cylinder's equilibration run, we used the result of simulation 1 of chapter 2 after 660 ns of simulation time; for the ribbon the starting point was the result of simulation 5 after 760 ns of simulation time, with the box doubled in the z-direction to prevent molecules from interacting with their periodic image. The modification of the force field was observed to change neither the aggregates' shape nor their internal structure (see Appendix 3.5 for details). Using the result of the equilibration run as a starting point, two production runs were performed for the cylinder: (1) a 200 ps trajectory with frames saved every 4 fs, used to calculate the autocorrelation function of the transition energies and the couplings, and (2) a 40 ns trajectory with frames saved every 2 ps, used to calculate absorption and linear dichroism spectra, the density of states of molecular transition energies and eigenstates, and exciton participation numbers. Only one production run was performed for the ribbon: a 20 ns trajectory with frames sampled every 2 ps starting from the result of the equilibration run.

The MD simulations were carried out using the GROMACS program [87]. We integrated Newton's equations of motion using the leapfrog algorithm [88], with a time step of 2 fs for the monomer calculations and 1 fs for the aggregate calculations. Periodic boundary conditions were used for the simulation box. An atomistic description was used, except for the alkyl side chains (CH_3 and $C_{18}H_{37}$) of the *amphi*-PIC molecules, where the basic building blocks were CH_2 and CH_3 groups.

The LINCS method [89] was used to constrain all bond lengths. The nonbonded interactions were calculated using a twin-range cutoff scheme. All Lennard-Jones and electrostatic interactions within the short-range cutoff distance of 0.9 nm were evaluated at each time step, based on a pair list recalculated every 5 steps. The Lennard-Jones and electrostatic interactions within the long-range cutoff of 1.4 nm were calculated simultaneously with each pair list update and assumed constant in between. Electrostatic interactions beyond the 1.4 nm cutoff radius were corrected with a reaction field potential, with a relative electric permittivity ϵ_r of 54 [90].

In the aggregate simulations, the *amphi*-PIC and counterion molecules on the one hand, and the water molecules on the other, were coupled separately to a heat bath using a Berendsen thermostat [91]. In the monomer simulations all molecules were coupled to the same heat bath. A temperature of 298 K and a relaxation time of 0.1 ps were used. For the pressure coupling, the Berendsen scheme [91] was used, with a reference pressure of 1 bar, a relaxation time of 0.5 ps and a compressibility of 4.6×10^{-5} bar^{-1}. The monomer simulations used isotropic pressure coupling, while semi-isotropic pressure coupling was applied in aggregate simulations, so that the z-dimension of the simulation box (through which aggregates were connected to their periodic image) was coupled to the pressure bath seperately from the x- and y-dimensions.

3.2.3 Exciton Hamiltonian

We model the excited states of the *amphi*-PIC aggregates using a Frenkel exciton Hamiltonian. The two-level approximation is made, taking into account only the ground and the first electronic excited state of each dye molecule. The Hamiltonian in the site basis reads

$$H(t) = \sum_{n=1}^{N} E_n(t) b_n^\dagger b_n + \sum_{n,m=1}^{N} J_{nm}(t) b_n^\dagger b_m, \tag{3.1}$$

where the operator b_n ($b_n^\dagger$) annihilates (creates) an exciton at molecule n, E_n is the transition energy of molecule n, J_{nm} is the excitonic coupling between molecules n and m, and the summations run over all the molecules within the aggregate. The time-dependence of the Hamiltonian accounts for fluctuations in the conformation of the molecules and the solvent environment.

Transition energies were calculated using the semi-empirical ZINDO/S-CIS method, which has been shown to be an accurate and cost-effective method for calculating transition energies based on structures from MD simulations [23]. The nuclear coordinates of the dye molecule under consideration were taken to be the corresponding atomic coordinates from the MD simulation snapshot. To decrease the necessary computational effort, in the quantum-chemical calculations the *amphi*-PIC's methyl and $C_{18}H_{37}$ tails were replaced by hydrogen atoms; since the first excited state is of π-π character such a simplification is perfectly acceptable. The environment was taken into account in the form of static point charges, with positions and values taken from the MD trajectory. Point charges were only taken into account within a cutoff radius of 3 nm from the center of the chromophore under consideration, which we defined as

$$\mathbf{r} = (\mathbf{r}_9 + \mathbf{r}_{10} + \mathbf{r}_{11} + \mathbf{r}_{13} + \mathbf{r}_{14})/5, \tag{3.2}$$

where the atom numbering is shown in Figure 3.1.

We used the tight-binding approximation, neglecting the exchange contribution to the couplings, so that the excitonic coupling J_{nm} between molecules n and m equals the Coulomb interaction between the transition charge densities of these two molecules. We calculated the couplings using the TrEsp method [109], which approximates the transition charge density as a set of atomic transition charges fitted to best reproduce the electrostatic potential [110, 111]. The coupling between dye molecules m and n is then calculated as

$$J_{nm}(t) = \sum_{i=1}^{N_{at}} \sum_{j=1}^{N_{at}} \frac{1}{4\pi\epsilon_0} \frac{q_{mi} q_{nj}}{|\mathbf{r}_{mi}(t) - \mathbf{r}_{nj}(t)|}. \tag{3.3}$$

Here, q_{mi} and $\mathbf{r}_{mi}$ denote the atomic charge and position of atom i from molecule m, respectively, ϵ_0 is the electric permittivity of vacuum and summations run over all the atoms of molecules n and m. Detailed information on the calculation of the transition charges is available in Appendix 3.6.

3.3 Results and discussion

3.3.1 Amphi-PIC monomer

Comparison of the calculated absorption spectrum of the *amphi*-PIC monomer to experiment constitutes a test of our force field, specifically of its description of the internal motions of the *amphi*-PIC molecule and the *amphi*-PIC-water interaction. Also, it provides a test of the ZINDO/S-CIS method, which we used for calculating transition energies, as applied to the *amphi*-PIC molecule.

Depending on the magnitude and time scale of the fluctutations in the monomer's transition energy, the calculation of the absorption spectrum is more or less involved, with the static limit (slow fluctuations) being the easiest. In this limit, the spectrum can be expressed as

$$A(\omega) \propto \sum_i \frac{\gamma}{(\hbar\omega - E_i)^2 + \gamma^2}, \tag{3.4}$$

where ω is the angular frequency, E_i is the transition energy at time $t_i = i\Delta t$, with Δt the sampling time (see below), and γ is the HWHM of the Lorentzian peaks (for computational reasons, sampling is normally performed using many snapshots from the MD trajectory of a single dye molecule, since considering an ensemble of many dye molecules at one instance of time, as is done in the experiment, would have a huge computational cost). To establish the validity of this static limit, it is important to analyze the energy fluctuations, which we do now.

We first quantify the magnitude of the fluctuations of the monomer's transition energy. The calculated time average of the transition energy is $18\,267\,\mathrm{cm}^{-1}$, with a standard deviation of $\sigma = 749\,\mathrm{cm}^{-1}$. Next, we investigate the timescales of the fluctuations of the transition energies using the autocorrelation function. The autocorrelation makes use of the mean value of the transition energies, and thus depends on the duration of the trajectory which is used for the calculation, since this duration affects the value of the calculated mean transition energy. More specifically, for longer trajectories the deviation from the mean transition energy will be larger than for short ones, because additional slow fluctuations will be taken into account. To make the autocorrelation function as informative as possible for the description of excitonic processes, we need to choose a trajectory length that corresponds to the timescales of these processes. Therefore, the full trajectory is split into J partial trajectories which have a duration that captures the relevant excitonic processes, and preliminary autocorrelation functions are calculated seperately for each partial trajectory. Finally, to obtain better statistics, the autocorrelations of the partial trajectories are averaged to obtain the final autocorrelation function. This means that the autocorrelation function is defined as

$$C(t_k) = \frac{1}{\sigma^2}\frac{1}{J}\sum_{j=1}^{J}\left[\frac{1}{I-k}\sum_{i=1}^{I-k}\Delta E_j(t_k+t_i)\Delta E_j(t_i)\right], \tag{3.5}$$

where the label j runs over the J partial trajectories, each consisting of I snapshots, i runs over all available trajectory segments that have a duration of t_k, and $\Delta E_j(t) = E_j(t) - \bar{E}_j$ is the deviation from the mean energy during partial trajectory j.

When calculating the autocorrelation function, the sampling time Δt determines a trade-off between a fine sampling of the autocorrelation in time on the one hand, and good statistics and thus low noise on the other. To simultaneously achieve a dense sampling of the short-time part of the autocorrelation (so that its oscillations can be observed) and obtain a low level of noise, three MD trajectories were used. A 2 ns trajectory with snapshots saved every $\Delta t = 4$ fs was used to calculate the first 100 fs of the autocorrelation function, a second trajectory of 10 ns with snapshots saved every 20 fs was used for the interval between 100 fs and 2 ps, and a third trajectory with a length of 50 ns and a sampling time of 100 fs was used to calculate the autocorrelation in the interval between 2 ps and 10 ps. Each of these trajectories was split into 200 ps partial trajectories, after which the autocorrelation was calculated according to Eq. 3.5; The result is depicted in Figure 3.3a.

To gain insight into the timescales of the transition energies' fluctuations, the first 10 ps of the autocorrelation function was least-squares fitted with a sum of negative exponentials. Three negative exponentials were needed to obtain a good fit, resulting in a fit function of the form

$$C(t) = \sum_{i=1}^{3} a_i \exp(-t/\tau_i), \tag{3.6}$$

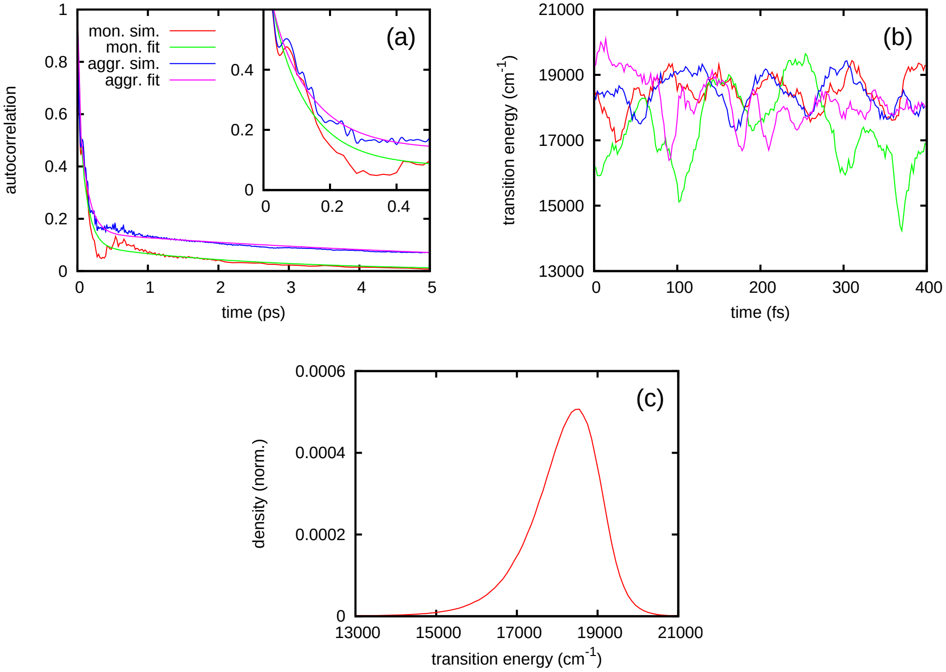

Figure 3.3: Analysis of the site transition energies. (a) The autocorrelation function of the site transition energies, for the *amphi*-PIC monomer and the cylindrical aggregate, fitted with tri-exponential functions. Inset shows the details of the first 0.5 ps. (b) Representative examples of the time evolution of the site energies of four different molecules in the cylindrical aggregate. (c) The distribution of transition energies in the cylindrical aggregate, normalized so that the area under the curve is unity.

with prefactors a_i normalized such that $\sum_{i=1}^{3} a_i = 1$. The parameters resulting from the fit are given in Table 3.2. The origin of the three dominant timescales, which can lie both in internal vibrations of the dye molecules or in intermolecular motions, will be discussed in Section 3.3.2.

We are now in the position to assess the validity of the static limit for calculating the absorption spectrum. The nature of a molecule's optical response is determined by the dimensionless parameter

$$\kappa = \frac{h\Lambda}{\sigma}, \tag{3.7}$$

where Λ^{-1} is the (dominant) timescale of the Hamiltonian and h is Planck's

	monomer transition energies	aggregate transition energies	aggregate couplings
τ_1 (ps)	0.011	0.011	0.26
τ_2 (ps)	0.11	0.12	11
τ_3 (ps)	2.4	6.9	-
a_1	0.26	0.29	0.61
a_2	0.64	0.56	0.39
a_3	0.10	0.15	-

Table 3.2: Parameters of a tri-exponential function fitted to the autocorrelation function of the transition energies (see Figure 3.3a) and a bi-exponential function fitted to the autocorrelation function of the couplings (see Figure 3.6b).

constant. For $\kappa \ll 1$, the static limit Eq. 3.4 is valid, while for $\kappa \gg 1$, the limit of fast fluctuations holds, with strong motional narrowing [112]. By far the most important timescale of the monomer's Hamiltonian, which constitutes 64 % of the fluctuations of the transition energy, is that of 110 fs; therefore, using Λ^{-1} =110 fs and σ =749 cm^{-1}, we obtain $\kappa = 0.4$. From this value we estimate that the calculated width of the absorption spectrum should be reduced by 14 % to correct our static approximation for motional narrowing [112]. Because the static limit represents a major computational simplification, we will use this approximation while keeping in mind that in reality the spectrum should be somewhat narrower than predicted by this model.

Figure 3.4 shows a comparison between the simulated and measured absorption spectra of the *amphi*-PIC monomer. The simulated spectrum was obtained employing Eq. 3.4, using a 100 ns trajectory, with snapshots saved every $\Delta t = 250$ fs, γ =10 cm^{-1} (in principle γ equals the inverse decay time of the excitation, which is 1.5 cm^{-1} for a monomeric decay time of 2.8 ns [55], but we used a larger value that smoothens the lineshape, yet is small enough not to widen the resulting spectrum), and the simulated absorption lineshape was blueshifted by 450 cm^{-1} to match the position of the experimental spectrum. The simulated spectrum compares well to the experimental one, the obvious lack of the vibronic progression in our result stems from the fact that we did not include the coupling of electronic excitations to vibrations. The width of the simulated spectrum overestimates the experimental value by roughly 20 %. The difference may be attributed mostly to the neglect of motional narrowing, while also inaccuracies in the MD structures may lead to an overestimation of

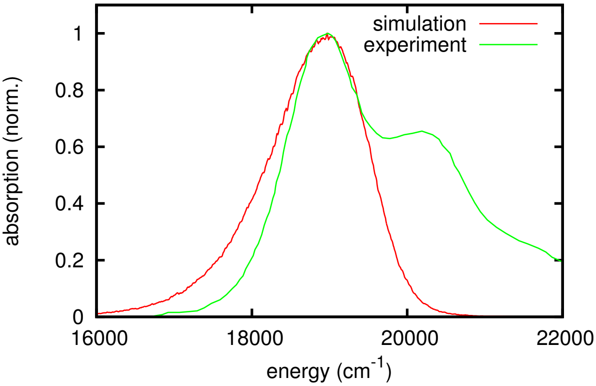

Figure 3.4: The simulated and experimental absorption spectra of the *amphi*-PIC monomer. The experimental data was taken from work by Sorokin *et al.* [79]. Spectra were normalized such that the maximum absorption values are unity, and the simulated spectrum has been blueshifted by 450 cm^{-1} to align it with the experimental spectrum.

transition energy fluctuations and thus to an overestimation of the width of the absorption spectrum [113]; we have already observed an extreme sensitivity of the absorption spectrum to structural inaccuracies when parametrizing the forces acting on the bridge between the *amphi*-PIC's quinoline rings (see Section 3.2.1).

3.3.2 Cylindrical aggregate

Transition energies

We now turn to the cylindrical aggregate, which has been obtained from MD simulations of the spontaneous aggregation process in chapter 2 (as explained in Section 3.2.2). Figure 3.3b illustrates representative examples of the time evolution of the site energies of 4 different molecules in the aggregate. Surprisingly, the transition energies exhibit large fluctuations of thousands of cm^{-1} in only several tens of femtoseconds. The magnitude of these fluctuations can be quantified using the distribution of transition energies, which is obtained by binning the transition energies of all molecules for every time step, as shown in Figure 3.3c. Conspicuously, the distribution of transition energies is asymmetric, with a long low-energy tail; the mean transition energy is 18 121 cm^{-1} while its standard deviation is 962 cm^{-1}.

To get more insight into the nature of disorder in the transition energies, we split it into two contributions: a dynamic and a static part. This terminology originates from stochastic models, which treat the transition energy of a molecule as the sum of a time-independent part (which differs per molecule) and a time-dependent part. Therefore, we define dynamic disorder as the fluctuations in the site transition energy of a single dye molecule; it is caused by fluctuations of the structure of the dye molecule itself as well as fluctuations of its environment. On the other hand, disorder between the mean transition energies of different molecules is denoted as static; this type of disorder is caused by local differences in the molecular packing of the aggregate. Such a partitioning of the disorder between static and dynamic components depends on the time span of the trajectory used for calculations, because the local aggregate structure slowly changes, thereby shifting the disorder from the static to the dynamic part for longer timescales.

Let us now give the relevant formulas. If we label the N *amphi*-PIC molecules by n and the I snapshots from the MD simulation by i, the average transition energy of molecule n is $\bar{E}_n = \sum_i E_{ni}/I$, while the average transition energy of all molecules is given by $\bar{E} = \sum_n \bar{E}_n/N$. Then, the standard deviation σ_{dyn} of the dynamic disorder can be expressed by

$$\sigma^2_{\mathrm{dyn}} = \frac{\sum_{ni}(E_{ni} - \bar{E}_n)^2}{NI}, \tag{3.8}$$

while the static disorder σ_{stat} is given by

$$\sigma^2_{\mathrm{stat}} = \frac{\sum_{n}(\bar{E}_n - \bar{E})^2}{N}. \tag{3.9}$$

The static and dynamic disorder are related to the total disorder $\sigma^2_{\mathrm{tot}} = \sum_{ni}(E_{ni} - \bar{E})^2/NI$ by the relation

$$\sigma^2_{\mathrm{tot}} = \sigma^2_{\mathrm{stat}} + \sigma^2_{\mathrm{dyn}}. \tag{3.10}$$

One of the timescales of the aggregates' exciton dynamics that can guide the choice of the time used for the partitioning between static and dynamic disorder is the exciton lifetime, which is 70 ps for the *amphi*-PIC aggregate [55]. Therefore, we use a 70 ps trajectory, and obtain $\sigma_{\mathrm{stat}} = 562\,\mathrm{cm}^{-1}$ and $\sigma_{\mathrm{dyn}} = 832\,\mathrm{cm}^{-1}$. Further analysis showed that these values change by less than 35 % when varying the trajectory length between 20 ps and 40 ns.

As in the case of the monomer, to assess the memory of the transition energies, we calculated the autocorrelation function according to Eq. 3.5, where the label j now runs over the N molecules in the aggregate and the average transition energies are calculated over all snapshots in the trajectory for each dye molecule seperately (see Figure 3.3a). The first 10 ps of the autocorrelation were fitted with a tri-exponential function, which yielded the parameters given in Table 3.2. We note that the aggregate's timescales of $\tau_1 = 11$ fs and $\tau_2 = 120$ fs correspond almost exactly to the monomer's timescales of $\tau_1 = 11$ fs and $\tau_2 = 110$ fs. Since the environment of a monomer and a molecule in the aggregate are very much different (water and possibly a single counterion for the monomer, against many other *amphi*-PIC molecules and counterions for the aggregate), these timescales apparently should be ascribed to the internal motions of the *amphi*-PIC molecules themselves rather than to fluctuations in the environment. This is plausible since angle bending modes can have periods as low as 20 fs [114] (the faster bond stretching modes are not accounted for in this chapter because all bond lenghts were fixed in our MD simulations). On the other hand, the slow timescale τ_3 differs considerably between monomer and aggregate; it equals 2.4 ps for the monomer, but 6.9 ps for the aggregate. Moreover, the slow fluctuations are more pronounced in the case of the aggregate, with $a_3 = 0.15$ for the aggregate against $a_3 = 0.10$ for the monomer. These differences point to the environment of the dye molecules as being, at least partially, the origin of the slow component of these fluctuations. The shorter timescale for the monomer might be due to the fact that water solvent, which constitutes its environment, is much more mobile than the rather inflexible aggregate structure. Interestingly, the two fastest timescales for *amphi*-PIC are similar to the timescales of 4 fs and 100-200 fs obtained for the FMO trimer [115], as well as those of 5-7 fs and 90-170 fs found for the LH2 complex [24]. Apparently, the fastest molecular motions have similar timescales over an entire range of dye molecules, which suggests a common origin of these timescales. Our relatively large value for the fastest timescale might be caused by the neglect of the fast bond stretching modes in our calculations.

Spectral density

Further information on the origin of the shape of the correlation function can be obtained by studying the spectral density $J(\omega)$, a quantity describing the frequency-dependent coupling between the excitonic states and the thermal vibrations of the environment. The spectral density is defined as [116, 117]

$$J(\omega) = \frac{\pi}{\hbar} \sum_{\xi} g_{\xi}^{2} \delta(\omega - \omega_{\xi}), \tag{3.11}$$

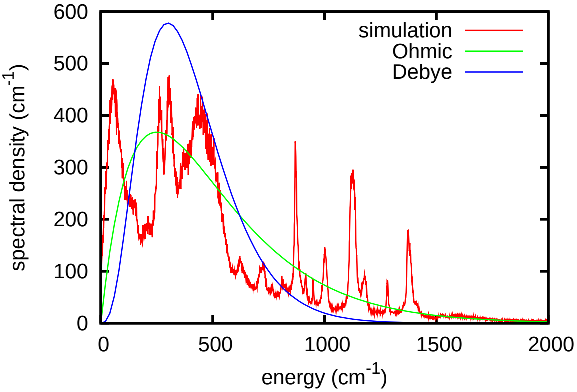

Figure 3.5: The spectral density of the cylindrical aggregate, as obtained from our simulations, fitted with Ohmic and Debye model densities.

where the sum runs over all phonon modes of the system, which have energies ω_ξ, while g_ξ is the dimensionless coupling constant between mode ξ and the electronic excitation of a single dye molecule within the aggregate. We calculated the spectral density from the transition energies' autocorrelation function $C(t)$ as [116]

$$J(\omega) = \sigma^2_{dyn} \frac{2}{\pi\hbar} \tanh(\hbar\omega/2k_B T) \int_0^\infty \mathrm{d}t\, C(t) \cos(\omega t), \tag{3.12}$$

where k_B is Boltzmann's constant and T the temperature. The resulting spectral density is plotted in Figure 3.5. Since the spectral density resembles a Fourier transform of the autocorrelation function, the broad background of the spectral density corresponds to the monotonically decaying part of the autocorrelation function, and can be ascribed to intermolecular modes, while the peaks in the spectral density correspond to oscillations in the autocorrelation, and belong to the intramolecular modes such as vibrations and rotations; this has also been shown numerically by Kleinekathöfer et al. [115] (as noted above, bond vibrations are not accounted for, and thus not visible in our spectral density).

In the phenomenological modeling of molecular aggregates, both the Ohmic [63, 118] and the Debye [119, 120] models for the spectral density are in common use. Now that we have obtained the spectral density of an *amphi*-PIC aggregate from first principles calculations, we can assess the validity of these model spectral densities. Combined with an exponential cutoff that ensures the spectral density to go to zero for large frequencies, the Ohmic spectral density is given by

$$J(\omega) = c\omega \exp(-\omega/\omega_c), \tag{3.13}$$

and the Debye spectral density is

$$J(\omega) = c\omega^3 \exp(-\omega/\omega_c). \tag{3.14}$$

In the above equations the prefactor c determines the peak magnitude of the spectral density, while the cutoff frequency ω_c determines the position of the spectral density's maximum. Fitting to the model spectral density yields $c = 4$ and $\omega_c = 250\,\mathrm{cm}^{-1}$ for the Ohmic spectral density and $c = 4.3 \times 10^{-4}\,\mathrm{cm}^2$ and $\omega_c = 100\,\mathrm{cm}^{-1}$ for the Debye spectral density; the results are plotted in Figure 3.5. The Ohmic model performs reasonably well on average, while the Debye model is unable to reproduce the high frequency tail of the simulated spectral density.

Excitonic couplings

In this section we discuss the excitonic couplings in the cylindrical aggregate, which were calculated as explained in Section 3.2.3. We start our analysis of the couplings by quantifying their magnitude. The average value (over all molecules) of the largest coupling of a dye molecule to any other molecule is $430\,\mathrm{cm}^{-1}$, while the average sum of all (absolute values of the) couplings to other dye molecules is $3104\,\mathrm{cm}^{-1}$ (which thus is an estimate for the total exciton bandwidth). Clearly, for every dye molecule there are many important couplings to its neighbors, due to the locally two-dimensional shape of the cylindrical aggregate.

The time evolution of the four largest positive couplings is depicted in Figure 3.6a. By comparison with Figure 3.3b it is immediately clear that the couplings fluctuate more slowly than the transition energies. We restrict our analysis of fluctuations to those couplings which have an absolute value larger than $400\,\mathrm{cm}^{-1}$ at the start of the production trajectory, since these couplings are the most important. As a measure for the magnitude of the fluctuations, we used the ratio of the couplings' standard deviation to their mean, which has an average value of $7.0\,\%$ (a $200\,\mathrm{ps}$ trajectory has been used for the calculation of the average, over which the π-π stacking between different *amphi*-PIC molecules remains stable).

In a similar manner as we did for the transition energies, we quantified the memory of the couplings using their autocorrelation function. The autocorrelation function was calculated according to Eq. 3.5, where the index j runs over all couplings with an absolute value greater than $400\,\mathrm{cm}^{-1}$ at the start of

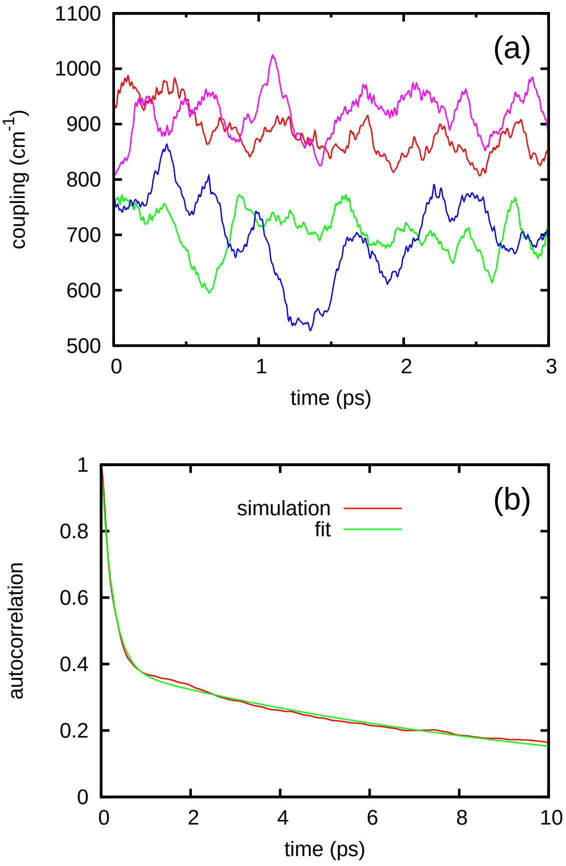

Figure 3.6: Analysis of the excitonic couplings in the cylindrical aggregate. (a) Time evolution of the four largest positive couplings. (b) The autocorrelation function fitted with a bi-exponential function.

the MD trajectory; the result is shown in Figure 3.6b. We performed a least-squares fit of the first 10 ps of the autocorrelation, using a sum of negative exponentials. Two exponentials were needed to get a good fit, resulting in a fit function of the form

$$C(t) = \sum_{i=1}^{2} a_i \exp(-t/\tau_i). \qquad (3.15)$$

The resulting parameters are reported in Table 3.2. The short 0.26 ps timescale of the couplings is of the same order of magnitude as the 0.11 ps one for the transition energies of the monomer and the 0.12 ps for the transition energies of the aggregate. The correspondence suggests that these timescales have the same origin, namely fluctuations of the internal structure of the dye molecules. Similarly, the long, 11 ps timescale of the couplings is of the same order of magnitude as the 2.4 ps and 6.9 ps for the transition energies. We previously ascribed these timescales of the transition energies, at least partially, to fluctuations in the intermolecular coordinates. The couplings too are influenced by the intermolecular coordinates, which determine the fluctuations of the orientation and position of the dye molecules, and thus indirectly the fluctuations of the couplings themselves.

Delocalization of exciton states

A commonly used measure for the number of molecules over which an excitonic state k is delocalized is given by its participation number, defined as

$$L_k = \left(\sum_{n=1}^{N} \phi_k(n)^4 \right)^{-1}, \tag{3.16}$$

where $\phi_k(n)$ represents the coefficient of the k'th eigenstate of the Hamiltonian of Eq. 3.1 (at a given time) at molecule n. The participation number equals unity when the exciton is fully localized on a single molecule, and it is of the order of the number of molecules N in the aggregate when the exciton is fully delocalized. The distribution of participation numbers we found for the excitons (eigenstates of the instantaneous Hamiltonian) in the cylindrical aggregate is given in Figure 3.7. The spread in participation numbers is large, ranging from states localized on a single molecule to those involving tens of molecules, with an average participation number of 14.3. The degree of delocalization might seem surprising, considering the substantial disorder in the transition energies and the lack of order in the internal structure of the aggregate. However, the cylindrical aggregate is effectively a two-dimensional structure, with each dye molecule having many neighbors; we have seen that as a result, the average sum (over all dye molecules) of all absolute couplings to other dye molecules is $3104\,\mathrm{cm}^{-1}$, which is much larger than the disorder in the transition energies of $\sigma_{\mathrm{tot}} = 962\,\mathrm{cm}^{-1}$. To conclude, we note that the very narrow peak around a participation number of unity is caused by outliers (molecules with a transition energy far from the mean), which are not in the vicinity of any other dye molecules with a similar transition energy.

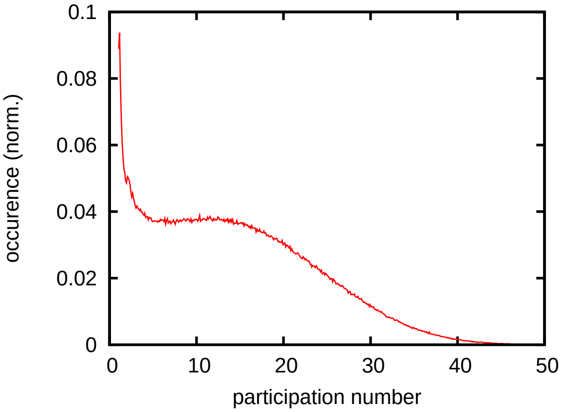

Figure 3.7: Histogram of the participation numbers of the cylindrical aggregate. The occurences have been normalized to make the integrated occurence equal to unity.

Aggregate absorption spectrum

Now that we have obtained the transition energies and couplings that govern the absorption spectrum, we are poised to calculate the spectrum itself. In the static limit, the aggregate absorption spectrum is a sum of Lorentzian lineshapes,

$$A(\omega) \propto \sum_{ik} O_{ik} \frac{\gamma}{(\hbar\omega - E_{ik})^2 + \gamma^2} \tag{3.17}$$

where O_{ik} is the oscillator strength and E_{ik} the energy of eigenstate k at time t_i, and we used $\gamma = 10\,\mathrm{cm}^{-1}$. The oscillator strengths were calculated as

$$O_k = \langle | \sum_n \phi_k(n) \boldsymbol{\mu}_n \cdot \mathbf{e}|^2 \rangle, \tag{3.18}$$

where $\langle \dots \rangle$ represents an orientational average over the polarization directions $\mathbf{e}$ of the electromagnetic field, invoked to account for an isotropic distribution of aggregate orientations. Finally, $\boldsymbol{\mu}_n$ denotes the transition dipole moment of molecule n, which is calculated from the atomic transition charges,

$$\boldsymbol{\mu}_n(t) = \sum_{i=1}^{N_{at}} q_{ni} \mathbf{r}_{ni}(t). \tag{3.19}$$

Our simulated absorption spectrum is plotted in Figure 3.8, together with the DOS (density of states) of the excitonic states and an experimental absorption spectrum of aggregates of *amphi*-PIC molecules measured by Sorokin *et*

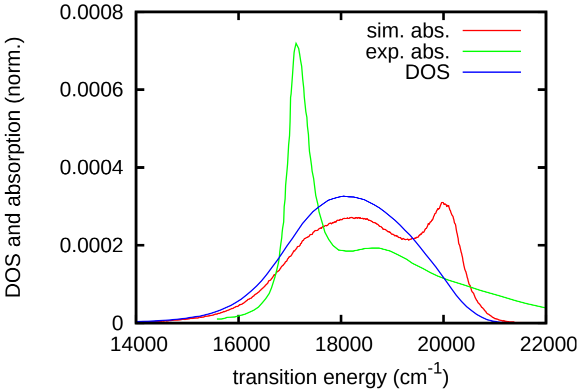

Figure 3.8: The simulated absorption spectrum of the cylindrical aggregate, the measured absorption spectrum taken from Sorokin *et al.* [79], and the density of eigenstates of the cylindrical aggregate. All curves were normalized, such that the area under each curve is unity.

al. [79]; the morphology of these aggregates was not determined in the experiment, though it was suggested that they have a cylindrical shape. The comparison of the calculated absorption spectrum with the corresponding DOS of the simulated cylinder, indicates that the cylinder has the character of an H-aggregate. However, the H-type behavior is not strong, as considerable oscillator strength is carried by states over the entire range of the exciton band, not only by the states at the band top. This result, which contrasts with experiment for many dye aggregates, finds it origin in the considerable structural and energetic disorder of the aggregate simulated here. The comparison to the spectrum measured by Sorokin et al. [79] is not very favorable. While the broad simulated spectrum exhibits a clear H band, the experimental spectrum has a relatively sharp J band. What complicates the comparison, is that it is not clear to what extent the higher lying band in the experimental spectrum is due to residual monomers, or mainly results from the aggregates.

In chapter 2, two distinct aggregate shapes resulted from MD simulations of the spontaneous aggregation process: a cylinder and a ribbon. From the MD simulations itself, it was not possible to decide which of these structures represents the equilibrium conformation. Now we can take another look at this question, by investigating whether the ribbon-like aggregate approaches the experimental spectrum better than the cylindrical one.

Before we discuss the spectral data itself, we shortly explain how the linear dichroism (LD) spectrum was calculated. LD reveals how the absorption of

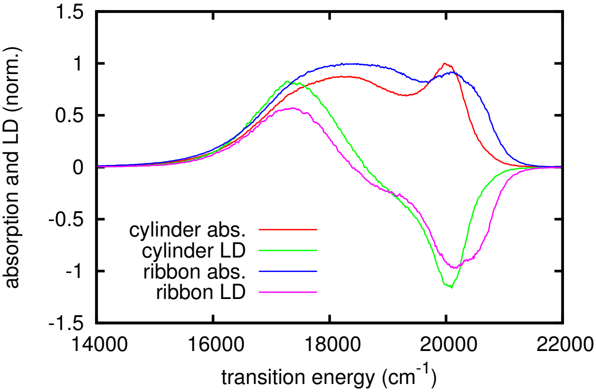

Figure 3.9: The absorption and linear dichroism spectra of the cylindrical aggregate and the ribbon-like aggregate. The spectra were normalized such that the maximum absorption values are unity.

light polarized in the direction of the aggregate axis differs from absorption of light polarized perpendicular to it; it is given by

$$LD(\omega) = A_{||}(\omega) - A_{\perp}(\omega) \propto \sum_k L_k \frac{\gamma}{(\hbar\omega - E_k)^2 + \gamma^2}, \tag{3.20}$$

where $A_{||}(\omega)$ denotes the absorbance parallel to the aggregate axis and $A_{\perp}(\omega)$ that perpendicular to the aggregate axis. If the aggregates are oriented in the z-direction,

$$L_k \propto \sum_{n,m} \phi_k(n)\phi_k^*(m)[(\boldsymbol{\mu}_n \cdot \mathbf{z})(\boldsymbol{\mu}_m \cdot \mathbf{z}) - \langle(\boldsymbol{\mu}_n \cdot \mathbf{e}_{\perp})(\boldsymbol{\mu}_m \cdot \mathbf{e}_{\perp})\rangle], \tag{3.21}$$

where $\langle \ldots \rangle$ represents the averaging of $\mathbf{e}_{\perp}$ over x- and y-orientations.

The resulting absorption and LD spectra of the simulated cylindrical and ribbon-like aggregates are shown in Figure 3.9. We observe that the spectra of the two aggregates are very similar, due to the large internal disorder of the aggregates which makes their spectra independent of their global shape. This we can show using a simple model aggregate for which the transition dipoles are randomly oriented.

Our model aggregate is a linear chain of 1000 dye molecules spaced 1 nm apart, with excited states described by a Frenkel exciton Hamiltonian as in Eq. 3.1. In the calculation of the couplings, each molecule was represented by a point-like transition dipole of 10 D, and the coupling between the point

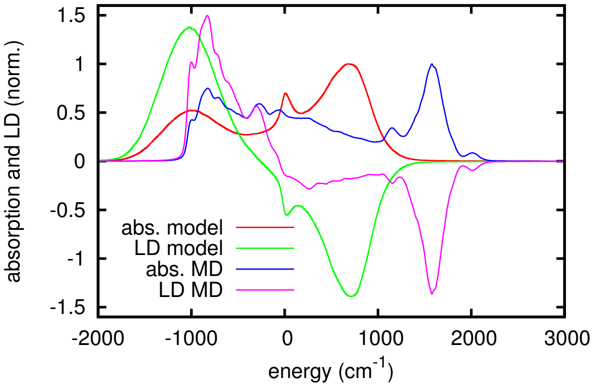

Figure 3.10: Absorption and linear dichroism spectra of the model linear aggregate with randomly oriented transition dipoles (*model*) and of the cylindrical aggregate, with all transition energies set to zero (*MD*). The spectra were normalized such that the maximum absorption values are unity.

dipoles $\boldsymbol{\mu}_m$ and $\boldsymbol{\mu}_n$ of molecules m and n is given by

$$J_{mn} = \frac{1}{4\pi\epsilon_0} \frac{\boldsymbol{\mu}_m \cdot \boldsymbol{\mu}_n - 3(\boldsymbol{\mu}_m \cdot \hat{\mathbf{r}}_{mn})(\boldsymbol{\mu}_n \cdot \hat{\mathbf{r}}_{mn})}{r_{mn}^3}, \tag{3.22}$$

where the intermolecular distance $\mathbf{r}_{mn} = \mathbf{r}_n - \mathbf{r}_m$ has length $r_{mn} = |\mathbf{r}_{mn}|$ and direction $\hat{\mathbf{r}}_{mn} = \mathbf{r}_{mn}/r_{mn}$. All transition energies were taken to be equal, $E_n = 0$, and the spectra were calculated by averaging over 1000 realizations of the random orientations of transition dipole moments.

The comparison of model spectra to those obtained from MD simulations for the cylinder is presented in Figure 3.10. Since the model aggregate has homogeneous transition energies, we also employed a homogeneous transition energy of 0 in the calculation of the cylinder spectra (so in the simulated Hamiltonian, only the couplings were calculated using the MD structure). Even though the shape of the cylinder and chain, as well as the number of nearest neighbors for a given molecule are completely different, the spectra are qualitatively very similar. This strongly suggests that the random orientation of the transition dipoles is the origin of the observed lineshapes of model chain and cylindrical aggregate.

3.4 Conclusions

We have used first principles calculations to obtain the absorption spectrum of both the monomer and the cylindrical aggregate of the *amphi*-PIC dye. Starting from structures obtained in MD simulations, we used quantum chemical computations to obtain the molecular transition energies and excitonic couplings that constitute the exciton Hamiltonian. This Hamiltonian, together with the dye molecules' transition dipoles which were also obtained from the MD structures, allowed us to compute absorption and linear dichroism spectra.

It was found that the generic force constant for improper dihedrals that is used in the GROMOS53A6 force field to keep $\pi-\pi$ systems in plane is not sufficient for reproducing the monomer's optical absorption spectrum; therefore, new force constants were obtained. Based on MD simulations with these new force constants, the exciton Hamiltonian was calculated, and its memory was characterized using the autocorrelation function; we obtained three timescales for the molecular transition energies and two for the couplings. Comparison of monomer and aggregate timescales taught us that the two fast timescales (11 fs and 120 fs for the transition energies, and 260 fs for couplings) could be identified as being caused by internal motions of dye molecules, while a third slower timescale (6.9 ps for transition energies and 11 ps for couplings) could be linked to intermolecular motions. The autocorrelation function was used to calculate the spectral density, revealing that the often-used Ohmic model for the spectral density corresponds better to our simulation data than the Debye model.

Comparison of the simulated absorption spectra with experiment gives mixed results. After modification of the force field, the simulated absorption of the *amphi*-PIC monomer approximates the measured absorption reasonably well; the quality of the simulated lineshape could be increased further in future work by inclusion of phonon sidebands. However, comparison between the absorption spectrum of the simulated cylinder and the experimental spectrum of an *amphi*-PIC aggregate shows that the simulated aggregate spectrum is too wide. The cause is a too disordered internal structure of the simulated aggregate, which was apparently not correctly reproduced by our MD simulations of the spontaneous aggregation process. We see two possible causes for this. First, the force field could lack the required accuracy. Compared with for example MD simulations of the spontaneous aggregation of lipid bilayers, our *amphi*-PIC molecules are less resemblant of those in the parametrization set of the force field. Also, the spectroscopic properties of the aggregate are probably more sensitive to the force field than the quantities which the force field was designed to reproduce (recall the huge effect of flattening the *am-*

phi-PIC's bridge on the width of its monomer spectrum, which has very little effect on the aggregate's structure). Second, there could be problems with the equilibration in MD simulations. This could be the case if the timescale of the formation of molecular order in the aggregate is much larger than our simulation time of hundreds of ns.

Obtaining the inner structure of molecular aggregates from MD simulations of the spontaneous aggregation process turns out to be a difficult endeavor. Possibly, more success could be obtained by first constructing an aggregate structure, using as input phenomenological models based on spectral data, and then using MD simulations to test the stability of these structures. In this way, information might be gained on aggregate structures while avoiding the pitfalls of simulating the spontaneous aggregation process, such as slow dynamics which may lead to equilibration problems. Also, using a force field that explicitly includes polarization might improve accuracy. This seems especially important for dye aggregates, since the charged nature of the dye molecules and counterions might make polarization play an important role.

By calculating the optical spectra of aggregates with 160 and 320 chromophores from first principles, we have shown that an ab initio approach can nowadays be applied to relatively large aggregates. To our knowledge, we are the first to obtain the optical properties of an aggregate of this size fully from first principles, including MD simulations of the spontaneous aggregation process. We have performed a first step towards using the first-principles approach as a tool that can provide information on variables that underlie the aggregates' optical properties, information that cannot be obtained by any other method.

3.5 Appendix: the effect of modifying the force field on the shape and internal structure of the *amphi*-PIC cylindrical aggregate

As described in the main text, in order to make the simulated absorption spectrum of the *amphi*-PIC monomer match experiment, we needed to modify the force field. Here, we investigate whether this change in force field has an effect on the structure of the cylindrical aggregate that we obtained in chapter 2, and which we used in the present chapter as a basis for calculating the exciton Hamiltonian and optical properties. For this analysis, we compared a 10 ns trajectory obtained with the original force field with a trajectory of the same length but for which the force field was switched to the new, modified one. As a measure for the global shape of the cylinder, we analyzed the cylinder's

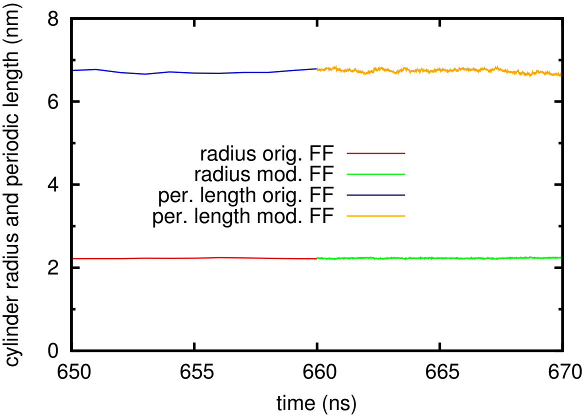

Figure 3.11: The radius and length of a periodic unit, for the cylindrical aggregate. At 660 ns, the force field was modified. Data for the initial part of the trajectory, obtained with the original force field (labeled *orig. FF*), was taken from chapter 2; data for the latter part of the trajectory corresponds to the equilibration run with the use of the modified force field (*mod. FF*).

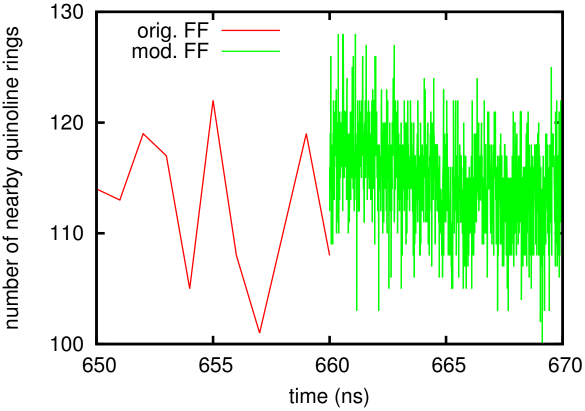

Figure 3.12: The number of quinoline ring pairs in the cylindrical aggregate with a separation smaller than 0.5 nm. At 660 ns, the force field was modified. Data for the initial part of the trajectory, obtained with the original force field (labeled *orig. FF*), was taken from chapter 2; data for the latter part of the trajectory corresponds to the equilibration run with the use of the modified force field (*mod. FF*).

radius and the length of a periodic cylinder unit (see Figure 3.11). To quantify the internal structure of the aggregate, we used the number of quinoline ring pairs that are within a cutoff separation of 0.5 nm (see Figure 3.12). We observed that neither the cylinder radius, nor its periodic length, nor the number of nearby quinoline rings changes after the force field was modified at $t = 660\,\text{ns}$. Even though the the modification of the force field changes the conformation of individual dye molecules, it turns out not to have an effect on the conformation of the aggregate as a whole.

3.6 Appendix: atomic transition charges

Atomic transition charges were needed for the calculation of the excitonic couplings with the TrEsp method, and for the calculation of transition dipole moments. We obtained these charges using the CHELP-BOW method [110, 111], which fits the charges to the electrostatic potential on a grid of randomly distributed points around the molecule. A symmetrized version of the amphi-PIC molecule was used, with the $C_{18}H_{37}$ tail replaced by a methyl group, whose geometry was optimized with the QChem program version 3.2 [86] in vacuum using a 6-311G* basis set and B3LYP functional.

Grid points were calculated using a code generously provided by Prof. Ulf Ryde. 105 000 grid points (2500 per atom) were randomly chosen within a maximal distance 0.8 nm from any atom. No minimal distance was needed since in CHELP-BOW method points with a Boltzmann weight lower than 10^{-6} are discarded. Next, the transition charge density and the resulting values of electrostatic potential on the grid were calculated with the QChem program version 3.2, in a TDDFT calculation with 6-311G* basis set and B3LYP functional. Subsequently, the atomic charges were determined by fitting to the electrostatic potential, again using a code supplied by Prof. Ulf Ryde. During the fitting procedure, the total transition charge was constrained to zero, and the transition dipole moment vector was constrained to the value of the TDDFT result (with transition dipole length of 9.6647 D). Atomic transition charges on side-chain hydrogen atoms were constrained to zero, because in our molecular dynamics simulations the side chain's CH_2 and methyl groups are treated as beads.

Finally, we scaled the atomic transition charges in order to reproduce the size of the measured transition dipole. The measured transition dipole was obtained from experimental data by integrating the absorption spectrum of the amphi-PIC monomer as measured by Malyukin *et al.* [121]. The oscillator

atom	charge (e)	atom	charge (e)	atom	charge (e)
1	0.0000486	14	-0.0036395	26	-0.0092783
2	-0.0411778	15	0.0446553	27	-0.0113596
3	-0.0278603	16	-0.0274678	28	0.0016716
4	-0.0067019	17	0.0485811	29	0.0092711
5	0.0194785	18	-0.0066983	30	0.0100318
6	-0.0411841	19	0.0161928	31	0.0057567
7	-0.0046459	20	0.0195775	32	0.0014754
8	-0.0461163	21	0.0480869	33	0.0061807
9	0.0074284	22	-0.0045631	34	0.0025160
10	-0.0174009	23	-0.0036656	35	-0.0404883
11	-0.0058098	24	-0.0045667	36	0.0410581
12	0.0007156	25	-0.0034657	37-42	0.0000000
13	0.0233611				

Table 3.3: The atomic transition charges of the *amphi*-PIC molecule. The atom numbering is given in Figure 3.13.

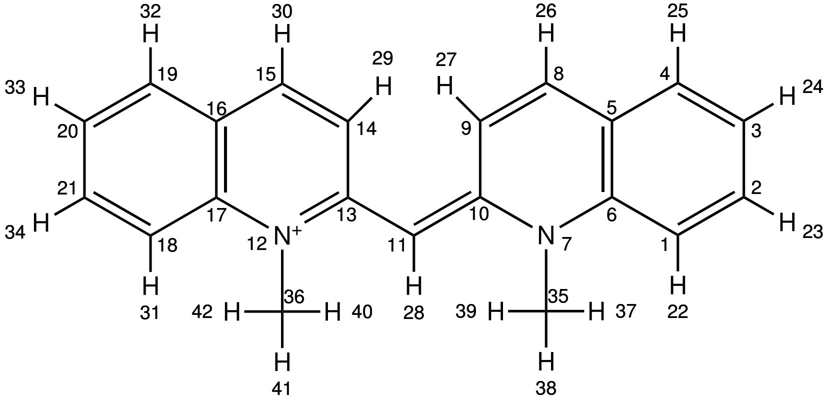

Figure 3.13: The symmetrized version of the *amphi*-PIC molecule used for the calculation of atomic transition charges, with the $C_{18}H_{37}$ tail replaced by a methyl group.

strength O was calculated from the integrated absorption spectrum,

$$O = 4.315 \cdot 10^{-9} \int \mathrm{d}k\, \epsilon(k), \tag{3.23}$$

where the wavenumber k is expressed in units of cm^{-1} and the molar absorption coefficient $\epsilon(k)$ is in $\mathrm{M}^{-1}\,\mathrm{cm}^{-1}$. From the oscillator strength, the transition dipole d was calculated using

$$O = \frac{4\pi m_e \nu}{3e^2\hbar} d^2, \tag{3.24}$$

where m_e is the electron mass, ν the frequency of the transition, which is determined from $\lambda = 527.5\,\mathrm{nm}$[122], e is the elementary charge and $\hbar$ is the reduced Planck's constant. The calculations yielded an oscilator strength of 0.678 and a transition dipole moment of 8.7 D. The atomic charges were thus scaled by a factor $8.7\,\mathrm{D}/9.6647\,\mathrm{D} = 0.90$ so that the measured dipole moment was reproduced. The resulting values of all atomic transition charges are given in Table 3.3.

Chapter 4

First-principles simulations of the initial phase of self-aggregation of a cyanine dye: structure and optical spectra[1]

Using first-principles simulations, we investigated the initial steps of the self-aggregation of the dye pseudoisocyanine (PIC) in water. First, we performed molecular dynamics (MD) simulations of the self-aggregation process, in which pile-of-coins oligomers ranging from dimers to stacks of about 20 molecules formed. The oligomer structures were found to be very flexible, with the dimers entering a weakly coupled state and then returning to a stable $\pi - \pi$ stacked conformation on a nanosecond timescale. The structural information from the MD simulations was combined with quantum chemical calculations to generate a time-dependent Frenkel exciton Hamiltonian for monomers, dimers, and trimers, which included vibronic coupling. This Hamiltonian, in turn, was used to calculate the absorption spectra for these systems. The simulated dimer spectrum compared well to experiment, validating the face-to-face stacked dimer arrangement found in our MD simulations. Comparison of the simulated trimer spectrum to experiment suggested that oligomers larger than the dimer cannot be abundant at the onset of J-aggregation. Finally, the

---

[1] This chapter is based on F. Haverkort, A. Stradomska, and J. Knoester, *J. Phys. Chem. B* **118**, 8877 (2014)

conformation of the PIC J-aggregate was investigated by testing the stability of several possible conformations in our MD simulations; none of the tested structures was found to be stable.

4.1 Introduction

The ordered structures that are formed by the self-aggregation of synthetic dye molecules have formed a flourishing area of research for decades [1, 2, 25, 27]. These molecular aggregates have been used as sensitizers in traditional photography [5, 6] and are promising building blocks for nanoscale functional materials, with applications such as light harvesting [16, 17], lasing [18, 19], and materials with nonlinear optical functionality [7–12]. Also, nature offers inspiration for self-aggregated functional systems: aggregates of dye molecules are used in photosynthesis by plants and light-harvesting bacteria to absorb sunlight and transport the resulting excitation energy to the photosynthetic reaction center [13–15]. In addition, molecular aggregates give rise to unexpected collective phenomena that are interesting from a fundamental viewpoint. Despite the continuing effort focused on molecular aggregates and the successes of phenomenological modeling, many questions remain unanswered, not only about the optical and energy transport properties of the aggregates themselves but also on the way the aggregates are formed. Here, we will focus on the initial stages of self-aggregation, using as object of our study the cyanine dye 1,1'-diethyl-2,2'-cyanine (pseudoisocyanine, PIC, see Figure 4.1). This was the first molecule for which J-aggregation was discovered [1, 2, 25, 27], and its aggregates are exemplary in the sense of yielding an exceptionally sharp J-band (i.e., an absorption band that is redshifted relative to the monomeric absorption spectrum).

In the past, several investigations of the initial steps of the aggregation process of PIC have been performed using spectroscopic techniques [123–126] (as well as examinations of similar dyes [127, 128]). These investigations found that, in the first stages of aggregation, several peaks appear on the blue side of the monomer absorption band, which are usually ascribed to dimers or larger oligomers with an H-aggregate character; as the aggregation progresses, a narrow and intense band appears on the red side of the monomer band, which is ascribed to the J-aggregate, and the other spectral bands decrease in intensity. This two-step aggregation process shows similarities to the nucleation-elongation mechanism by which some supramolecular polymers are formed [129]. It remained an open question how the transition from small oligomers with blueshifted absorption to large J-aggregates with redshifted absorption

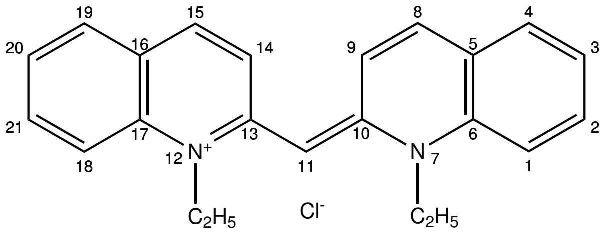

Figure 4.1: The PIC dye with chloride counterion.

takes place. Also, there is as of yet no certainty on the molecular structure of the PIC oligomers formed in the initial stages of aggregation, although a slipped stack model for the dimer structure has been proposed that could reproduce the dimer absorption spectrum reasonably well [123].

Another open question concerns the structure of the PIC J-aggregate. It is likely that multiple conformations exist depending on the experimental conditions, and many structural models for the aggregate have been proposed over the years [1]. For example, good fits to spectroscopic experiments have been obtained using one-dimensional aggregate models [64, 66, 130]. In addition, electron microscopy measurements revealed tubular J-aggregates formed by the PIC dye, with a diameter of about 2.3 nm [22, 131]; while this represents a major experimental advance, these techniques are not yet precise enough to image the stacking arrangement within the aggregate, and its resolution is not sufficient to observe monomers or small oligomers.

In this chapter, we address the above questions by means of first-principles modeling. First, using molecular dynamics simulations, we have witnessed the real-time aggregation of dye oligomers on an atomic scale, which cannot be observed experimentally; these simulations provided us with a model of the dimer structure distinct from the one proposed by Kopainsky et al. [123]. Subsequently, quantum chemical calculations of transition energies and excitonic couplings, performed on the basis of the MD structures, were combined with a model for the dominant excitonic states to yield the absorption spectrum of the PIC monomer, dimer, and trimer. Comparison of this simulated dimer spectrum with experiment allowed for verification of the MD dimer structure. In particular, we have shown that the origin of the different peaks in the dimer and trimer spectra can be explained using a simple model, which fully takes into account the intricacies of the intermediate-strength vibronic coupling (exciton-phonon coupling) operative in the PIC oligomers. Our approach of using first principles calculations has the great advantage that not only can we obtain ensemble properties, but also detailed information on the time evolution of single oligomers; this turned out to be essential for understanding the structure and optical properties of the PIC dimer. Finally, several structural models for the PIC J-aggregate were tested by assessing their stability in MD simulation.

The outline of this chapter is as follows. In Section II, we describe the force field and the details of the performed molecular dynamics simulations; we present our model for the excitonic states of the PIC oligomer and explain how that model is used to calculate absorption spectra. In Section III, we test our methodology by comparing simulations of the PIC crystal structure and monomer absorption spectrum to experiment. Then, we describe the outcome of our simulations of the spontaneous aggregation process and analyze the spectral properties of the PIC dimer and trimer. We investigate the structure of the PIC J-aggregate by testing the stability of several model structures in MD simulations. In the final Section IV, we summarize and conclude.

4.2 Computational details

4.2.1 Force fields

CHARMM Drude force field

We performed most MD simulations using the CHARMM Drude force field [132], which explicitly includes polarizability, unlike the modification of the GROMOS force field used in chapters 2 and 3. For water, the SWM4-NDP model was used [133]. A number of modifications had to be applied to the force field, as the PIC molecule is not fully parametrized in its standard version. Therefore, the atomic charges of the PIC molecule were fitted to the molecular electrostatic potential (ESP) with the CHELPG method [81], using version 2.9 of the Orca program. The fitting was performed using a regular grid with a spacing of 0.3 Å; grid points were included within a distance of 6 Å, but outside the COSMO van der Waals radii of the atoms. The ESP was evaluated using density functional theory with the B3LYP functional and the 6-31G* basis set, for the minimal-energy vacuum-phase geometry obtained at the same level of theory. Polarizabilities and Thole parameters (which determine the screening factor for dipole-dipole interactions between nearby atoms) for the PIC molecule's non-hydrogen atoms were taken from fully parametrized molecules containing similar chemical groups, such as pyridine and indole. Note that our procedure for obtaining atomic partial charges and atomic polarizabilities represents an approximation to the standard procedure for the CHARMM Drude force field, in which both partial charges and polarizabilities are determined in a single fitting procedure to the ESP. For bonds, angles, and dihedral angles, the values of similar, already parametrized, bonds and angles were used.

However, for the linker between the two quinoline moieties of the PIC molecule, no similar structures exist in the CHARMM Drude force field that could provide the parametrization. As a result, to keep the linker's carbon atom in plane with the quinoline rings to which it is bound, a harmonic potential with a force constant of $753.4\,\mathrm{kJ\,mol^{-1}\,rad^{-2}}$ was applied to dihedral angles 10-7-9-11 and 13-12-14-11 (see Figure 4.1 for the atom numbering). The value of this force constant was taken from our work in chapter 3 on the amphi-PIC molecule, which differs from the PIC molecule only in its hydrocarbon side chains. To describe correctly the twisting of the PIC molecule around its central bond, potential energy terms were added for the two dihedral angles ϕ_1 and ϕ_2, defined by atoms 10-11-13-14 and 13-11-10-9 (see Figure 4.1). Fitting to the quantum-chemical potential energy surface (PES, using the same methodology as in chapter 2, with a simplified version of the PIC molecule with ethyl tails replaced by methyl groups) yielded the energy function

$$U(\phi_1,\phi_2)/(\mathrm{kJ\,mol^{-1}}) = -8.368\cos(\phi_1)-30\cos(2\phi_1)-8.368\cos(\phi_2)-30\cos(2\phi_2). \tag{4.1}$$

These additional potential terms lead to a great improvement in the reproduction of the quantum-chemical PES, shifting the position of the absolute minimum to approximately the correct location (PES data is supplied in Appendix 4.5).

Because we observed in our preliminary MD simulations that hydrogen atoms bound to aromatic carbons of the PIC molecule were bending very much out of the plane of their respective quinoline rings, the improper force constant that keeps these hydrogens in plane was raised from 0.45 to $20\,\mathrm{kcal\ mol^{-1}\ rad^{-2}}$ (quantum chemical calculations for the corresponding angle in the benzene molecule resulted in an even larger force constant of $62\,\mathrm{kcal\ mol^{-1}\ rad^{-2}}$, but increasing the force constant to such a large value might destabilize the MD simulations).

GROMOS force field

For comparison with the CHARMM Drude force field, we have performed a small number of simulations using a modification of the GROMOS53A6 force field [80], which is described chapter 3.

4.2.2 Molecular dynamics simulations

MD simulations using the CHARMM Drude force field

MD simulations using the CHARMM Drude force field were performed with the NAMD program [134, 135]. To get rid of close contacts, all simulations were preceded by 1000 steps of conjugate gradient energy minimization, followed by a short simulation of 10 ps with a small 0.1 fs time step. Then, the time step could be increased to 0.5 fs. Attributing a small mass to the Drude particles allowed us to treat their propagation using an extended Lagrangian with a dual-Langevin thermostat; this generated a trajectory close to the self-consistent field limit [135]. The dual Langevin thermostat coupled non-Drude atoms to a heat bath at 298 K, using a damping coefficient of 20 ps^{-1}, while Drude particles were coupled to a heat bath at 1 K with a damping coefficient of 5 ps^{-1}. A Langevin barostat was used to control the pressure, with a target pressure of 1.013 25 bar, an oscillation timescale of 200 fs, and a damping timescale of 100 fs. Pressure coupling was applied isotropically in simulations of spontaneous aggregation and of separate monomers, dimers, and trimers; semi-isotropically in simulations of aggregates, with the dimension along which the aggregate was connected to its periodic image coupled separately to the pressure bath; and anisotropically to the simulation box filled half with crystal and half with water. We used periodic boundary conditions and, unless otherwise stated, a cubic simulation box with 6 nm sides.

Electrostatic forces were calculated using the Particle Mesh Ewald (PME) method, which mapped charges outside the cutoff radius of 1.2 nm to a grid, with a maximum spacing between grid points of 0.1 nm. Van der Waals forces were truncated beyond a 1.2 nm cutoff, while a switching function was applied between 1.05 and 1.2 nm to make the van der Waals potential decrease to zero in a smooth manner. Drude particles were coupled to all non-hydrogen atoms to allow for an explicit treatment of polarization. To prevent a polarization catastrophe, an additional quartic restraining potential with a force constant of 40 000 kcal mol^{-1} $\mathrm{Å}^{-2}$ was applied when the bond length between a Drude particle and its parent atom exceeded 0.2 Å. To save computational effort, NAMD uses an integration scheme with multiple time steps. In our simulations, nonbonded forces were only evaluated every two time steps, based on a pair list which was updated every 10 time steps. Pairs of atoms were included in the pair list within a cutoff distance of 1.35 nm. Moreover, bonded atoms that were connected through at most one intermediate atom were excluded from non-bonded interactions (1-3 exclusion). Bond lengths within the water molecules were held fixed using the Settle algorithm [136]. In the simula-

RMSD / nm	PIC	chloride	water	
CHARMM Drude	0.021	0.019	0.019	
GROMOS	0.051	0.026	0.036	
box size / nm (error)	a_x	b_x	b_y	c_z
experiment	6.793	0.09375	6.853	6.310
CHARMM Drude	7.1 (4.5 %)	0.097 (3.5 %)	6.9 (0.69 %)	6.4 (1.4 %)
GROMOS	7.0 (3.0 %)	0.097 (3.5 %)	7.1 (3.6 %)	6.5 (3.0 %)

Table 4.1: Assessment of the accuracy of the CHARMM Drude force field used in this chapter, and of a modified version of the GROMOS force field used in chapter 3, by testing the stability of the experimentally determined crystal structure in these force fields. The upper part of the table shows the root-mean-square deviation (RMSD) between simulated and experimental crystal structures. The lower part conveys the simulated and measured sizes of the simulation box, with the relative deviation of simulated values from experiment given in parentheses. Only nonzero components of the box vectors **a**, **b**, and **c** are given.

tions of self-aggregation and of the crystal, the screened Coulomb correction of Thole was applied to non-excluded, nonbonded pairs of Drude oscillators that were separated by less than 5 Å.

To build the starting configuration for our simulations of the PIC crystal, we used the experimentally determined crystal structure [137]. The unit cell was multiplied in the direction of the crystallographic unit vectors by factors of 5, 5, and 6, yielding a supercell (with box vectors **a**, **b**, and **c** denoted in Table 4.1 as ‘experiment’) which was used as the starting point of two MD simulations. The first simulation was performed to determine the equilibrium size of the simulation box; it had pressure coupling applied separately to all three box dimensions, and consisted of a 5 ns equilibration run followed by a 5 ns production run. A second simulation at constant volume was performed to obtain RMSD values, and consisted of a 1 ns equilibration run followed by a 3 ns production run.

To simulate the PIC monomer, we took the coordinates of a single PIC molecule and its nearest chloride counterion from the experimental crystal structure and then filled the rest of the simulation box with water. Then, we performed a 1 ns equilibration run which was the starting point for two further production trajectories: a 10 ns run with frames saved every 250 fs, which was used for the calculation of the monomer spectrum in the static limit, and a 200 ps trajectory sampled every 2 fs, from which the spectrum was calculated with the Numerical Integration of the Schrödinger Equation (NISE) method.

For our simulations of the PIC dimer, we selected two dimers (later on referred to as dimers a and b) that showed orderly $\pi - \pi$ stacked configurations from the results of the self-aggregation simulations. Both dimers were placed in a separate simulation box, to which counterions were added at random positions before the remaining open space was filled with water. Then, 1 ns equilibration runs were performed, followed by 5 ns production runs with frames saved every 250 fs, which were later used for analysis of the dimer conformation as well as for calculating absorption spectra in the static limit. For NISE calculations of the absorption spectrum, snapshots were made of both aforementioned production runs at 0, 2.5, and 5 ns. This yielded six starting configurations for 200 ps trajectories with snapshots saved every 2 fs. For the PIC trimer, simulations were performed in the same way as for the dimer.

We constructed several aggregate geometries that were used as a starting point for MD simulations that tested the stability of these structures. One of the aggregates consisted of a single strand of 12 PIC molecules and counterions that was taken from the crystal structure and then solvated with water; the resulting size of the simulation box was 8.2 nm along the direction of the strand and 6 nm in the other two directions. Another aggregate was built of four strands from the crystal structure and contained 48 PIC molecules and counterions; at the start of the simulation, its simulation box was described by the box vectors $\mathbf{a} = (6\,\mathrm{nm}, 0, 0)$, $\mathbf{b} = (0, 6\,\mathrm{nm}, 0)$, and $\mathbf{c} = (0.11\,\mathrm{nm}, 0, 8.2\,\mathrm{nm})$. Pile-of-coins aggregates containing 20 PIC molecules were constructed by multiplying self-aggregated dimers with an orderly $\pi - \pi$ stacking into the direction perpendicular to the molecular plane, placing counterions at random locations in the box, and filling the remaining space with water. Two such aggregates were built: one with all ethyl side groups of the PIC molecules oriented in the same direction, with initial box dimensions of 8.1 nm along the direction of the aggregate and 6 nm in the other two directions, and an aggregate with ethyl side groups on alternating sides, with box dimensions of 8.4 nm in the aggregate direction and again 6 nm in the other directions.

MD simulations using the GROMOS force field

MD simulations utilizing our modification of the GROMOS force field were performed with the GROMACS program [87]. Newton's equations of motion were integrated using the leapfrog algorithm [88]. A time step of 1 fs was used for simulations of the PIC crystal structure, and a time step of 2 fs for simulations of self-aggregation. An atomistic description was used, except for the ethyl side groups of the PIC molecules, for which the basic building blocks were CH_2 and CH_3 groups.

The lengths of all bonds were constrained using the LINCS method, except for simulations of the crystal structure, where only bonds including hydrogen atoms were constrained [89]. Non-bonded interactions were calculated using a twin-range cutoff scheme, in which Lennard-Jones and electrostatic interactions within a cutoff distance of 0.9 nm were evaluated directly at each time step, based on a pair list recalculated every 5 steps. On the other hand, electrostatic interactions beyond the 0.9 nm cutoff radius were calculated using the PME method, with a minimal spacing between grid points of 0.12 nm, cubic interpolation, and a relative strength of the Ewald-shifted direct potential at the cutoff radius of 1×10^{-5}.

Our system was coupled to a heat bath by a Berendsen thermostat [91] with a reference temperature of 298 K and a relaxation time of 0.1 ps. Pressure was controlled using a Berendsen barostat [91], with a reference pressure of 1 bar, a relaxation time of 0.5 ps, and a compressibility of 4.6×10^{-5} bar^{-1}. Pressure coupling was applied separately in all directions for the crystal simulations, while the coupling was isotropic for simulations of the spontaneous aggregation process.

The initial configurations for simulations of the self-aggregation process were prepared by randomly placing PIC molecules and counterions in the box and then adding water to fill the remaining space. The MD simulations that tested the stability of the PIC crystal for our modification of the GROMOS force field were performed in exactly the same manner as those using the modified CHARMM Drude force field, described in the previous section, with identical trajectory lengths and sampling rates.

4.2.3 Exciton Hamiltonian

We used a Holstein Hamiltonian to describe the vibronic excitations of PIC monomers and oligomers. For each dye molecule, we took into account one dipole-allowed electronic excitation (the lowest-energy and optically dominant one), linearly coupled to a single harmonic vibrational mode. Thus we assume that for a monomer, the curvature of the vibrational potential remains the same upon electronic excitation, but the position of its minimum is displaced along the vibrational coordinate. Then, the Hamiltonian for one-exciton states is given by

$$H(t)=\sum_{n=1}^{N}E_n(t)b_n^\dagger b_n+\sum_{n,m=1}^{N}J_{nm}(t)b_n^\dagger b_m+\hbar\omega_0\sum_{n=1}^{N}a_n^\dagger a_n+\hbar\omega_0\lambda\sum_{n=1}^{N}b_n^\dagger b_n(a_n^\dagger+a_n), \tag{4.2}$$

where $b_n^\dagger$ and b_n are the Pauli creation and annihilation operators of an electronic excitation at molecule n, $a_n^\dagger$ and a_n create and annihilate a vibrational energy quantum $\hbar\omega_0$ at molecule n (in the potential of the electronic ground state), E_n is the vertical excitation energy of molecule n, J_{nm} the excitonic coupling between molecules n and m, and λ^2 is the Huang-Rhys factor. Summations run over all N molecules within the oligomer. The time-dependence of the Hamiltonian is the result of fluctuations in the conformation of the molecules and the solvent environment. We assumed that these fluctuations do not affect the vibrations nor their coupling to the electronic transition.

To find the excited states of the Hamiltonian given in Eq. 4.2, we employed the two-particle approximation [138], in which the full one-exciton multiphonon basis set is truncated to include only states with at most two molecules excited. In the one-particle state $|n,\tilde{\nu}\rangle$, the molecule n is excited vibronically (i.e. electronically and vibrationally), with $\tilde{\nu}$ vibrational quanta in the displaced potential of the electronic excited state, while all the other molecules remain in their overall (electronic and vibrational) ground state. In the two-particle state $|n,\tilde{\nu};m,\nu\rangle$, apart from the vibronically excited molecule n, one more molecule (m) is excited purely vibrationally with ν vibrational quanta in the “unshifted” potential of the electronic ground state. Thus, the excited states of the aggregate are found as linear combinations of the one- and two-particle states:

$$|k\rangle=\sum_{n}\sum_{\tilde{\nu}=0}^{\nu_{max}}c_{n,\tilde{\nu}}^{k}|n,\tilde{\nu}\rangle+\sum_{n}\sum_{m\neq n}\sum_{\tilde{\nu}=0}^{\nu_{max}-1}\sum_{\nu=1}^{\nu_{max}-\tilde{\nu}}c_{n,\tilde{\nu},m,\nu}^{k}|n,\tilde{\nu};m,\nu\rangle. \tag{4.3}$$

The two-particle approach is numerically exact for dimers, as there are only two molecules constituting a dimer. It is an approximation for larger aggregates but has been shown to perform very well for molecular aggregates and crystals [139, 140].

We further truncated the basis set size by discarding states with more than 6 phonons in total ($\tilde{\nu}+\nu$). For the monomer and dimer, we tested that increasing the cut-off for the total number of phonons beyond 6 does not change spectra in any noticable way. We used a vibrational quantum of $\hbar\omega_0$=1368 cm^{-1} and a Huang-Rhys factor of $\lambda^2=0.605$, following Kopainsky et al. [123], who parametrized the vibronic states of the PIC monomer by fitting to its measured absorption spectrum.

We calculated transition energies using the semi-empirical ZINDO/S-CIS method, an accurate and computationally efficient method for calculating transition energies based on structures from MD simulations [23]. For the nuclear coordinates of the dye molecule under consideration, we used the corresponding atomic coordinates from the MD simulation snapshot. The nuclear dynamics then naturally leads to static and dynamic disorder in the transition energies. The necessary computational effort was reduced by replacing the PIC molecule's ethyl tails by hydrogen atoms, a plausible approximation since the first excited state is of π - π character. The environment was included in the form of static point charges, with positions and charges taken from the MD trajectory. Point charges were only taken into account for molecules located within a cutoff radius of 3 nm from the center of the chromophore under consideration.

In calculating excitonic couplings, we employed the tight-binding approximation, neglecting the exchange contribution, so that the coupling J_{nm} between molecules n and m equals the Coulomb interaction between the transition charge densities of these two molecules. Couplings were calculated using the TrEsp method [109], which approximates the transition charge density as a set of atomic transition charges fitted to best reproduce the "transition electrostatic potential" [110, 111]. The coupling between dye molecules m and n is then given by

$$J_{nm}(t) = \sum_{i=1}^{N_{at}} \sum_{j=1}^{N_{at}} \frac{1}{4\pi\epsilon_0} \frac{q_{mi} q_{nj}}{|\mathbf{r}_{mi}(t) - \mathbf{r}_{nj}(t)|}, \tag{4.4}$$

where q_{mi} and $\mathbf{r}_{mi}$ are the atomic transition charge and the position of atom i from molecule m, ϵ_0 denotes the electric permittivity of vacuum, and summations run over all atoms of molecules n and m. We used the same atomic transition charges for the PIC molecule as those used previously for the *amphi*-PIC molecule in chapter 3, since these molecules only differ in their hydrocarbon tails, which carry no transition charge. Note that transition charges were scaled to correspond with the oscillator strength of 0.678 obtained by integrating the *amphi*-PIC monomer spectrum (which is virtually identical to the PIC monomer spectrum). This oscillator strength differs from the value of 0.35 given by Kopainsky and coworkers for the PIC monomer [123]; we suspect that the difference is caused by Kopainsky et al. only taking into account the oscillator strength related to the 0-0 transition of the vibronic progression.

4.2.4 Absorption spectrum in the static limit

The computationally most efficient way of calculating the absorption spectrum from an MD trajectory is by using the static limit, which neglects the past dynamics of each MD snapshot, thus assuming a slowly varying Hamiltonian [112]. In this limit, the absorption spectrum is given by

$$A(\omega) \propto \sum_{ik} \langle |\boldsymbol{\mu}_{ik} \cdot \mathbf{e}|^2 \rangle f_{ik}(\omega) \tag{4.5}$$

where ω is the angular frequency, $\boldsymbol{\mu}_{ik}$ the transition dipole of instantaneous eigenstate k at time t_i, and $\langle \dots \rangle$ averages over the polarization directions $\mathbf{e}$ of the electromagnetic field. $f_{ik}(\omega)$ is a Lorentzian lineshape function with its mean located at the eigenenergy $\hbar\omega_{ik}$,

$$f_{ik}(\omega) = \frac{1}{\pi} \frac{\gamma}{(\hbar\omega - \hbar\omega_{ik})^2 + \gamma^2}, \tag{4.6}$$

where we have used a value of $\gamma = 10\,\mathrm{cm}^{-1}$ for the Half Width at Half Maximum (HWHM) (a value large enough to smoothen the lineshape but at the same time small enough not to influence the width of the overall spectrum). The transition dipole moments between the overall ground state and the eigenstates, $\boldsymbol{\mu}_k = \langle 0|\boldsymbol{\mu}|k\rangle$, are calculated using the expansion of $|k\rangle$ in the basis of one- and two-particle states given by Eq. 4.3. Since only the one-particle states have a transition dipole moment from the ground state, we obtain

$$\boldsymbol{\mu}_k = \sum_{n\tilde{\nu}} c^k_{n\tilde{\nu}} \boldsymbol{\mu}_n f_{\tilde{\nu},0}, \tag{4.7}$$

where the Franck-Condon factors $f_{\tilde{\nu},0}$ describe the overlap between two vibrational states, and are given by

$$f_{\tilde{\nu},0} = \frac{\lambda^{\tilde{\nu}} \exp\left(-\lambda^2/2\right)}{\sqrt{\tilde{\nu}!}}. \tag{4.8}$$

$\boldsymbol{\mu}_n$ denotes the transition dipole moment of molecule n, which is calculated from the atomic transition charges as

$$\boldsymbol{\mu}_n(t) = \sum_{i=1}^{N_{at}} q_{ni} \mathbf{r}_{ni}(t). \tag{4.9}$$

4.2.5 Absorption spectrum calculated with the NISE method

A more accurate way to calculate the absorption spectrum is the Numerical Integration of the Schrödinger Equation (NISE) method [141–143]. This method properly accounts for the history of each snapshot and therefore accounts for motional narrowing of spectral lines. Yet, the method is not exact, as it neglects the effect of changes in the electronic state of the dye molecules on their environment [144]. In the NISE method, the absorption spectrum is obtained from the linear response function, which is given by

$$R(t) = -\frac{i}{\hbar}\langle g(0)|\hat{\mu}(t)\hat{U}(t)\hat{\mu}(0)|g(0)\rangle\Gamma(t), \tag{4.10}$$

where $|g\rangle$ denotes the electronic ground state (without vibrations), $\hat{\mu}(t)$ the transition dipole operator, and the time evolution operator is given by

$$\hat{U}(t) = \exp_{+}\left[-\frac{i}{\hbar}\int_0^t \mathrm{d}\tau\, \hat{H}(\tau)\right], \tag{4.11}$$

where the exponent is positively time ordered. Decay of the electronic excitation is accounted for by the phenomenological relaxation factor $\Gamma(t) = \exp(-t/2T)$, with the lifetime of the singly excited states T =2.8 ns, as measured for the monomer of the amphi-PIC dye [55]. In order to obtain starting points for the calculation of the response function, the 200 ps MD trajectories were sampled every 20 fs. The absorption spectrum was then calculated as

$$A(\omega) = -\mathrm{Im}\int_0^\infty \mathrm{d}t\, R(t)\exp(-i\omega t). \tag{4.12}$$

For long times, limited sampling of the disorder in the site transition energies and the couplings causes noise in the response function. To prevent this noise from affecting the spectrum, the integral in Eq. 4.12 was calculated only up to 32 fs for the monomer spectrum, and up to 64 fs for the dimer and trimer spectra.

4.3 Results and discussion

4.3.1 Testing the force field: crystal structure and monomer spectrum

Before we performed production MD simulations, we validated our force field by testing the stability of the experimentally determined structure of the PIC crystal, which has been obtained using X-ray structure analysis by Dammeier et al. [137]. As an additional test, we simulated the absorption spectrum of the PIC monomer and compared it to the spectrum measured by Kopainsky and coworkers [123].

To test the stability of the crystal structure in our force field, we used the experimentally determined atomic coordinates as the starting point of MD simulations. The crystal structure was then observed to remain stable in all our simulations, of which the longest lasted 15 ns. As measures for the difference between the experimentally determined crystal structure and the equilibrated structure from MD, we used the deformation of the simulation box and the root-mean-square deviation (RMSD) of the crystal coordinates from their experimental values (see Table 4.1). The maximal deformation of the simulation box occurred in the x-direction, perpendicular to the strands comprising the crystal, and equaled 4.5 %. The average change in unit cell dimensions was 2.2 %; for comparison, this is in the upper range of the values reported by Nemkevich et al. for a set of small molecules and for several force fields [145]. In the simulation that was used to calculate the RMSD, the size of the simulation box was fixed at the experimental value. Before analyzing the MD results, thermal fluctuations were removed by averaging atomic coordinates over all 6000 snapshots of the 3 ns trajectory. In addition, the averaged MD structure was translated and rotated separately for each group of atoms considered (PIC, chloride, or water), to minimize RMSD values. An RMSD value of 0.021 nm was obtained for the PIC molecules, several times larger than the typical values reported by Nemkevich et al. [145]. This was to be expected, since the small molecules studied by Nemkevich et al. are more similar to the molecules used for parametrizing force fields than the larger and more complex PIC molecule.

To compare the performance of the polarizable CHARMM force field with that of the nonpolarizable GROMOS force field (which we used in chapters 2 and 3) in reproducing PIC properties, we have also used the GROMOS force field to simulate the crystal structure (the results are shown in Table 4.1). The GROMOS force field performs considerably worse than CHARMM, resulting in significantly larger RMSD values, especially for the PIC atoms, for which the RMSD value is 2.4 times bigger than the CHARMM result. Also, the deformation of the simulation box is larger for the GROMOS force field: the average change in unit cell dimensions of 3.2 % is 1.5 times bigger than the CHARMM result. We conclude that the CHARMM force field is considerably more accurate than GROMOS in reproducing the properties of the PIC crystal. This might be due to the polarizability, explicitly included in the CHARMM Drude force field but only implicitly included in GROMOS. It

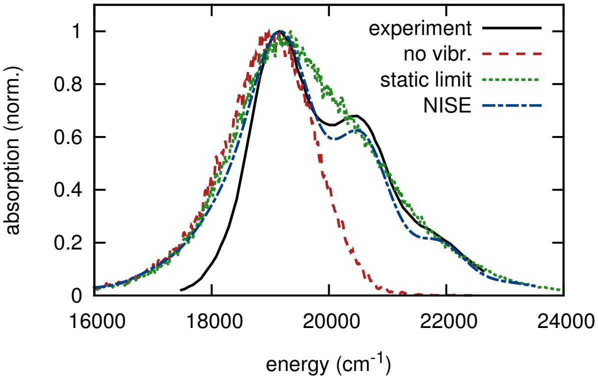

Figure 4.2: Absorption spectrum of the PIC monomer, according to experiment [123] (black solid curve) as well as our simulations at various levels of sophistication: NISE with explicit coupling to vibrations (blue long/short dashes), static limit with vibrations (green short dashes), and static limit without vibrations (red dashed curve). Absorption maxima were normalized to unity.

is well established that explicit inclusion of polarizability is important for an accurate description of highly charged systems such as the PIC crystal [146]. Our finding that the nonpolarizable GROMOS force field is relatively inaccurate supports the hypothesis that the too large degree of internal disorder of aggregates of the amphi-PIC dye, found in chapters 2 and 3, might have been due to inaccuracy in the used force field.

While simulations of the crystal structure tested mainly the PIC-PIC interactions within our force field, the interactions between PIC chromophores and water solvent, as well as our quantum-chemical calculations of transition energies, were checked by simulating the absorption spectrum of the PIC monomer and comparing to the measured spectrum [123]; the result is shown in Figure 4.2. The spectrum simulated with the NISE method approximates experiment well. Relative intensities and positions of the vibronic peaks are reproduced to a good accuracy, which was to be expected since the vibronic states were parametrized by fitting to the experimental monomer spectrum. The width of the 0-0 transition is accurate except for the too large low-energy tail. We expect this tail to be caused by inaccuracies in the force field, to which quantum chemical calculations of transition energies are very sensitive. A possible mechanism through which this inaccuracy could lead to a broadened spectrum is by causing a mismatch between MD and quantum-chemical equilibrium geometries of the chromophore [23, 113]. Also, the simulated spectrum had to be blueshifted by 500 cm^{-1} to make its peak position coincide with experiment, due to the well-known fact that the quantum-chemical ZINDO/S method, which we used to calculate the transition energies, does not correctly reproduce absolute energy values [23]. In order to correct for this systematic error of ZINDO/S for the PIC molecule, the 500 cm^{-1} blueshift was applied to all simulation results shown in this chapter.

In the static limit, the neglect of the motional narrowing effect causes the absorption spectrum to lack the resolution needed for discerning the separate peaks of the vibronic progression, leading to a significantly poorer performance than in the case of the NISE method. We also have calculated the monomer absorption spectrum in the static limit neglecting the coupling to a vibrational mode, which is practically equivalent to calculating the distribution of site transition energies (since each transition energy value contributes a Lorentzian peak with a HWHM of only 10 cm^{-1} to the spectrum). We can see that the transition energies fluctuate by 1000's of cm^{-1}, and that their distribution is asymmetric, with a longer tail on the low-energy side; we have found a similar result for the amphi-PIC dye in chapter 3, using a different force field than the one used here. Having been convinced of our force field's accuracy by its ability to reproduce both the experimental crystal structure and the monomer absorption spectrum, we are now poised to simulate the spontaneous aggregation process.

4.3.2 MD simulations of the self-aggregation process

We have studied the initial phase of the self-aggregation of the PIC dye in water by means of MD simulations, starting with PIC molecules and chloride counterions randomly distributed in water. We then observed that the dye molecules spontaneously assembled into multiple oligomers, which consisted of PIC molecules stacked in a pile-of-coins fashion, as depicted in Figure 4.3. The oligomers existed in a dynamic equilibrium, continuously forming, only to fall apart again later.

To quantify the amount of aggregation, we used the number of pairs of closely spaced quinolines n_q divided by the total number of molecules in the simulation box n_{mol}, as shown in Figure 4.4. The closely spaced quinolines were used as a measure for quinolines that are π - π stacked (these quantities are almost equal for the 0.5 nm cutoff radius we used for the quinoline center-to-center distance). To understand the meaning of this quantity, note that a face-to-face dimer has two closely spaced quinoline pairs. Thus, for a system consisting of only such dimers, $n_q/n_{mol} = 1$. For slipped dimers with only

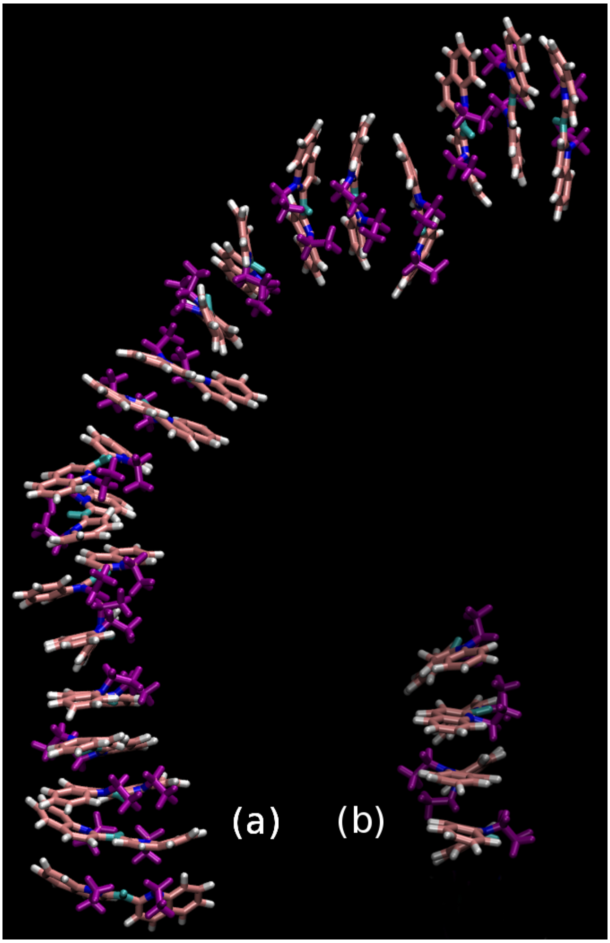

Figure 4.3: PIC oligomers with a pile-of-coins structure, formed in our MD simulations of the spontaneous aggregation process. (a) The largest self-aggregated structure that formed in our simulations, a pile of 19 PIC molecules. (b) A representative example of a PIC tetramer.

one quinoline per molecule facing its neighbor, $n_q/n_{mol} = 0.5$. Finally, if all the molecules in the box were part of a pile-of-coins aggregate with periodic boundary conditions, we would have $n_q/n_{mol} = 2$.

From Figure 4.4, it is clear that larger structures are formed when raising the dye concentration, in agreement with experiment [22]. The reason is that, at higher concentrations, there will be more collisions due to the oligomer's Brownian motion; on the other hand, the probability of an oligomer breaking

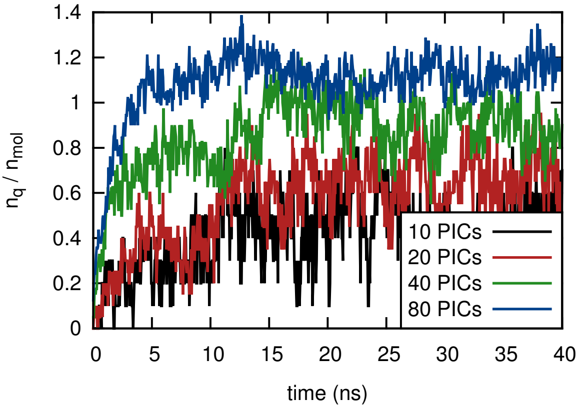

Figure 4.4: Characterization of the spontaneous aggregation process by the number of closely spaced quinoline rings n_q, corrected for the number of PIC molecules in the simulation box n_{mol}. Simulations were performed with 10, 20, 40, or 80 PIC molecules in the simulation box.

apart will not be affected by the dye concentration (as long as the dye concentration stays small enough so that oligomers do not influence each other). This causes a shift in the dynamic equilibrium, leading to larger structures. Also, our simulations show that the duration of the spontaneous aggregation process depends on the PIC concentration, with the aggregation taking place faster at higher concentrations. The aggregation lasted around 5 ns for the box with 80 PIC molecules, against 12 ns for the box of the same volume containing only 10 PIC molecules. The explanation is that at lower concentrations it takes more time before Brownian motion causes monomers or oligomers to collide, resulting in less possibilities for aggregate growth. We should note that the PIC concentrations used here are higher than in most experiments: with 10-80 PIC molecules in a 6 nm cube box, the concentration ranges from 0.077 to 0.62 M. The reason that we need a relatively high dye concentration in order to observe aggregation could be due to the limited number of dye molecules in the simulation box, which might change the dynamics of aggregate formation. Another possibility might be that the aggregation time is in reality much longer than the simulation times we can achieve in our simulations, and we are compensating for this fact by using a higher dye concentration; this view is corroborated by a measurement of the speed of formation of the PIC J-aggregate, which was found to be of the order of a minute [125].

The largest self-aggregated structure that formed in our simulations was a pile of coins consisting of 19 PIC molecules (shown in Figure 4.3a), which formed in our simulation with 80 PIC molecules; clearly, there is a considerable amount of structural disorder in its π - π stacking. With 20 PIC molecules in the simulation box, sizes ranging from monomers up to hexamers were observed, with the representative example of a tetramer depicted in Figure 4.3b. With 10 PICs, we observed mostly monomers and dimers. The history of the tetramer shown in Figure 4.3b gives a good impression of the dynamic equilibrium in which the oligomers exist: this tetramer had formed 15 ns earlier from the fusion of a trimer with a monomer. The newly formed tetramer existed as a chaotic stack for multiple nanoseconds before evolving into the more ordered stack depicted here. The monomer that took part in the tetramer formation, in turn, had broken away from a dimer 10 ns previously. The timescale of oligomer formation and breakup is thus of the order of 10 ns. Unlike in the MD simulations of *amphi*-PIC, described in chapter 2, most of the chloride counterions are not in close proximity to PIC oligomers but are instead located in the bulk water.

The formation of pile-of-coins stacks as the initial step of the self-aggregation process is corroborated by spectroscopic experiments. When the PIC concentration is raised from a value where only monomers exist in those experiments, the first change to the absorption spectrum is a shift to higher energies, ascribed to the formation of dimers and possibly larger oligomers [22, 147]. As we will see in Sections 4.3.3 and 4.3.4, PIC dimers and trimers which are stacked face-to-face have exactly this type of blueshifted spectrum. On the other hand, it is experimentally observed that when the dye concentration is increased further, a redshifted sharp J-band appears, polarized parallel to the aggregate axis [22, 147]. Since the PIC's transition dipole is oriented parallel to the molecule's long axis, this means that in the J-aggregate the PIC molecules must be aligned along the aggregate axis. The opposite is the case for the pile-of-coins arrangement of the oligomers observed in our simulations, where the long axis of the PIC molecule is perpendicular to the stacking direction. This means that there must be a particular aggregate size at which a structural reorganization takes place. Since we observe pile-of-coins oligomers of up to 19 molecules, our simulations of spontaneous aggregation suggest that the reorganization will take place beyond this size.

Next to our simulations utilizing the CHARMM Drude force field, we also performed simulations of the spontaneous aggregation process using a modification of the GROMOS force field. When a chloride counterion was used in these simulations, PIC oligomers formed, similar to our simulations with the CHARMM Drude force field, but with a somewhat smaller size of the PIC oligomers (less aggregation).

4.3.3 Absorption spectrum and geometry of the PIC dimer

Simulation of the absorption spectrum of the PIC dimer enables us to explain the origin of the experimental dimer spectrum, while at the same time the comparison of simulated and experimental spectra tests the dimer's face-to-face stacked conformation. Our simulated dimer absorption spectrum is shown in Figure 4.5a, together with the spectrum that was measured by Kopainsky and coworkers [123]. In order to match the experimental positions of the peaks, we applied a redshift of $100\,\mathrm{cm}^{-1}$ (on top of the $500\,\mathrm{cm}^{-1}$ blueshift which accounts for ZINDO/S inaccuracy for PIC); this aggregation shift accounts for non-resonant interactions with higher excited states and will be taken into account for all dimer and trimer results throughout the rest of this chapter. The NISE calculation reproduces the experimental spectrum to a large extent: the two peaks and the high-energy shoulder were reproduced at the correct positions and with approximately proper relative intensities. The good match between simulated and measured spectra is a strong indication of the correctness of the face-to-face conformation of the PIC dimer predicted by our MD simulations. Similar to the situation for the monomer spectrum, the static limit is still considerably less accurate than the NISE method.

As noted above, the NISE simulation does not reproduce the relative intensities of the experimental peaks exactly. The underlying reason is revealed by plotting separately the six contributions to the NISE spectrum (each arising from a different trajectory), as done in Figure 4.5b. We see that there are two types of spectra, corresponding to two types of dimer conformations. One kind is formed by dimers which are orderly $\pi - \pi$ stacked, as represented by trajectories 1, 2, 4, and 6 in Figure 4.5b. Trajectories 3 and 5 belong to the other species, which consists of dimers in an unstable conformation; as a result of their small excitonic coupling, these dimer spectra resemble those of the monomer. Indeed, we can see in Figure 4.6 that the starting structures of the dimer trajectories 3 and 5 (dimer a at 5 ns and dimer b at 2.5 ns, respectively; see Section 4.2.1) are relatively weakly coupled. We conclude that the inaccuracy of relative peak intensities in the averaged spectrum is probably due to inaccuracies in the sampling of the $\pi - \pi$ stacked and weakly coupled dimer species: comparing Figures 4.5a and 4.5b, we can see that the contribution of the weakly coupled species is underrepresented. Surprisingly, this suggests that the amount of time the dimer spends in a disordered and unstable conformation is even more than the two out of six instances that we sampled.

To get better insight into the origin of the peaks in the absorption spectrum of the ordered, strongly coupled PIC dimer, we performed a detailed

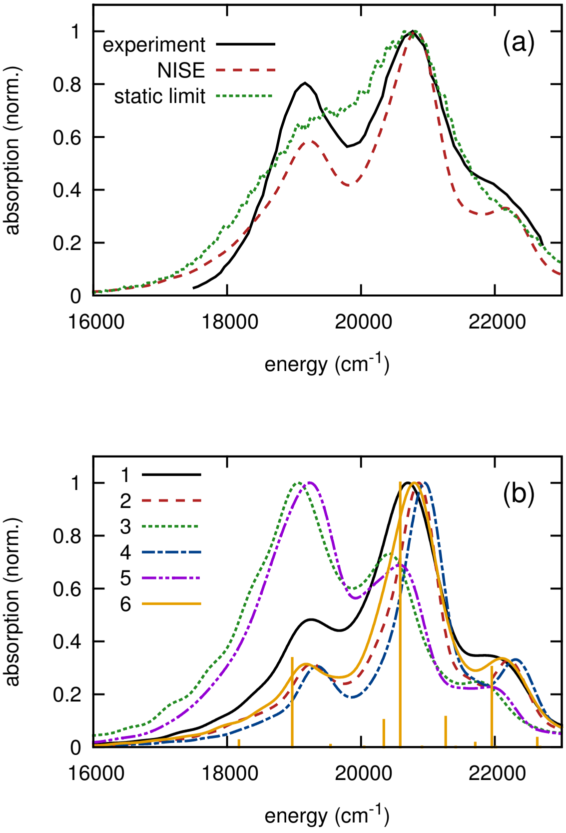

Figure 4.5: Absorption spectrum of the PIC dimer. (a) Obtained from experiment [123] (black solid curve) as well as simulated using the NISE method (red dashed curve) and the static limit (green dotted curve). Absorption maxima are normalized to unity. (b) Spectra of the six trajectories which were averaged over to obtain the NISE result shown in part (a). Trajectories 1, 2, and 3 were started from the configuration of dimer a at 0, 2.5, and 5 ns, respectively; trajectories 4, 5, and 6 used initial configurations from dimer b at the same times. The stick spectrum is the result of a simple dimer model, with parameters based on average values from trajectory 6. Note that the slight oscillations in the low-energy tail of some spectra are ringing artefacts, originating in the cutoff of the response function integral [112].

analysis of the excited states of a model dimer. This revealed that the experimental dimer spectrum, which consists of two peaks followed by a high

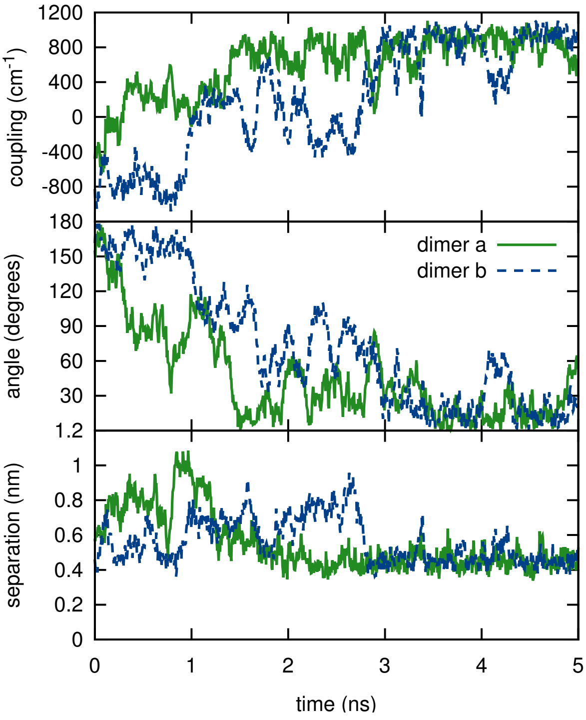

Figure 4.6: Characterization of the time evolution of two PIC dimers. (a) Excitonic coupling. (b) Angle between the transition dipoles. (c) Center-to-center distance.

energy shoulder, can be interpreted as originating mostly from excitations with an in-phase combination of transition dipole moments, accompanied by 0, 1, and 2 phonons, respectively. As is typical for H-aggregates, these states are blueshifted with respect to the monomer. The parameters for the model dimer were obtained by averaging over the representative trajectory 6, which yielded an excitonic coupling of $J = 956$ cm^{-1} and a 15° angle between the transition dipole moments of the two PIC molecules. The excitation energies of both molecules were assumed equal and taken as $18\,904\,\mathrm{cm}^{-1}$, which is the average value over both molecules from trajectory 6 (including both the blueshift due to ZINDO/S inaccuracies and the dimerization redshift); this assumption significantly simplifies the interpretation, as the excited states of a dimer can now be classified as either symmetric (+) or antisymmetric (-)

with respect to exchange of the two PIC molecules:

$$|k_\pm\rangle = \sum_{\tilde{\nu}=0}^{\nu_{max}} c^k_{\pm,\tilde{\nu}} \left(|1,\tilde{\nu}\rangle \pm |2,\tilde{\nu}\rangle\right) + \sum_{\tilde{\nu}=0}^{\nu_{max}-1} \sum_{\nu=1}^{\nu_{max}-\tilde{\nu}} c^k_{\pm,\tilde{\nu},\nu} \left(|1,\tilde{\nu};2,\nu\rangle \pm |2,\tilde{\nu};1,\nu\rangle\right). \tag{4.13}$$

The stick spectrum of this model dimer is shown in Figure 4.5b. Because of the small angle between the transition dipole moments of the two PIC molecules, the majority of the absorption intensity is carried by the transitions to symmetric states. The apparent discrepancy between the positions of the sticks and the maxima of the NISE-simulated spectrum for trajectory 6 is a result of our assumption of equal excitation energies of the two molecules building the dimer. When disorder is included, the symmetric and antisymmetric states of the dimer are coupled; in effect, the eigenstates are pushed away from each other: the low intensity antisymmetric states shift to lower energies, while the intense symmetric ones shift to higher energies, thus shifting the overall spectrum to higher energies.

As is typical for an H-type dimer, the lowest-energy excitation, at about 18 200 cm^{-1}, is to the antisymmetric state, with a total of 0 vibrational quanta (with a small, 6 % admixture, of the state with 1 vibrational quantum); however, due to its small transition dipole moment, this excitation contributes only little to the low-energy tail of the absorption spectrum. Most of the intensity of the first peak arises from the transition to the symmetric state, located at an energy of about 19 200 cm^{-1}. While being mostly (74 %) a 0-phonon state, it contains a significant admixture (20 %) of the 1-phonon states of both one- and two-particle origin, that is, states where the vibration is excited on the same molecule as the electronic excitation, as well as states with a vibration on the electronically unexcited molecule. The second absorption peak, at about 20 600 cm^{-1}, originates mostly from the excitation to the symmetric state with one vibrational quantum (76 %), with a substantial admixture of the 0-phonon state (22 %). This state has considerable contribution from 2-particle states (39 %). The high-energy shoulder arises from the transition to a symmetric state with a transition energy of about 22 000 cm^{-1} and with 2 vibrational quanta (76 %), mixed with a state with 1 vibrational quantum (23 %). The contribution from states with vibrations excited on the molecule which is in its electronic ground state (2-particle states) is even higher and reaches 51 %. The interpretation given above remains valid for the other 3 trajectories which correspond to strongly coupled dimers (trajectories 1, 2, and 4); the excitation energies differ from those of trajectory 6 by at most 170 cm^{-1}, while the contributions from states with different numbers of phonons change by no more than 6 %.

The non-negligible mixing of states with a different number of vibrational quanta, as well as the significant 2-particle character of the intensity-carrying states, are a signature of the breakdown of the strong vibronic coupling limit. This is not surprising, since the combination of having an average coupling $J = 956\ \text{cm}^{-1}$, a vibrational quantum $\hbar\omega_0 = 1368\ \text{cm}^{-1}$, and a Huang-Rhys factor of 0.605 makes the PIC dimer an excellent example of intermediate vibronic coupling. The effects are manifested as the strongly altered absorption intensity distribution as compared to the monomer, and as the increased splitting between the 0-0 and 0-1 line [148–150].

The time evolution of the dimer conformation can be studied by tracking the excitonic coupling, the angle between the two monomeric transition dipoles, and the PIC molecules' separation (taken as the distance between the two molecules' linker carbon atoms). The time dependence of these quantities is shown in Figure 4.6, for the two production runs that were also used to calculate the dimer absorption spectrum in the static limit. All three quantities are highly correlated, as we will discuss in more detail using dimer b as an example. Initially, the two PIC molecules are π - π stacked in an ordered manner (as depicted in Figure 4.7a); the coupling is strong and negative, which is due to the antiparallel orientation of the transition dipoles.[†] As should be the case for a dimer in a stable π - π stacked conformation, the center-to-center separation is small, only about 0.5 nm. At around 200 ps, one of the PIC molecules starts rotating around its long axis (see Figure 4.7b). At the time of rotation, a temporary increase in the center-to-center distance to 0.7 nm and a decreasing alignment of the transition dipoles is accompanied by a drop in the coupling strength. The dimer quickly returns to a stable state (Figure 4.7c), the excitonic coupling is strong, but now the ethyl sidegroups of the two dyes point in opposite directions. After 1 ns of simulation time, the dimer enters an unstable, weakly coupled state (shown in Figure 4.7d), which lasts about 2 ns. During this time, the alignment of the transition dipoles deteriorates, the separation between the chromophores increases up to 0.9 nm, and, as a result, the coupling strength oscillates around zero. Between 3 ns and 5 ns, the dimer is again in a stable state; during the unstable period, one of the transition dipoles has turned around, resulting in a parallel orientation which makes the coupling positive.

The PIC dimer is thus a highly volatile arrangement, which periodically leaves its stable π - π stacked structure and enters an unstable state, to return

---

[†] Even though the coupling is negative, this still is an H-dimer, as the optically allowed state is now (approximately) antisymmetric with respect to interchange of both molecules and therefore occurs above the monomer transition.

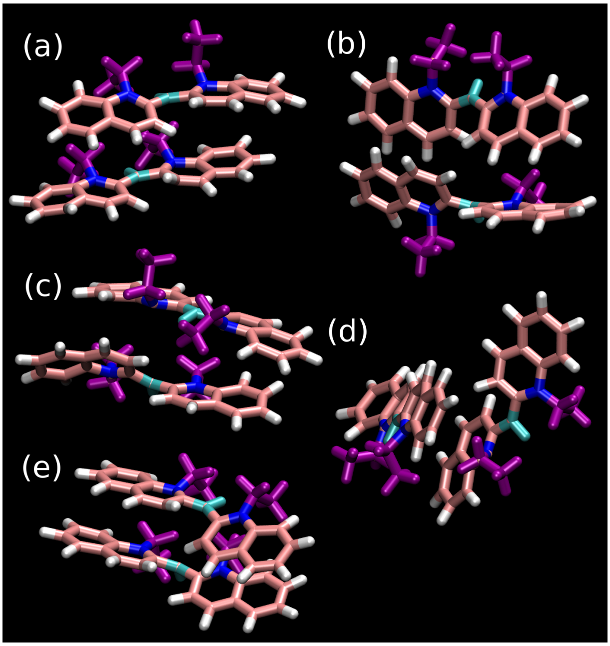

Figure 4.7: Several representative snapshots of dimer b from Figure 4.6. (a) 100 ps after the start of the production run: ethyl side groups of both PIC molecules are on the same side; (b) 200 ps: molecules are rotating with respect to each other; (c) 250 ps: after the rotation, ethyl side groups are located on opposite sides; (d) 2 ns: disorganized, unstable configuration of the dimer; (e) 5 ns: the dimer has stabilized and ethyl tails are back to the same side.

to stability soon after. The relative orientation of the transition dipoles, as well as that of the ethyl sidegroups, changes on a nanosecond timescale. This means that it is not accurate to model the dimer structure using a single value for the angle between the transition dipoles, as was done previously by Kopainsky and coworkers in their seminal work on the PIC dimer [123]. The importance of taking into account the variation in dimer conformations is demonstrated by the fact that Kopainsky et al. probably proposed an incorrect model structure based on their single, effective value of 70° for the angle between the transition dipoles: they suggested a sandwich dimer with only a single quinoline of each molecule π - π stacked to the other dye, instead of the structure with the whole dye molecule stacked face to face as found in this chapter. Note that, even though we conclude on a different dimer model than Kopainsky et al., the average absolute value of the coupling in our simulations, 641 cm^{-1} for dimer a and 584 cm^{-1} for dimer b, is very similar to their effective value of 630 cm^{-1} [123].

4.3.4 Absorption spectrum of the PIC trimer

We further investigated the self-aggregation process by simulating the absorption spectrum of the PIC trimer, shown in Figure 4.8a. As we did for the dimer, we applied an aggregation redshift of 100 cm^{-1} to all calculated trimer spectra (as well as a 500 cm^{-1} blueshift to correct for ZINDO/S systematic error). The trimer spectrum is qualitatively similar to that of the dimer, consisting of two peaks and a high-energy shoulder. The second, most intense peak of the NISE-simulated trimer spectrum lies 370 cm^{-1} higher than the corresponding peak of the dimer. This additional blueshift results from the coupling to a third chromophore; it is considerably smaller than the shift of 1620 cm^{-1} between the main peaks of the experimental monomer and dimer spectra. To investigate the variability of the NISE spectra between different trimer trajectories, we have plotted them for all six trimer trajectories that were averaged over to obtain the trimer absorption discussed above, as shown in Figure 4.8b. We see that the intensity of the first peak (around 19 200 cm^{-1}) is relatively large for some trajectories, and that these trajectories also show a somewhat smaller blueshift of their most intense peak; during these trajectories, the $\pi-\pi$ stacking must have been relatively weak. Note that there are no trajectories that have a spectrum similar to that of the monomer, in contrast to the dimer result depicted in Figure 4.5b; this must be caused by the trimer having two nearest-neighbor pairs instead of one, so that the chance is small that both pairs are simultaneously weakly coupled.

Similarly as for the dimer, we performed a detailed analysis of the eigenstates of a model trimer, for which the parameters were obtained by averaging over trajectory 4 (which yields the spectrum closest to the overall average). This resulted in an excitation energy (corrected for the ZINDO/S blueshift and aggregation redshift) of 19 105 cm^{-1}, excitonic couplings between the nearest neighbors of -832 cm^{-1}, and between the second neighbors of 205 cm^{-1}. The angle between the transition dipoles was taken as 157° and 45° for the nearest and second neighbors, respectively. Tentatively, the interpretation of the three peaks visible in the absorption spectrum is similar as in the dimer case, with the lowest peak resulting from 0-0 vibronic transitions associated with the three exciton states of the trimer, the second peak being predominantly the first vibronic replica, and the third peak being mostly the second vibronic replica. However, as the exciton bandwidth increases for the trimer as compared to the dimer, we move further away from the strong vibronic coupling regime toward the strong electronic coupling regime. In effect, for the trimer,

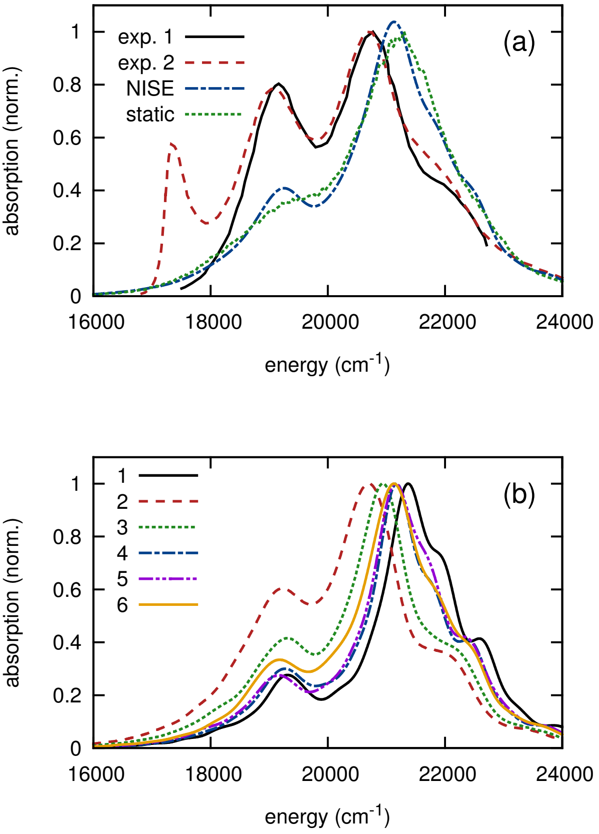

Figure 4.8: (a) Simulated absorption spectra of the PIC trimer, calculated in the static limit (green dots) and with the NISE method (blue dot-dashed curve), next to the dimer spectrum that was deduced from experiment by Kopainsky et al. [123] ("exp. 1", black solid curve), and the experimental spectrum that was measured at the onset of J-aggregation by von Berlepsch et al. [22] ("exp. 2", red dashed curve). (b) Spectra of the six trajectories which were averaged over to obtain the NISE result shown in part (a). Trajectories 1, 2, and 3 were started from the configuration of the first trimer at 0, 2.5, and 5 ns, respectively; trajectories 4, 5, and 6 used initial configurations from the second trimer at the same times.

both the description in the displaced oscillator basis of the strong vibronic coupling, as well as in the undisplaced oscillator basis of the weak vibronic coupling is cumbersome, and strong mixing of states characterized by different numbers of phonons is observed. We will present here the general picture, without going into intricacies of the intermediate coupling.

The lowest peak in the trimer absorption spectrum results from the transition between the ground state and three different excited states with 0 vibrational quanta. The lowest-energy one, at approximately 18 100 cm^{-1}, is associated with the exciton characterized by approximately out-of-phase transition dipoles. This out-of-phase character results from a combination of in-phase wavefunction amplitudes and an almost antiparallel orientation of the nearest neighbor transition dipoles (see above). As typical for H-aggregates, it carries little oscillator strength and thus forms a low-energy tail of the first absorption peak. A larger contribution comes from the second excitation at around 18 700 cm^{-1}, to a state related to the exciton characterized by a node on the central molecule. Most of the intensity of the first peak is carried by a transition at about 19 000 cm^{-1} to the exciton state for which the transition dipoles are all in phase (which is a result of out-of-phase wavefunction amplitudes combined with almost antiparallel transition dipoles on nearest neighbors). With the growing energy of those states, the admixture of one-phonon states grows (from about 7% to 26%), as does the two-particle character of the excitations (from 4% to 17%).

Most of the intensity of the second peak comes from the excitation at 20 800 cm^{-1} of the state which is mostly (70%) an in-phase combination of the electronic excited states of all molecules accompanied by a single vibrational excitation, with a considerable admixture (18%) of 0-phonon states. Compared to the situation in the dimer, the two-particle contribution is larger (54%). The third peak (a shoulder on the high-energy side of the main peak) is due to the 2-phonon states, considerably mixed with 1- and 3-phonon states.

Comparing the calculated trimer spectrum to experimental data might give us information on its abundance in experiment. To this end, in Figure 4.8a we have plotted the simulated trimer spectrum together with the experimental dimer spectrum and the spectrum measured at the onset of J-aggregation. It is clear that, at the onset of aggregation, large contributions to the spectrum are made by the PIC dimer and J-aggregate. However, the accuracy of available data is not sufficient to determine if there are also smaller contributions from trimers, larger oligomers, or monomers. If these species exist at the onset of aggregation, it seems likely that they will be far less prevalent than the dimer.

From Figure 4.8a we can see that the static limit result for the trimer absorption spectrum approaches the more accurate NISE result; in contrast, the static limit performed significantly worse than NISE for the monomer and dimer (see Figures 4.2 and 4.5a). The static limit thus seems to become increasingly accurate with increasing oligomer size. Two mechanisms may be at play. First, exchange narrowing starts playing a role with increasing oligomer size, and this might diminish the importance of the motional narrowing which is neglected in the static limit. Second, the separation between the most intense peaks increases from $1290\,\mathrm{cm}^{-1}$ for the monomer, to $1494\,\mathrm{cm}^{-1}$ for the dimer, and to $1857\,\mathrm{cm}^{-1}$ for the trimer (the values are given here for the NISE results). This increased separation will make each distinct peak more visible, even when the static limit overestimates the width of individual peaks.

4.3.5 Stability of PIC aggregates

Our simulations of the spontaneous aggregation process did not show a structural transition from H-oligomers with a pile-of-coins geometry to large J-aggregates. Therefore, we took a different route to investigate the structure of the PIC aggregate: we tested the stability of model structures in MD simulation. We chose four promising structural motifs for the PIC aggregate: (1) a pile-of-coins geometry with all ethyl side groups of the PIC molecules located on the same side of the aggregate, (2) a pile-of-coins geometry with ethyl side groups of neighboring dyes located on alternate sides of the aggregate, depicted in Figure 4.9a, (3) a single strand from the experimentally determined crystal structure, which was used in the past as a one-dimensional model of the J-aggregate, [151] shown in Figure 4.9b, (4) a thread consisting of four such strands, suggested by cryo-TEM images of rodlike PIC aggregates from von Berlepsch et al. [22], depicted in Figure 4.9c. Structures (1) and (2) were suggested by our simulations of the self-aggregation process, and are similar to the previously proposed ‘staircase’ model of a slipped stack of dyes [152]. All aggregates were connected to their periodic images in the direction of the aggregate axis, which should greatly diminish any finite size effects. Unfortunately, none of the investigated aggregate types turned out to be stable. The strands from the crystal structure fell apart into a number of oligomers with a pile-of-coins geometry, which were similar to those formed in our simulations of the spontaneous aggregation process, and the pile-of-coins aggregate broke apart into smaller segments. To make sure that any assembly of strands from the crystal is unstable in our force field, a MD simulation was performed with half the box occupied by the crystal structure and half filled with water solvent. The result was that the crystal started falling apart; within 20 ns, most of the crystal had dissolved into the water to form pile-of-coins oligomers, as shown in Figure 4.10.

Our simulations thus suggest that PIC aggregates do not consist of strands like those in the crystal structure, where the quinoline rings are π - π stacked

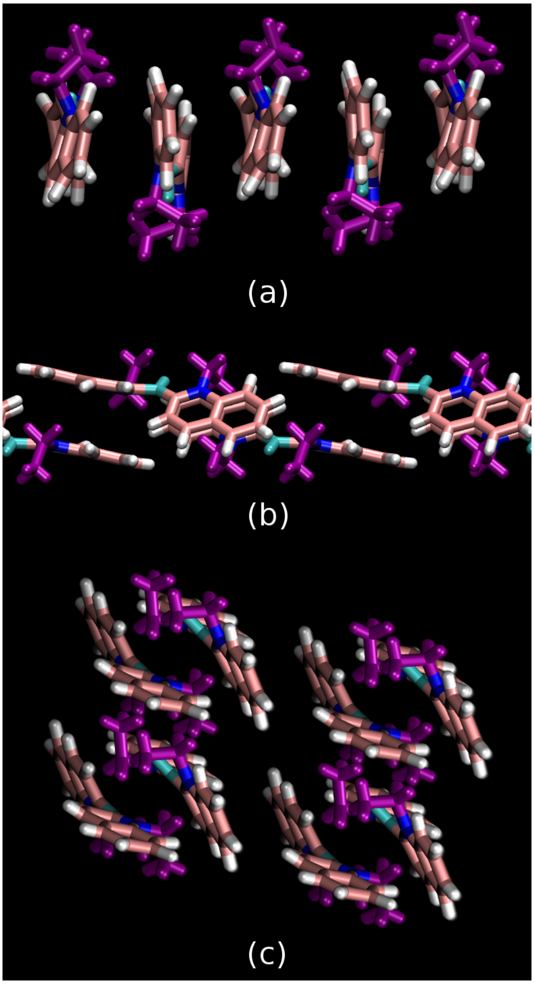

Figure 4.9: Three possible geometries of the PIC aggregate for which we tested the stability in MD simulations. (a) Pile-of-coins stack with the PIC molecules' ethyl side groups located on alternating sides of the aggregate. (b) Single strand, with quinoline rings π - π stacked in a parallel-displaced manner, taken from the experimentally determined crystal structure. Side view. (c) Four strands from the crystal structure. Top view.

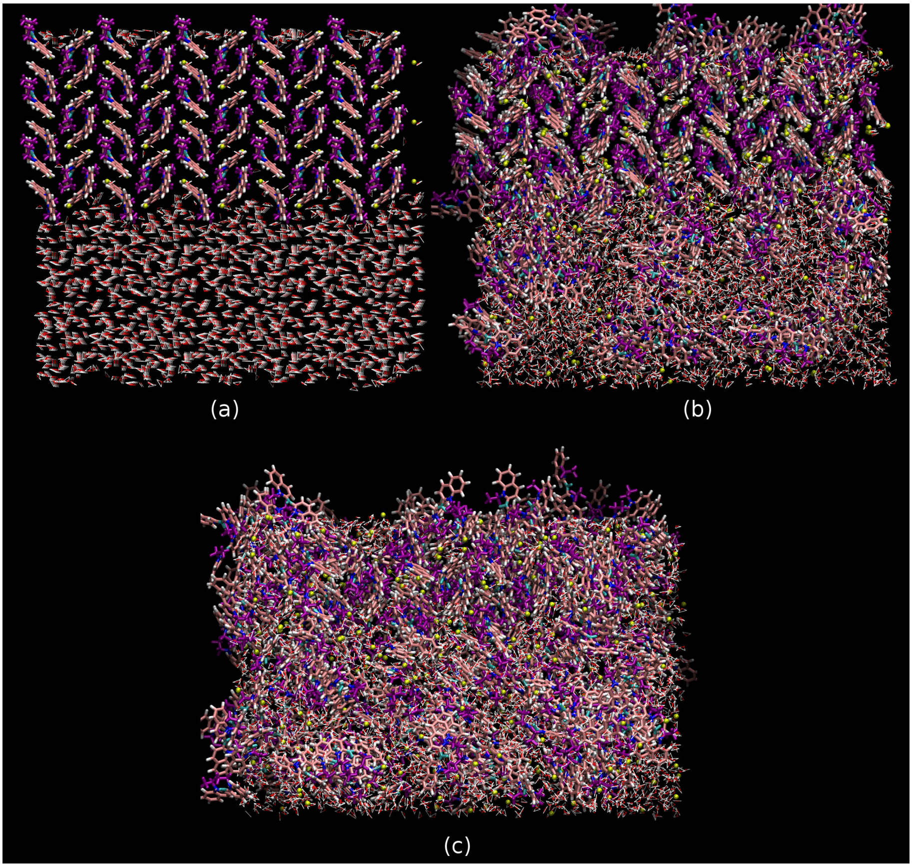

Figure 4.10: Snapshots from a MD simulation starting with half the simulation box occupied with PIC crystal, and the other half with water solvent. (a) Initial configuration. (b) After 10 ns. (c) After 20 ns.

in a parallel-displaced manner, nor do they have a pile-of-coins geometry. An alternative could be that the rods imaged by Berlepsch et al. are cylinders consisting of a monolayer or a bilayer of PIC molecules (where in the bilayer the ethyl tails would be shielded from the water solvent); this type of structure has been used successfully to explain the spectroscopy of the C8S3 aggregate [59]. On the other hand, we cannot exclude the possibility of a realistic aggregate structure being unstable in our MD simulations, due to the approximate nature of the force field approach.

4.4 Conclusions

We have studied the initial steps of the spontaneous aggregation process of the PIC dye in water using MD simulations and spectral modeling. First, we tested our methodology by verifying the stability of the experimental structure of the PIC crystal in our force field, and by comparing the simulated absorption spectrum of the PIC monomer to experiment. We learned that the CHARMM Drude force field used in this chapter reproduces the PIC crystal structure considerably better than the GROMOS force field used in chapters 2 and 3 for the related amphi-PIC dyes. Then, we performed molecular dynamics simulations of the self-aggregation process, in which pile-of-coins stacks of up to 19 dyes were formed.

The dimer spectrum compared favorably to experiment, corroborating the simulated dimer's face-to-face stacked geometry, which differs from the classical structure proposed by Kopainsky et al. [123]. The dimer structure was found to be very flexible, switching between a stable $\pi-\pi$ stacked state and a weakly coupled state every few nanoseconds. This fact has important implications for the dimer absorption spectrum, which turns out to be a superposition of two types of lineshapes: one belonging to an orderly $\pi-\pi$ stacked structure and one similar to the monomer lineshape of the weakly coupled dimer. Taking into account structural fluctuations thus turns out to be essential for understanding the dimer spectrum. In contrast, the spectral contribution of orderly $\pi-\pi$ stacked structures could be understood using a static vibronic model, which allowed us to elucidate the origin of each peak observed in experiment, and showed that the dimer resides in the intermediate vibronic coupling regime. Next, we simulated the trimer spectrum and compared it to the experimental spectrum at the onset of J-aggregation, from which we could conclude that in experiment trimers and larger oligomers, if they are present at all, are probably not prevalent.

It is difficult to assess up to which size pile-of-coins oligomers grow in experiment. The experimental spectrum that we used does not give any evidence for the existence of H-type structures larger than the dimer at the onset of aggregation; on the other hand, it is difficult to believe that there are no intermediate structures between H-type dimers and large J-aggregates. Additional insights might be gained using novel spectroscopic techniques such as 2D spectroscopy, which can help determine which spectral peaks are due to the aggregate and which to other species at the onset of aggregation. In addition to the process by which aggregates are formed, also the aggregate structure remains an open question.

4.5 Appendix: additional potential energy terms for the PIC linker

As explained in section 2.1.1 of the main text, we have added additional potential energy terms to the standard CHARMM Drude force field in order to accurately describe the forces acting on the linker between the quinoline moieties of the PIC molecule. Using the quantum-chemical DFT method as a benchmark, the resulting great improvement in accuracy is shown in Figure 4.11.

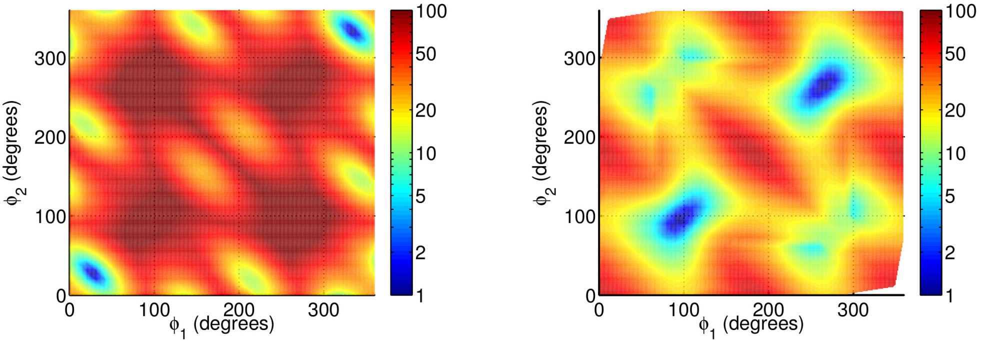

(a) quantum chemistry

(b) standard force field

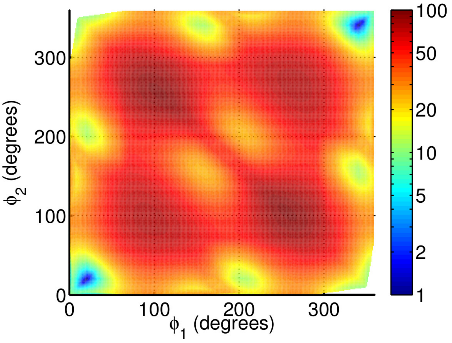

(c) modified force field

Figure 4.11: The potential energy surface as a function of the two dihedral angles that determine the twisting of the PIC molecule around its central bond, calculated using (a) the quantum chemical DFT method, (b) the CHARMM Drude force field, and (c) the CHARMM Drude force field with extra energy terms, given in Eq. 1 of the main text, which were fitted to reproduce the quantum chemical results. Energy scale in kJ mol^{-1}, with the lowest energy value of each plot set to 1 kJ mol^{-1}.

Chapter 5

Exciton transport in linear molecular aggregates with static and dynamic disorder

We have studied the behavior of the Pauli Master Equation Approach (PMEA) and Numerical Integration of the Schrödinger Equation (NISE) for exciton transport. We focused mainly on long-time transport, using a linear chain of chromophores as model system. At long times, the NISE method was found to always predict diffusive behavior. We investigated the dependence of the corresponding diffusion constant on several model parameters, and found that diffusion is fastest when the amounts of static and dynamic disorder are of the same order of magnitude. On the other hand, the PMEA was found to predict slightly subdiffusive motion for a set of parameters that is realistic for a class of molecular dye aggregates. Surprisingly, it was not possible to find a regime in parameter space where NISE and PMEA predicted the same long-time diffusion constant; for the studied parameter range, the PMEA predicted slower diffusion than NISE. Increasing the amount of static disorder in the PMEA led to strongly subdiffusive transport at long times, regardless of temperature, probably due to large energetic differences between neighboring chromophores acting as barriers.

5.1 Introduction

The transport of electronic excitation energy (excitons) in matter is an essential process for all life on earth, since plants and photosynthetic bacteria depend on this phenomenon to move excitons from the location where they are created by the absorption of sunlight to the photosynthetic reaction center, where the electronic excitation energy is converted into chemical energy [13–15]. Exciton transport also plays an important role in many synthetic functional materials, such as artificial light harvesting systems [153], molecular aggregates [1, 2], semiconductor quantum wells and wires [154], and polymers [155, 156]. In addition, accurate simulation of exciton dynamics is necessary for interpreting experimental nonlinear spectra that are in broad use as probes for all sorts of materials.

The main challenge in modeling Frenkel exciton transport lies in accurately describing the interaction of the exciton with its complex environment [64, 143, 157]. Over the past decades a myriad of models have been developed to address this challenge, examples being Redfield theory [158], cumulant expansions [112], Hierarchy of Equations of Motion (HEOM) [159, 160], surface hopping [144], and Ehrenfest dynamics [116, 161]. These methods differ in their underlying assumptions and thus have different regimes of applicability.

In this chapter, we investigated two methods for modeling exciton dynamics: the Numerical Integration of the Schrödinger Equation (NISE) method [141, 143, 162–164] and the Pauli Master Equation Approach (PMEA) [3, 64, 157]. Both have seen extensive use, driven by their computational efficiency which allows treatment of large systems of many 1000's of chromophores. The NISE method describes the Frenkel exciton under consideration by its wavefunction, its most limiting assumption being that the environment is not influenced by the dynamics of the exciton. On the other hand, the PMEA propagates eigenstate populations using a rate equation, which assumes a small coupling between system and environment. It has previously been used to study exciton transport in one-dimensional chains in the low-temperature regime [165–167]. Here, we investigated the exciton dynamics predicted by both methods using numerical simulations. The system we used is a linear chain of chromophores. From now on we will assume this chain to be a molecular aggregate, but much of what we will find can easily be translated to other types of systems.

The outline of this chapter is as follows. In Section 5.2, we describe our Frenkel exciton Hamiltonian, and explain how we performed simulations of exciton transport using the NISE and PMEA methods. In addition, we define the possible transport regimes that we have encountered in our simulations.

Section 5.3 contains the results of our simulations of exciton dynamics, and explains how the transport predicted by the NISE and PMEA methods depends on the simulation parameters used. We conclude in Section 5.4.

5.2 Models and simulation details

5.2.1 Frenkel exciton Hamiltonian

In this chapter, we considered a linear molecular aggregate with open boundary conditions. The number of chromophores N ranged from 100's to 1000's in our simulations, and was chosen such that finite-size effects were negligible. We described the electronic state of this molecular aggregate using a Frenkel exciton Hamiltonian. We took into account two energy levels per chromophore, namely the electronic ground state and a single excited state. The Hamiltonian of the collective excited states (Frenkel excitons) in the aggregate was then given by

$$H = \sum_{n=1}^{N} E_n b_n^\dagger b_n + \sum_{n=1}^{N-1} J(b_n^\dagger b_{n+1} + b_{n+1}^\dagger b_n) \tag{5.1}$$

where the Pauli operators b_n and $b_n^\dagger$, respectively, annihilate or create an exciton at site n, and the excitation transfer interaction J is taken into account only between nearest neighbors. The site transition energies E_n contain the effects of the environment and consist of a static and a dynamic component, $E_n = E_n^{stat} + E_n^{dyn}$. The static component E_n^{stat} is due to static inhomogeneity of the host matrix and also includes the average excitation energy of the chromophores. We modeled E_n^{stat} as Gaussian random variables with standard deviation σ_{stat}; the disorder deviation from the average exictation energy was assumed uncorrelated for different molecules. The dynamic part of the site transition energies, E_n^{dyn}, accounts for the dynamic degrees of freedom of the environment (i.e., vibrations). In principle, E_n^{dyn} should account for the quantum nature of the environmental degrees of freedom and is an operator in the Hilbert space of these degrees of freedom [157]. As a simplification, often an effective treatment is used, where the effect of a dynamic environment is described through a classical, stochastic model [168], in which E_n^{dyn} is treated as a stochastic process. The E_n^{dyn} are then explicitly time-dependent, making the Hamiltonian explicitly time-dependent as well. This latter approach is taken by the NISE method, which models E_n^{dyn} as a Gaussian random process with standard deviation σ_{dyn} and a particular decay of the autocorrelation function in time (see Eqs. 5.2 and 5.3 below). Solving the time-dependent Schrödinger equation for the resulting Hamiltonian then leads to scattering between the (time-dependent) eigenstates. The NISE method has the advantage that it is not perturbative, but on the other hand the detailed balance condition is not obeyed because of a lack of feedback from the quantum system on the classical degrees of freedom. In the PMEA, second-order perturbation theory is applied to the dynamic part of the site transition energies E_n^{dyn}, yielding a set of transition rates between the (static) eigenstates of Hamiltonian 5.1 (see Section 5.2.3) which guarantee detailed balance. The transition rates can be derived either by describing E_n^{dyn} as a quantum-mechanical operator, with a linear coupling of the exciton to environmental vibrations [157], or by modeling E_n^{dyn} as a classical, Gaussian stochastic process [169, 170].

When using the NISE method, the stochastic process $E_n^{dyn}(t)$ is Gaussian, and thus characterized entirely by the combination of its mean and autocorrelation function. Without loss of generality, the mean of the dynamic disorder may be chosen zero, whence its correlation function is defined by the expectation value

$$C(t) = \langle E_n^{dyn}(t')E_n^{dyn}(t'-t)\rangle. \tag{5.2}$$

We will assume that no correlations exist between different molecules. Three functional forms for the correlation function have been used in this chapter, which are shown in Figure 5.1. In almost all cases, we have used what we will call the 'overshooting' correlation function,

$$C(t) = \sigma_{dyn}^2 \tau_c^2 \frac{\tau_c^2 - t^2}{(\tau_c^2 + t^2)^2}. \tag{5.3}$$

where the parameter τ_c can be interpreted as a memory time. Note that the convential definition of the correlation time [171]

$$\tau_c = \int_0^\infty \mathrm{d}t \, \frac{C(t)}{\sigma_{dyn}^2} \tag{5.4}$$

cannot be used for the overshooting function, as it assumes a strictly positive correlation function and would give $\tau_c = 0$ in this case. Instead, we define the memory time of the overshooting correlation function as the point in time where the function intersects the time axis, $C(\tau_c) = 0$.

The two other autocorrelation functions have been used to compare the results of the NISE method with other ways of simulating exciton dynamics. One of these is the Ohmic correlation function, which we derived from the Ohmic spectral density in Appendix 5.5,

$$C(t) = \sigma_{dyn}^2 \frac{1}{\frac{\pi^2}{4}\left(\frac{t}{\tau_c}\right)^2 + 1}. \tag{5.5}$$

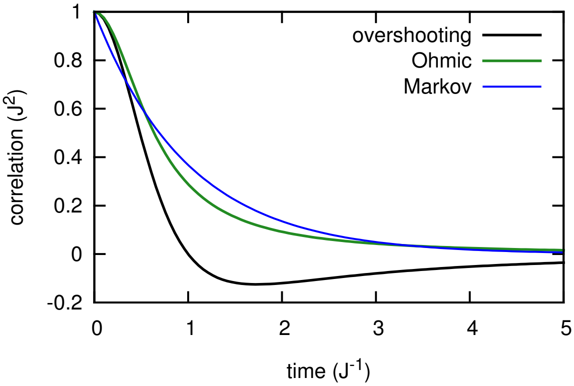

Figure 5.1: The overshooting, Ohmic, and Markov correlation functions, for a correlation time of $\tau_c = 1\,\mathrm{J}^{-1}$ and disorder size of $\sigma_{dyn} = 1\,\mathrm{J}$.

The other is the Markov correlation function, given by

$$C(t) = \sigma_{dyn}^2 \exp(-t/\tau_c). \tag{5.6}$$

5.2.2 Modeling exciton dynamics with the NISE method

As explained in Section 5.2.1, the Numerical Integration of the Schrödinger Equation method describes the excitonic state of a molecular aggregate using the wavefunction, and accounts for fluctuations of the environment by adding a time-dependent, stochastic component to the electronic Hamiltonian. The method can be implemented in a number of ways [172], of which the exact exponential approach, which propagates the wavefunction by successive application of the time-evolution operator, is the most straightforward; this is the approach used here. Specifically, the excitonic wavefunction $\Psi(t)$ was propagated over each time step Δt as

$$\Psi(t + \Delta t) = \exp\left(-\frac{i}{\hbar} H(t)\Delta t\right) \Psi(t), \tag{5.7}$$

where the exciton Hamiltonian is given by Eq. (5.1). Simulations were initialized with the exciton located on the central chromophore of the chain.

The NISE method takes the influence of the environment on the exciton into account, but neglects the back-reaction of the exciton on the environment. One of the cases for which this is accurate is when the coupling between system and environment is small. An important effect of this simplification is that in equilibrium, all eigenstates have the same probability of being occupied. Since the relative probability of an eigenstate being occupied is given by the Boltzmann factor $\exp(-E/k_BT)$, this can be interpreted as the NISE method operating at infinite temperature. Assuming an infinite temperature is appropriate when the width of the exciton band is smaller than k_BT, as the Boltzmann factors of all eigenstates are then approximately equal. For a linear aggregate with nearest-neighbor interactions, the width of the exciton band is $4J$, and at room temperature, $k_BT \approx 200\,\mathrm{cm}^{-1}$. The high-temperature assumption thus results in the validity condition $J \ll 50\,\mathrm{cm}^{-1}$. Even though this condition is normally not met for singlet excitons in molecular aggregates, this might not always pose a problem, since equilibrium may not be reached within the experimental time scale. In particular, when the intermolecular coupling strength J is large compared to the dynamic disorder, the movement of an exciton to neighboring sites will be much faster than scattering to higher lying states, and the NISE method might well yield accurate results. Note that in contrast to electronic excitations, collective vibrations have a much narrower band and therefore the high-temperature assumption made by the NISE method should be more accurate for these vibrational excitations [141, 163, 164].

5.2.3 Modeling exciton dynamics with the PMEA

In the Pauli Master Equation Approach, second-order perturbation theory in the coupling between the system (exciton) and its environment (nuclear vibrations) is used to obtain a rate equation for the populations of excitonic states. We derived in Appendix 5.6 that the assumptions made by using perturbation theory are approximately accurate when $\sigma_{dyn} \ll \sigma_{stat}$ (note that the connection between σ_{dyn} on the one hand, and the parameters T and W_0 of the PMEA on the other, is made in Appendix 5.5).

The perturbative treatment of the exciton-vibration coupling leads to a scattering rate from excitonic state $|k'\rangle$ with energy $E_{k'}$ to state $|k\rangle$ with energy E_k that is given by [63, 157, 173, 174]

$$\begin{aligned} W_{kk'} =& J(|E_{k'} - E_k|) \sum_n |a_{kn}|^2 |a_{k'n}|^2 \\ & [\theta(E_k - E_{k'}) n(E_k - E_{k'}) + \theta(E_{k'} - E_k)(1 + n(E_{k'} - E_k))] , \end{aligned} \tag{5.8}$$

where $\theta(E)$ denotes the Heaviside step function and $n(E) = (\exp(E/kT) - 1)^{-1}$ is the Bose-Einstein distribution. We used the Ohmic functional form for the spectral density,

$$J(E) = W_0 \theta(E) E \exp(-E/E_c), \tag{5.9}$$

where the prefactor W_0 is a measure of exciton scattering and the exponential cutoff with cutoff energy E_c makes sure that the spectral density vanishes at large energies. The eigenstate $|k\rangle$ and the state $|n\rangle$ (in which the excitation is localized entirely on site n) have an overlap factor of $a_{kn} = \langle k|n\rangle$. Using the scattering rates given in Eq. 5.8, we calculated the time evolution of eigenstate populations as

$$P_k(t) = \sum_{k'} \exp(-\hat{R}t)_{kk'} P_{k'}(0), \tag{5.10}$$

where

$$R_{kk'} = \sum_{k''} W_{k''k}\delta_{kk'} - W_{kk'}. \tag{5.11}$$

Simulations were initiated with the exciton fully located in a single eigenstate, the probability of starting in eigenstate k being equal to its squared overlap factor a^2_{km} on the central chromophore m of the chain.

5.2.4 The limiting regimes of ballistic and diffusive exciton transport

The nature of the exciton motion in a molecular aggregate is determined by the degree of spatial and temporal coherence of the exciton states. In the limit of fully coherent eigenstates (i.e., in the absence of static and dynamic disorder), the exciton motion is similar to that of a particle moving at a constant speed that is proportional to the exciton bandwith, and is called ballistic. On the other hand, in the incoherent limit, exciton motion is diffusive. The different types of transport can be characterized using the second moment of exciton displacement $\langle (n - n_0)^2 \rangle$, where n_0 denotes the initial exciton location on a linear chain and the brackets denote both a quantum mechanical average (expectation value) as well as a statistical one (averaging over many realizations of the disorder in site energies).

For ballistic transport on a linear chain with nearest-neighbor interactions (see Eq. 5.18), the second moment of exciton displacement evolves as

$$\langle (n - n_0)^2 \rangle = 2J^2t^2. \tag{5.12}$$

On the other hand, for diffusive transport

$$\langle (n - n_0)^2 \rangle = 2Dt, \tag{5.13}$$

where D is called the diffusion constant. A third case is anomalous diffusion, for which the second moment does not increase linearly with time,

$$\langle (n - n_0)^2 \rangle = ct^{\alpha}. \tag{5.14}$$

This type of motion is termed subdiffusive when $\alpha < 1$, and superdiffusive for $\alpha > 1$.

The numerical calculation of the second moment of displacement differs between the NISE and PMEA methods. For the NISE method, the calculation is straightforward and exact,

$$\langle (n-n_0)^2 \rangle = \frac{1}{R} \sum_r \sum_n P_{rn}(t)(n-n_0)^2. \tag{5.15}$$

Here the index r runs over all R realizations of the disorder in site transition energies, and the population at site n for realization r is given by $P_{rn} = |\langle n|\Psi_r(t)\rangle|^2$. When using the PMEA method, however, the site populations P_n cannot be calculated because only the eigenstate populations P_k are known, while the wavefunction is unknown. Therefore, we instead applied an approximate calculation which assumes that all interexcitonic coherences have disappeared,

$$\langle (n-n_0)^2 \rangle \approx \frac{1}{R} \sum_r \sum_k P_{rk} \langle (n-n_0)^2 \rangle_{rk}, \tag{5.16}$$

where the second moment of displacement of eigenstate k is given by

$$\langle (n-n_0)^2 \rangle_{rk} = \sum_n (n-n_0)^2 |a^r_{kn}|^2. \tag{5.17}$$

Eq 5.16 is exact in the limit of fully localized eigenstates and an excellent approximation for times larger than the inter-exciton coherence time, and reduces to Eq. 5.15 in those cases.

5.3 Results and discussion

5.3.1 NISE model of exciton transport: general properties

The nature of exciton dynamics predicted by the NISE method depends on the interplay between the excitonic coupling, the static disorder, and the dynamic disorder. Without energetic disorder, transport is ballistic and the exciton moves away from its source with a constant velocity, as shown in Figure 5.2a. In this case an analytic solution exists for the exciton probability density after a time t at a chromophore located n sites away from the starting position [175],

$$P_n(t) = [J_n(2Jt)]^2, \tag{5.18}$$

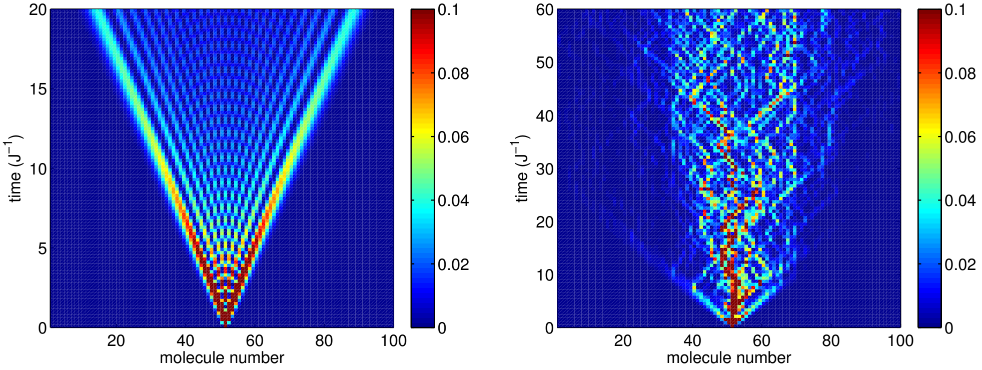

(a) no disorder

(b) single disorder realization

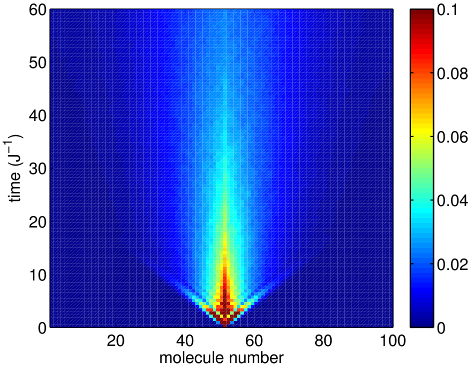

(c) 1000 disorder realizations

Figure 5.2: Exciton motion in a linear chain of 100 chromophores, with the exciton initially located on the central chromophore, modeled using the NISE method. Color coding represents the exciton probability density. (a) No static or dynamic disorder. (b, c) $\sigma_{dyn} = \sigma_{stat} = 0.5\,\mathrm{J}$, $\tau_c = 3\,\mathrm{J}^{-1}$ and an overshooting correlation function Eq. 5.3 was used.

where $J_n(2Jt)$ is the Bessel function of order n (this result was derived using nearest neighbor couplings and periodic boundary conditions with the chain length N tending to infinity). Because the exciton moves away from its starting position with constant velocity, the second moment of its displacement is a quadratic function of time, as shown in Figure 5.3.

When static and dynamic disorder are introduced, exciton motion is hindered by scattering off the barriers posed by energetic differences between

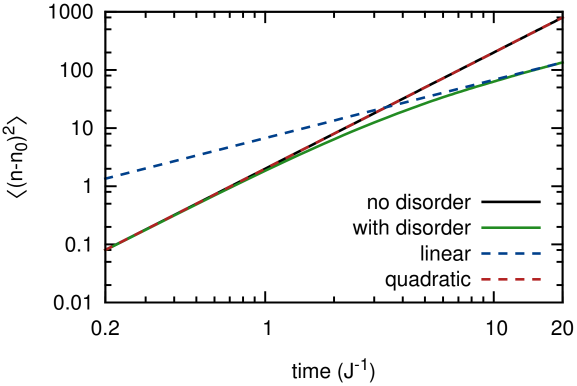

Figure 5.3: Exciton motion quantified by a log-log plot of the second moment of exciton displacement, as calculated with the NISE method. A linear function (blue dashes) and a quadratic function (red dashes) are shown for comparison. In the calculation including disorder, an overshooting correlation function Eq. 5.3 was used, $\sigma_{stat} = \sigma_{dyn} = 0.5\,\mathrm{J}$ and $\tau_c = 3\,\mathrm{J}^{-1}$.

nearest neighbors. The resulting motion is shown in Figure 5.2b for a single disorder realization, and in Figure 5.2c averaged over 1000 realizations of disorder (note that the observed exciton motion would be qualitatively unchanged had we used only dynamic disorder). We observe that initially the exciton motion is ballistic. As more and more scattering off energy barriers occurs, however, the exciton motion becomes slower, and the transport is to become diffusive in the long run. The resulting evolution of the second moment of displacement from a quadratic function to a linear function is depicted in Figure 5.3. An intermediate regime of subdiffusive motion is observed when (static and/or dynamic) disorder is large and the memory time of the dynamic disorder is long (see Figure 5.4). The reason is that initially only the eigenstates which are (partially) located on the starting site are excited; mixing of eigenstates by variations in the dynamic disorder is needed to move the exciton beyond the range of these initially excited states.

5.3.2 NISE model of exciton transport: scaling of the diffusion constant

As we have seen in the previous section, energetic disorder will in the long run cause exciton motion to become diffusive. The speed of this diffusive motion can be quantified using the diffusion constant (see section 5.2.4). Here, we in-

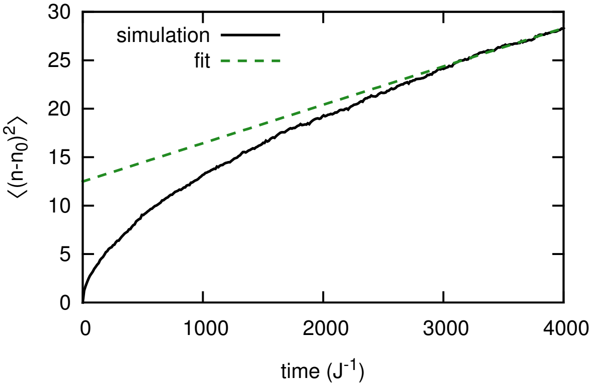

Figure 5.4: NISE result for the second moment of exciton displacement which shows an initial phase of subdiffusive transport, fitted with a linear function. Only data after $t = 3000\,\mathrm{J}^{-1}$ was used for the fit. The simulation used an overshooting correlation function Eq. 5.3 in combination with parameters $\sigma_{stat} = 5$, $\sigma_{dyn} = 1\,\mathrm{J}$ and $\tau_c = 20\,\mathrm{J}^{-1}$.

vestigate the dependence of the diffusion constant on three model parameters: the memory time of transition energies τ_c, the size of dynamic disorder σ_{dyn}, and the size of static disorder σ_{stat}.

Figure 5.5 shows the scaling of the diffusion constant with the inverse memory time of the dynamic disorder, in the absence of static disorder. A general pattern can be observed that does not depend on the size of the dynamic disorder. In the limit of a large memory time $\tau_c \to \infty$, the dynamic disorder becomes static and the diffusion constant drops sharply, $D \to 0$. For intermediate values of the memory time, the diffusion constant changes relatively slowly as a function of this time. Then, when decreasing the memory time further, the diffusion constant increases sharply. We cannot handle the white noise limit $\tau_c \to 0$ analytically because the overshooting correlation function is not strictly positive, which makes it impossible to define a memory time in the conventional manner, using Eq. 5.4. As can be seen in Figure 5.5, the diffusion constant was about two orders of magnitude higher for the small disorder value of $\sigma_{dyn} = 0.1\,\mathrm{J}$ compared to the larger value of $\sigma_{dyn} = 1\,\mathrm{J}$. Another difference between the studied disorder levels was that for the smaller disorder value, the diffusion constant dropped much sharper in the static limit (the drop is so sharp that it is hard to distinguish in the figure). This might be due to a much larger delocalization of exciton states, and thus a larger overlap between states, which could make even small changes in the site transition energies give rise to strong mixing between (instantaneous) eigenstates.

The dependence of the diffusion constant on the size of the dynamic disorder σ_{dyn} is displayed in Figure 5.6, in the absence of static disorder and for an autocorrelation function $C(t)$ according to Eq. 5.3, with $\tau_c = 10\,\mathrm{J}^{-1}$. To show that the diffusion constant has a power-law dependence on σ_{dyn},

$$D = c\sigma_{dyn}^{\alpha}, \tag{5.19}$$

we used a logarithmic scale for both axes. We also show a power-law fit to the data in Figure 5.6; since the power-law behavior only holds for small values of σ_{dyn}, this fit is performed using data points for which $\sigma_{dyn} \leq 1$. The best fit was obtained for $c = 1.8$ and $\alpha = -2.0$. This power of -2 has previously been obtained analytically [176] by assuming that the dynamic disorder and the memory time are small, but our numerical calculations show that this analytic result is accurate well beyond the regime for which it was derived. The monotonic decrease of the diffusion constant for larger σ_{dyn} can be understood as increased scattering of the wavefunction off increasingly large energy barriers. Note that using the Path Integral method, which is very similar to NISE, Ezaki et al. have also found that the diffusion constant decreases monotonically with the size of dynamic disorder [177].

In Figure 5.7 we again show the dependence of the diffusion constant on the size of the dynamic disorder, but now we also took into account a static disorder component in our calculations. We can see that when $\sigma_{dyn} \ll \sigma_{stat}$, fluctuations in transition energies due to dynamic disorder were too small to overcome the static disorder, and D tended to zero. On the other hand, when $\sigma_{dyn} \gg \sigma_{stat}$, the large size of the dynamic disorder inhibited exciton transport, and the diffusion constant diminished with increasing σ_{dyn}, consistent with Figure 5.6. The diffusion speed was at its maximum in the intermediate regime where σ_{dyn} is of the same order of magnitude as σ_{stat}; this result is a manifestation of the phenomenon of environment-assisted quantum transport [178, 179]. The relation between the diffusion constant and the size of static disorder is shown in Figure 5.8. As was the case for the dynamic disorder, we see that the diffusion constant decreases monotonically when the size of the static disorder σ_{stat} increases. Again, the explaination is the increased occurence of scattering events as energy barriers become larger.

Of the great number of methods for calculating exciton dynamics that have been developed, some give results that are very similar to the NISE method. We demonstrated this by comparing the dependence of the diffusion constant on the inverse memory time for several methods: the NISE method, the path integral method [177], the coherent potential approximation (CPA) [177], and

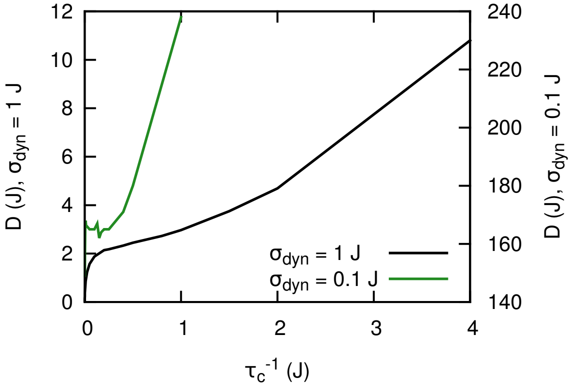

Figure 5.5: Dependence of the diffusion constant on the inverse memory time of site transition energies for the NISE method, plotted for two values of dynamic disorder and an overshooting correlation function Eq. 5.3 (no static disorder component was taken into account).

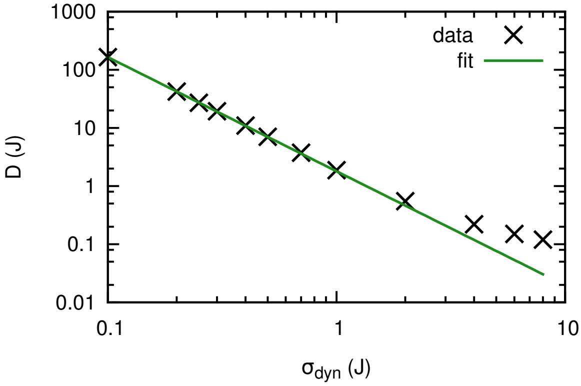

Figure 5.6: Dependence of the diffusion constant on the standard deviation of the dynamic disorder in the site transition energies, using the NISE method and fitted with a power law function (best fit with a power of -2). No static disorder was taken into account, and an overshooting correlation function Eq. 5.3 with a memory time of $\tau_c = 10\,\mathrm{J}^{-1}$ was used.

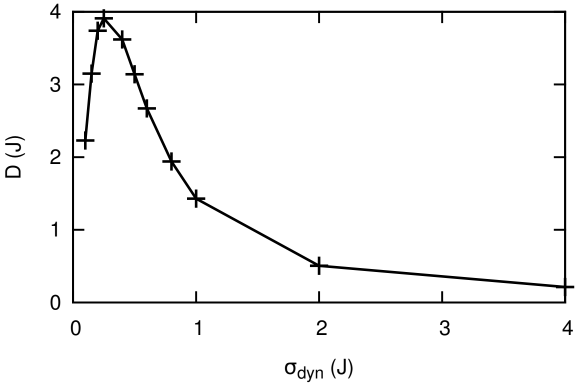

Figure 5.7: Dependence of the diffusion constant on the size of dynamic disorder for the NISE method. In contrast to Fig. 5.6, also a static disorder component with standard deviation $\sigma_{stat} = 0.5\,\mathrm{J}$ was taken into account. For the dynamic disorder, an overshooting correlation function Eq. 5.3 with a memory time of $\tau_c = 10\,\mathrm{J}^{-1}$ was used.

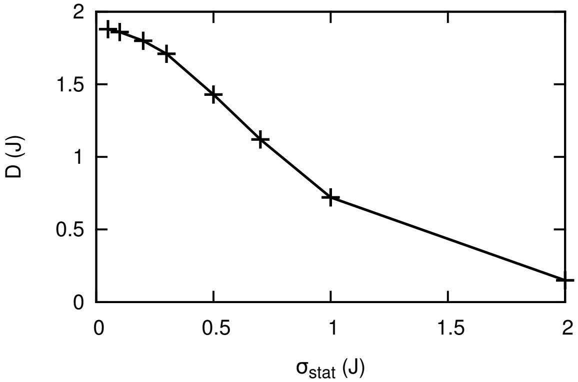

Figure 5.8: Dependence of the diffusion constant on the size of static disorder for the NISE method. An overshooting correlation function Eq. 5.3, a dynamic disorder size of $\sigma_{dyn} = 1\,\mathrm{J}$ and a memory time of $\tau_c = 10\,\mathrm{J}^{-1}$ were used.

a method developed by Kassner and Reineker [180] (see Figure 5.9). Here, we used the Markov correlation function Eq. 5.6, as this was also used in the methods we compared to. A good agreement is found between the different methods, except for the less accurate CPA which deviated substantially from

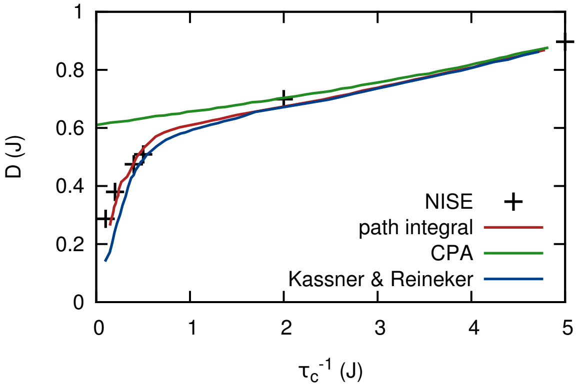

Figure 5.9: Dependence of the diffusion constant on the inverse memory time of the dynamic disorder, for several methods of calculating exciton dynamics: the NISE method used in this chapter, the path integral and CPA methods used by Ezaki et al. [177], and the method developed by Kassner & Reineker [180]. Data for the CPA, path integral, and Kassner & Reineker methods was taken from Ezaki et al. [177]. For all calculations, the disorder size was given by $\sigma_{dyn} = 3\,\text{J}$ and $\sigma_{stat} = 0$, and a Markov correlation function Eq. 5.6 was used.

the others for large memory times. The reason for this agreement was that all four methods make the same basic approximation of neglecting the back-reaction of the system on the bath.

5.3.3 The PMEA model of exciton transport

We now turn to the exciton motion that is predicted by the Pauli Master Equation Approach. Some general features of this exciton motion can be deduced directly from the formula for scattering rates between eigenstates, given by Eq. 5.8. We see that scattering rates are proportional to the parameter W_0, which is related to the influence of the fluctuating environment. The motion is predicted to be faster for higher W_0 (more interaction with environmental fluctuations), which is only realistic when W_0 is not too large (see Appendix 5.6). Transport will also be slower for small values of the cutoff energy E_c.

We have analyzed the behavior of the PMEA in a more quantitative manner by performing simulations for different values of the model parameters W_0, σ_{stat}, T and ω_c. The motion predicted for the set of parameters $\sigma_{stat} = 0.3\,\text{J}$, $W_0 = 10\,\text{J}$, and $\omega_c = 0.5\,\text{J}$ (which is realistic for a molecular aggregate [64])

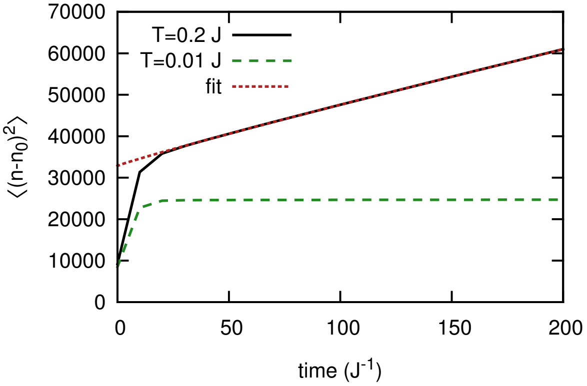

Figure 5.10: Exciton motion simulated with the PMEA, fitted by a power law Eq. 5.19. An Ohmic spectral density Eq. 5.9 was used, and parameters that are realistic for a molecular aggregate: $\sigma_{stat} = 0.3\,\mathrm{J}$, $W_0 = 10\,\mathrm{J}$, and $\omega_c = 0.5\,\mathrm{J}$. Note that for an excitonic coupling of $1000\,\mathrm{cm}^{-1}$, a temperature of 0.2 J equals 300 K, while 0.01 J would correspond to 15 K.

is shown in Figure 5.10. At room temperature, we could distinguish between two transport regimes: an initial phase of fast transport, followed by a phase of slower motion. To clarify the origins of the initial phase of fast transport, we have also plotted the exciton motion for a much lower temperature. Also here we observed the initial phase of fast exciton movement, which could only be caused by the exciton thermalizing from high-energy states to lower-lying states, since this is the only type of scattering that can occur at very low temperatures; this suggests that thermalization was responsible for the room temperature result as well. However, we must caution that the nature of this initial transport phase probably depends strongly on the chosen initial conditions. Once the initial thermalization was finished, a slower motion from low-energy state to low-energy state took over at room temperature, while the exciton was practically trapped in one of the lowest-energy states at the very low temperature.

To assess the nature of the long-time transport at room temperature, we performed a power law fit using only data for times larger than $30\,\mathrm{J}^{-1}$, with result

$$\langle (n-n_0)^2 \rangle = 32875 + 200 \cdot \left(\frac{t}{J^{-1}} \right)^{0.93} . \tag{5.20}$$

The observed exciton motion was thus almost diffusive in the long-time limit. Note that the fit values could vary somewhat depending on the time range

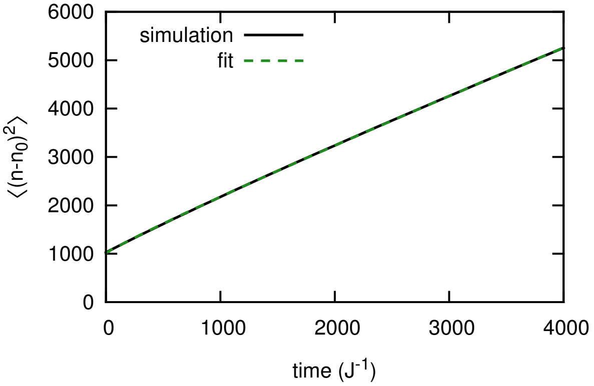

Figure 5.11: Exciton motion simulated with the PMEA, fitted by a power law. We used an Ohmic spectral density Eq. 5.9 and parameters $\sigma_{stat} = 0.5\,\mathrm{J}$, $\omega_c = 0.16\,\mathrm{J}$, $T = 100\,\mathrm{J}$, and $W_0 = 2 \cdot 10^{-4}\,\mathrm{J}$ (which corresponds to $\sigma_{dyn} = 0.5\,\mathrm{J}$). The fit cannot be distinguished from the simulation.

chosen for the fit, since the power-law behavior was not exactly obeyed. A relevant time scale in this respect is the fluorescence decay time of molecular aggregates, for which a typical value is 100 ps [34, 181]; assuming a coupling of $J = 1000\,\mathrm{cm}^{-1}$, this time span is equivalent to $3000\,\mathrm{J}^{-1}$.

To compare the PMEA and NISE methods, we tried to find a regime in parameter space for which both methods predict diffusive behavior at long times, with the same diffusion constant. To this end, we performed PMEA simulations using a very high temperature, since the NISE method operates in the high-temperature limit. In the high-temperature limit, the Ohmic spectral density used in our PMEA simulations can be transformed into an Ohmic autocorrelation function for the site transition energies, which we used for corresponding simulations with the NISE method (see Appendix 5.5). This transformation also yielded the necessary relation between the size of dynamic disorder σ_{dyn} in the NISE method on the one hand, and the temperature and scattering rates prefactor W_0 of the PMEA method on the other (see Eq. 5.31), as well as a relation between the autocorrelation time τ_c in the NISE method and the cutoff ω_c in the PMEA (Eq. 5.32). The result of a representative PMEA simulation is shown in Figure 5.11; in contrast to the simulations at lower temperatures, this simulation did not show an initial regime of quick transport, corroborating our earlier statement that such a transport regime

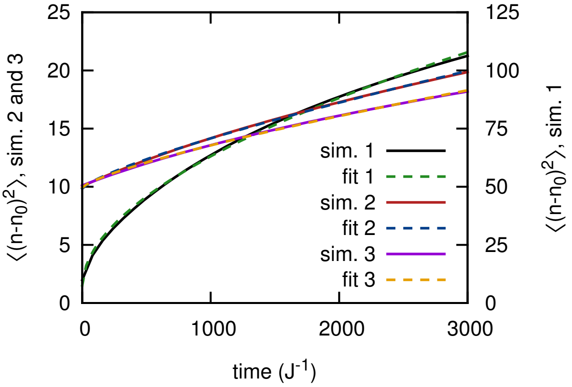

Figure 5.12: Examples of subdiffusive exciton motion predicted by the PMEA, each fitted by a power law function. For all simulations: $\sigma_{stat} = 2\,\mathrm{J}$, $\omega_c = 0.16\,\mathrm{J}$, and an Ohmic spectral density Eq. 5.9 was used. Simulation 1: $W_0 = 3.2\,\mathrm{J}$, $T = 0.1\,\mathrm{J}$. Simulation 2: $W_0 = 0.071\,\mathrm{J}$, $T = 0.1\,\mathrm{J}$. Simulation 3: $W_0 = 7.1 \cdot 10^{-5}\,\mathrm{J}$, $T = 100\,\mathrm{J}$ (corresponding to $\sigma_{dyn} = 0.3\,\mathrm{J}$).

was due to a thermalization effect. A power-law fit yielded

$$\langle (n - n_0)^2 \rangle = 1012 + 1.8 \cdot \left(\frac{t}{J^{-1}} \right)^{0.93} , \qquad (5.21)$$

indicating almost diffusive behavior with a deduced diffusion constant of $D = 0.9\,\mathrm{J}$. However, the NISE simulation with exactly the same parameters predicted diffusive motion that was about three times faster, with a diffusion constant of $D = 2.9\,\mathrm{J}$. Another representative parameter set that we tested is given by $\sigma_{stat} = 0.5\,\mathrm{J}$, $W_0 = 2 \cdot 10^{-6}\,\mathrm{J}$ (corresponding to $\sigma_{dyn} = 0.05\,\mathrm{J}$) and $\omega_c = 0.16\,\mathrm{J}$ (corresponding to $\tau_c = 10\,\mathrm{J}^{-1}$), for which the PMEA validity condition $\sigma_{dyn} \ll \sigma_{stat}$ derived in Appendix 5.6 holds much better, the difference in predicted diffusion speeds was even greater: the PMEA predicted $D = 6 \cdot 10^{-3}\,\mathrm{J}$, while the NISE method gave $D = 0.9\,\mathrm{J}$. Surprisingly, it seems that there does not exist a regime in parameter space for which the NISE and PMEA methods predict identical long-time transport behavior.

The PMEA simulations that we discussed until now predicted an only slightly subdiffusive exciton motion. However, for larger static disorder values than those used so far, much stronger subdiffusivity can arise, as shown in Figure 5.12. As we did before, the subdiffusivity of the predicted transport was quantified using power-law fits for the mean squares displacement. For simulation 1, performed at $T = 0.1\,\mathrm{J}$ (which equals 150 K for an excitonic coupling of $J = 1000\,\mathrm{cm}^{-1}$), the result of the fit was

$$\langle (n - n_0)^2 \rangle = 7.6 + 1.3 \cdot \left(\frac{t}{J^{-1}} \right)^{0.54} . \qquad (5.22)$$

The power of 0.54 shows that the exciton motion is strongly subdiffusive. Simulation 2 used identical parameters to simulation 1 except for a 45-fold decrease of the scattering rate prefactor W_0, giving

$$\langle (n - n_0)^2 \rangle = 9.8 + 0.022 \cdot \left(\frac{t}{J^{-1}} \right)^{0.77} . \qquad (5.23)$$

The smaller scattering rate thus resulted in less subdiffusivity (but note that this also depends on the time frame considered, which is held constant here). In simulation 3, the temperature was increased greatly while at the same time decreasing the prefactor W_0, so that the amount of exciton transport was almost the same as for simulation 2. The power-law fit gave

$$\langle (n - n_0)^2 \rangle = 9.9 + 0.019 \cdot \left(\frac{t}{J^{-1}} \right)^{0.76} , \qquad (5.24)$$

which shows that the amount of subdiffusivity is almost identical to simulation 2, even though the simulations use widely varying temperatures.

Inspiration for understanding the subdiffusive dynamics predicted by the PMEA might be gained from random walk and differential equation models for transport, for which a large body of literature exists that deals with the conditions that cause different types of transport [182–184]. For example, the simplest random walk model, with a single step time and length, predicts diffusive motion. However, when step times and lengths are taken from a probability distribution, diffusive motion will result for random walks with finite first and second moments of the step length and finite step times [184], while subdiffusive behavior is exhibited when the expectation value of the step time diverges [182]. Analogously, we might suspect that the subdiffusive motion predicted by the PMEA is the result of a diverging expectation value of the population transfer time (inverse scattering rate) between adjacent states. Work by Vlaming et al. indicates that this is indeed the case [167].

A mechanism by which large disorder could cause subdiffusivity is the existence of chromophores with a much lower transition energy than their neighbors, called outliers or traps. If the temperature is considerably lower than the width of the exciton band, excitons can easily enter such low-lying states but cannot leave them as the scattering rates out of these states are very low, which causes trapping of the exciton. Another mechanism which contributes to subdiffusivity is that outliers (low- as well as high-energy ones) act as barriers, which the exciton cannot pass. At high temperatures, this is probably the sole mechanism causing subdiffusive behavior.

5.4 Conclusion

In this chapter, we have studied the exciton transport predicted by the NISE and PMEA methods. At long times, we have observed that the NISE method always predicts diffusive behavior, no matter how large the energetic disorder. We have found that exciton transport is fastest for small static disorder, a dynamic disorder size which is of the same order of magnitude as the static disorder, and a short memory time of the dynamic disorder. This means that functional materials that require fast exciton transfer should be designed to have these properties. For the PMEA, our simulations showed that at long times, slightly subdiffusive motion is predicted for a set of parameters that is realistic for a molecular aggregate. Not only does this PMEA result differ qualitatively from the fully diffusive motion seen using the NISE method, but at long times the PMEA also gives slower transport than the NISE method for the parameter ranges we considered. Surprisingly, it was not possible to find a regime in parameter space where the predictions of the NISE and PMEA methods coincided. We speculate that at high temperatures the results of the NISE method are more accurate, since unlike the PMEA it is not a perturbative method, and that in reality long-time exciton motion is diffusive at high temperatures. On the other hand, the diffusion constant predicted by the NISE method did coincide with that of several other methods. When the size of the static disorder was increased in the PMEA, the exciton motion became strongly subdiffusive. Such strongly subdiffusive motion was found before for low temperatures and Lévy disorder (that carries more weight in the tails than the Gaussian disorder used here) by Vlaming et al. [167], but we show that also for medium to very high temperatures and Gaussian disorder, strong subdiffusivity can occur as well.

The different predictions made by the PMEA and NISE methods in particular, and the plethora of methods for calcuting exciton dynamics in general, means that for each application proper testing by comparison to experiment should be performed, to make sure the method chosen is used in its regime of validity.

5.5 Appendix: from the Ohmic spectral density to the Ohmic autocorrelation function

A spectral density describes the frequency-dependent coupling between excitonic states and the thermal vibrations of their environment. It contains the same information about a system of chromophores as the autocorrelation function of site transition energies. Here, we will perform the transformation from spectral density to autocorrelation function for the Ohmic spectral density. Along the way, we will need to assume that the high-temperature limit holds.

The Ohmic spectral density with an exponential cutoff is given by

$$J(\omega) = W_0 \theta(\omega) \hbar\omega \exp\left(-\frac{\omega}{\omega_c}\right). \tag{5.25}$$

From this spectral density, we can obtain the frequency-domain quantum correlation function [116],

$$C_q(\omega) = 2\pi\hbar(1 + n(\omega))(J(\omega) - J(-\omega)), \tag{5.26}$$

where the subscript q denotes a quantum correlation function and $n(\omega)$ is the Bose-Einstein distribution

$$n(\omega) = \frac{1}{e^{\hbar\omega/k_B T} - 1}. \tag{5.27}$$

By taking the high-temperature limit we simplify the frequency-domain quantum correlation function to

$$C_q(\omega) = 2\pi\hbar W_0 k_B T e^{-|\omega|/\omega_c}. \tag{5.28}$$

By applying the Fourier transform to the above quantity, we obtain the time-domain quantum correlation function

$$C_q(t) = 2\pi \int_{-\infty}^{\infty} \mathrm{d}\omega\, e^{i\omega t} C(\omega) = 4\pi^2 \hbar W_0 k_B T \frac{2}{\omega_c (t^2 + 1/\omega_c^2)}. \tag{5.29}$$

We now introduce the symmetric (with respect to complex conjugation) correlation function $C_q^{(+)}(t) = C_q(t) + C_q^*(t)$, which is real; the classical correlation function $C(t)$ can be identified with $C_q^{(+)}(t)/2$. Because $C_q(t)$ is real (due to $C_q(\omega)$ being even and real), $C(t) = C_q(t)$, so that

$$C(t) = 4\pi^2 \hbar W_0 k_B T \frac{2}{\omega_c (t^2 + 1/\omega_c^2)}. \tag{5.30}$$

This classical autocorrelation function of the site transition energies can be rewritten into a function of the standard deviation σ_{dyn} and correlation time τ_c of the energy fluctuations. To this end, we use that

$$\sigma_{dyn}^2 = C(0) = 8\pi^2\hbar W_0 k_B T \omega_c, \tag{5.31}$$

which also relates the dynamic disorder of the NISE method to the scattering rates of the PMEA (but only in the high-temperature limit), and we use that [171]

$$\tau_c = \int_0^\infty \mathrm{d}t \, \frac{C(t)}{\sigma_{dyn}^2} = \frac{\pi}{2\omega_c}. \tag{5.32}$$

The Ohmic autocorrelation function can then be expressed as

$$C(t) = \sigma_{dyn}^2 \frac{1}{\frac{\pi^2}{4}\left(\frac{t}{\tau_c}\right)^2 + 1}. \tag{5.33}$$

5.6 Appendix: regime of validity of the perturbation theory approximation used to derive the PMEA

The Pauli Master Equation 5.10 is derived using second order time-dependent perturbation theory in the interaction between the electronic excitation (the system) and the motion of the nuclei in its surrounding (the bath). Here, we derive the regime in parameter space for which this approximation is valid.

The derivation of the PMEA starts with the Hamiltonian $H = H_0 + H'$, where the interaction between system and bath

$$H' = \sum_{n=1}^{N} b_n^\dagger b_n E_n^{dyn}(t) \tag{5.34}$$

is treated as a perturbation, which influences the system dynamics through scattering rates between the eigenstates $|k\rangle$ of Hamiltonian H_0. The perturbation theory is considered to be valid when the mixing of the energy levels by the perturbation is negligible, in other words, the first order correction to the energy levels in time-independent perturbation theory must be considerably smaller than the spacing between energy levels. This gives the condition

$$\frac{H'_{kk}}{E_k - E_{k'}} \ll 1 \tag{5.35}$$

which must hold for all eigenstates k and k'. We rewrite

$$H'_{kk} = \langle k|H'|k\rangle = \sum_{n=1}^{N} E_n^{dyn}(t)|a_{kn}|^2, \tag{5.36}$$

with $a_{kn} = \langle k|n\rangle$. To simplify Eq. 5.36 further, we assume that the state $|k\rangle$ is delocalised over N_{del} chromophores, with an equal probability amplitude of $|a_{kn}|^2 = 1/N_{del}$ at each of these chromophores, and zero otherwise. Replacing the resulting expression

$$\sum_{n=1}^{N_{del}} E_n^{dyn}(t)/N_{del} \tag{5.37}$$

with its stochastic average then yields

$$H'_{kk} = \frac{\sigma_{dyn}}{\sqrt{N_{del}}}. \tag{5.38}$$

We can also simplify the expression for $E_k - E_{k'}$. Assuming a negative value of the excitonic coupling J (a J-aggregate), the typical spacing between two states $|k\rangle$ and $|k'\rangle$ at the bottom of the band (where most of the oscillator strength resides) is given by [185]

$$E_k - E_{k'} = 3\pi^2|J|/(N_{del}+1)^2, \tag{5.39}$$

which represents a lower bound for the spacing between states anywhere in the band. We also assume intermediate-size static disorder so that [186]

$$N_{del} + 1 \approx 9.6\left(\frac{\sigma_{stat}}{|J|}\right)^{-2/3}. \tag{5.40}$$

Combining the above yields

$$\frac{H'_{kk}}{E_k - E_{k'}} \approx \frac{\sigma_{dyn}}{\sqrt{N_{del}}}\frac{(N_{del}+1)^2}{3\pi^2|J|} \approx \frac{\sigma_{dyn}(N_{del}+1)^{3/2}}{3\pi^2|J|} \approx \frac{\sigma_{dyn}}{\sigma_{stat}}. \tag{5.41}$$

Substituting this result into Eq. (5.35) gives $\sigma_{dyn} \ll \sigma_{stat}$ as a validity criterion for the PMEA.

Samenvatting

In dit proefschrift worden moleculaire aggregaten die zijn opgebouwd uit synthetische kleurstofmoleculen onderzocht. Moleculaire aggregaten zijn clusters van moleculen die niet covalent gebonden zijn, maar die bijeen worden gehouden door bijvoorbeeld van der Waals krachten, $\pi - \pi$ interacties, hydrofobe interacties, waterstofbruggen of electrostatische krachten. Wanneer een aggregaat bestaat uit kleurstofmoleculen, dan verschilt de wisselwerking van het aggregaat met licht fundamenteel van de wisselwerking die losse kleurstofmoleculen met licht hebben. De reden hiervoor is een verandering in de aangeslagen toestanden van de kleurstofmoleculen wanneer ze elkaar naderen. Kleurstofmoleculen hebben meerdere aangeslagen toestanden, waarvan er meestal één optisch dominant is. Als de kleurstofmoleculen dicht op elkaar geplaatst zijn in een aggregaat koppelen deze optisch dominante toestanden, waardoor collectieve excitaties ontstaan die verspreid zijn over meerdere moleculen. De collectieve excitaties worden Frenkel excitonen genoemd en zijn de oorzaak van de speciale optische eigenschappen van moleculaire aggregaten. Deze speciale optische eigenschappen uitten zich onder andere in de verschillende absorptiespectra van aggregaten en monomeren: tijdens het aggregatieproces kan een roodverschuiving optreden van het spectrum (we spreken in dit geval van een J-aggregaat) of een blauwverschuiving (H-aggregaat). J-aggregaten worden gekenmerkt door een zeer smalle absorptieband en ultrasnelle spontane emissie van een foton door collectief stralend verval van de laagst-energetische excitontoestand. Verder kennen moleculaire aggregaten een sterke niet-lineaire optische respons en in sommige aggregaten kunnen excitonen over grote afstanden worden getransporteerd.

Aggregraten kunnen in het laboratorium worden gemaakt doordat sommige synthetische kleurstofmoleculen, wanneer ze worden opgelost in een vloeistof, spontaan samenkomen om een structuur te vormen. Deze structuren kunnen allerlei vormen aannemen, zoals een lineair aggregaat, een cilinder, een buis, of een vlak aggregaat. Ook het soort stapeling van de moleculen binnen het aggregaat toont grote variatie. De structuur van een aggregaat hangt zowel af van het gekozen kleurstofmolecuul als van experimentele omstandigheden zoals de concentratie van het kleurstofmolecuul, het type tegenion (wanneer het kleurstofmolecuul geladen is), de temperatuur en het type oplosmiddel. Het is dus in principe mogelijk om een aggregaat te ontwerpen door het kleurstofmolecuul en de experimentele omstandigheden aan te passen. In combinatie met hun speciale optische eigenschappen maakt dit moleculaire aggregaten veelbelovend voor toepassingen in de nanotechnologie, bijvoorbeeld als opto-elektronische onderdelen, als nanobuisjes die energie (excitonen) kunnen transporteren of als organische zonnecellen. Voor deze laatste toepassing kan inspiratie worden opgedaan in de natuur: sommige planten en bacteriën gebruiken aggregaten van kleurstofmoleculen, bijvoorbeeld van chlorofylmoleculen, om zonlicht te absorberen en om vervolgens het ontstane exciton te transporteren naar het fotosynthetisch reactiecentrum, waar de energie van het exciton wordt gebruikt om een brandstof te produceren. Eerder werden aggregaten van kleurstofmoleculen al toegepast in de traditionele fotografie, om de gevoeligheid voor licht te vergroten en kleurgevoeligheid te introduceren.

Er zijn verschillende manieren om met behulp van experimenten informatie over moleculaire aggregaten te verkrijgen. Elektronmicroscopie kan bijvoorbeeld gebruikt worden om afbeeldingen van aggregaten te maken. Deze techniek is echter nog niet verfijnd genoeg om ook de interne structuur van aggregaten te kunnen observeren, en ook kunnen alleen relatief grote aggregaten worden afgebeeld. De meest gebruikte experimentele techniek is echter het schijnen van laserlicht op een oplossing met aggregaten. Vervolgens wordt gemeten wat de wisselwerking tussen aggregaat en licht met het licht doet. De wisselwerking van het aggregaat met een enkele (eventueel gepolariseerde) lichtpuls geeft statische informatie over het aggregaat. Wanneer niet één maar meerdere lichtpulsen op het aggregaat worden gericht, met een kleine vertraging tussen iedere puls, kan ook dynamische informatie verkregen worden: de eerste lichtpuls slaat dan een exciton aan en de volgende lichtpulsen wisselwerken op latere tijdstippen met dit exciton.

Optische spectra kunnen een schat aan informatie bevatten, maar het is niet altijd eenvoudig om deze informatie te interpreteren. Het combineren van experimentele data met theoretische modellen is daarom noodzakelijk, waarbij traditioneel fenomenologische modellen worden gebruikt. Deze modellen postuleren een vorm en structuur van het aggregaat waarvan ingeschat wordt dat deze het gemeten spectrum kan verklaren. Modelparameters, die bijvoorbeeld de overgangsenergieën van de kleurstofmoleculen en de excitonische koppelingen tussen de moleculen beschrijven, worden vervolgens gefit aan experimentele data. Op deze manier wordt geprobeerd om het experimentele spectrum te reproduceren, en wanneer dit lukt is er een redelijke waarschijnlijkheid dat de gekozen aggregaatstructuur en de gefitte overgansenergieën en koppelingen realistisch waren. Deze fenomenologische aanpak heeft echter een aantal belangrijke nadelen: het kan bijvoorbeeld geen dynamische informatie leveren over de structuur van een aggregaat en ook niet de variatie tussen verschillende aggregaten in een monster modelleren. De grote vooruitgang in de rekenkracht van computers en in simulatiemethodes maakt dat tegenwoordig de alternatieve aanpak van ab initio simulaties mogelijk is, die deze nadelen niet heeft en in dit proefschrift gevolgd wordt. Onze aanpak begint met het uitvoeren van moleculaire dynamica simulaties om de vorm en structuur van een aggregaat te achterhalen. Vervolgens worden kwantumchemische berekeningen uitgevoerd op de verkregen structuren om overgansenergieën en excitonische koppelingen te verkrijgen, die op hun beurt weer als invoer dienen voor een model voor de excitontoestanden van het aggregaat. Uiteindelijk kan een absorptiespectrum worden uitgerekend en vergeleken met experiment.

Hoofdstuk 2 onderzoekt met deze ab initio aanpak aggregaten van het molecuul amphi-pseudoisocyanine (amphi-PIC), een amfifiele afgeleide van het veel bestudeerde PIC molecuul. Het amphi-PIC molecuul vormt het onderwerp van een aantal interessante experimenten over de mate van excitontransport in aggregaten, maar de resultaten van deze experimenten worden nog niet goed begrepen. Een van de oorzaken hiervoor is dat de vorm en interne structuur van de amphi-PIC aggregaten nog niet zijn opgehelderd, terwijl die van grote invloed zijn op het excitontransport. Om hier meer duidelijkheid over te krijgen hebben we moleculaire dynamica simulaties van het spontane aggregatieproces uitgevoerd. Deze simulaties leverden twee aggregaatvormen op, een cilindervorm en een lintvorm, maar we konden niet achterhalen welke van deze twee vormen het meest stabiel is in onze simulaties. De interne structuur van beide aggregaten was veel chaotischer dan we hadden verwacht. Verder wordt in dit hoofdstuk onderzocht in hoeverre moleculaire dynamica simulaties in staat zijn om de afhankelijkheid van het spontane aggregatieproces van het gebruikte tegenion te simuleren, en of deze simulaties het fenomeen van elkaar aantrekkende cylindrische aggregaten kunnen reproduceren zoals bijvoorbeeld is waargenomen voor cylindrische aggregaten van een ander kleurstofmolecuul.

Hoofdstuk 3 onderzoekt de optische eigenschappen van de aggregaten uit hoofdstuk 2. Het doel hiervan is tweeledig. Ten eerste willen we absorptie en lineair dichroisme spectra uitrekenen die met experiment kunnen worden vergeleken, om zo een indicatie te geven van de betrouwbaarheid van onze simulaties. Ten tweede geeft een ab initio simulatie van de optische eigenschappen van een aggregaat inzicht in de oorsprong van deze optische eigenschappen, door de relatie met meer fundamentele informatie als de aggregaatstructuur en de grootte van overgangsenergieën en koppelingen duidelijk te maken. Geen van de twee gesimuleerde spectra komt overeen met een door andere onderzoekers gemeten absorptiespectrum van amphi-PIC aggregaten; door de grote mate van structurele wanorde in de gesimuleerde aggregaten is hun absorptiespectrum veel te breed. Dit resultaat toont de moeilijkheid van het uitvoeren van betrouwbare simulaties van het spontane aggregatieproces. Wel bleek het mogelijk om de gesimuleerde absorptiespectra te begrijpen door ze te vergelijken met het spectrum van een eenvoudig lineair modelaggregaat met een isotrope verdeling van overgangsdipolen.

In Hoofdstuk 4 wordt het aggregatieproces van de kleurstof PIC, het best onderzochte synthetische kleurstofmolecuul, onderzocht. Het PIC molecuul heeft een essentiële rol gespeeld in het onderzoek naar moleculaire aggregaten: het fenomeen van kleurstofmoleculen in oplossing die spontaan aggregeren is namelijk toevalligerwijze ontdekt in de jaren 1930 door het onstaan van een smalle, roodverschoven piek in het absorptiespectrum van een PIC oplossing. Deze piek werk door G. Scheibe correct geïnterpreteerd als het resultaat van een polymerisatieproces. Na deze ontdekking is veel onderzoek naar de aggregatie van verschillende synthetische kleurstofmoleculen op gang gekomen. Uit spectroscopische experimenten weten we dat de aggregatie van PIC begint met de vorming van H-dimeren, met een absorptiepiek die blauwverschoven is ten opzichte van het monomeer. Wanneer het aggregatieproces voortschreidt groeit een smalle, roodverschoven piek, een teken van de vorming van een J-aggregaat. Uit gepolariseerde absorptiemetingen blijkt dat deze roodverschoven piek longitudinaal gepolariseerd is, wat erop duidt dat de as (lange zijde) van de PIC moleculen samenvalt met de as van het aggregaat. Het is niet bekend hoe de overgang van H-dimeer tot J-aggregaat verloopt, en ook niet wat de vorm of interne structuur van het aggregaat is. Daarom onderzoeken we dit spontane aggregatieproces door het in een moleculaire dynamica simulatie na te bootsen. In onze simulatie worden dimeren en grotere oligomeren gevormd, tot zo'n 20 moleculen groot, waarbij de moleculen als een stapel kaarten op elkaar liggen. Het absorptiespectrum van ons dimeer komt goed overeen met het experiment, waarmee we een eerder voorgesteld dimeermodel weerleggen, en ook het spectrum van het trimeer wordt berekend. Ook onderzoeken we de variatie in de tijd van de dimeerstructuur, en de invloed dat dit heeft op het absorptiespectrum. Omdat we in onze simulaties geen overgang zien van de gevormde oligomeren naar een groot J-aggregaat, proberen we de vorm van het J-aggregaat te achterhalen door de stabiliteit van verschillende modelstructuren in onze moleculaire dynamica simulaties te testen.

Hoofdstuk 5 bestudeert het excitontransport in een lineair moleculair aggregaat. Hiertoe gaan we na hoe dit transport afhangt van de relatieve grootte van enkele parameters die een vereenvoudigd modelaggregaat beschrijven. Deze parameters beschrijven ten eerste de verschillen tussen de overgangsenergieën van kleurstofmoleculen, die onder andere ontstaan door variatie in de positie van kleurstofmoleculen ten opzichte van naburige kleurstofmoleculen en watermoleculen. Bovendien verandert de overgangsenergie van kleurstofmoleculen met de tijd als gevolg van de bewegingen van de moleculen en hun omgeving. Als laatste is ook de excitonische koppeling tussen kleurstofmoleculen van belang. Om het excitontransport te kunnen voorspellen maken we gebruik van twee simulatiemethodes, de numerieke integratie van de Schrödinger vergelijking methode (Engelse afkorting: NISE) en de Pauli master vergelijking methode (PMEA). Met de NISE methode wordt het transport na verloop van tijd altijd diffusief en we bestuderen hoe de bijbehorende diffusieconstante schaalt met de eerder genoemde parameters van het aggregaat. Met de PMEA ligt dit ingewikkelder: het voorspelde transport is in dit geval subdiffusief, waarbij de mate van subdiffusiviteit afhangt van de parameters van het aggregaat en de bestudeerde tijdsspanne. We proberen om een set parameters te vinden waarbij de NISE en PMEA methodes in de lange-tijd limiet hetzelfde excitontransport voorspellen. Onze simulaties met de PMEA methode bij hoge temperaturen ontkrachten de theorie dat moleculen met lage overgangsenergieën als vallen voor excitonen fungeren en zo verantwoordelijk kunnen zijn voor subdiffusief gedrag, doordat we ook bij deze hoge temperaturen subdiffusief gedrag observeren en de kans dat een exciton in een lage-energie val raakt bij een hoge temperatuur even groot is als de kans dat hij eruit komt.

Dankwoord

Als eerste wil ik mijn promotor Jasper Knoester bedanken. Jasper, dit proefschrift was zonder jou niet mogelijk geweest. Regelmatig heb ik in onze gesprekken mogen delen in je grote kennis van de natuurkunde en in het bijzonder van moleculaire aggregaten. Je vermogen om de juiste vragen te stellen en je kritische blik hebben zowel dit onderzoek als mijn wetenschappelijke ontwikkeling regelmatig vooruit gebracht. I would also like to thank my co-promotor Anna Stradomska-Szymczak for her guidance and for our many enlightening discussions. You too were indispensible for the work presented in this thesis. Alex de Vries wil ik bedanken voor het begeleiden van mijn eerste stappen in de wereld van moleculaire dynamica simulaties. Ik denk met plezier terug aan onze samenwerking, die heeft geleid tot twee mooie wetenschappelijke artikels.

I am grateful to the members of the reading committee Bert Meijer, David Beljonne and Maria Loi for spending their valuable time on reading my thesis. Sjoerd en Emiel, fijn dat jullie me als paranimfen terzijde willen staan.

Verder wil ik mijn collega's bij de vakgroep Theorie van de Gecondenseerde Materie bedanken voor de goede sfeer, de gezellige lunches en de sociale activiteiten buiten het onderzoek om: Niels van der Vegte, Thomas la Cour Jansen, Roel Tempelaar, Chungwen Liang, Santanu Roy, Ana Cunha, Erik Bloemsma, Bas Vlaming, Robert Broos, Jasper Compaijen, Bintoro Nugroho, Victor Malyshev, Bernhard Hoenders, Wijnand Broer, Maxim Mostovoy, Sergey Artyukhin, Andrea Scaramucci, Andrey Leonov, Dennis Visser, Chiel van der Vegte, Kasper Duivenvoorden en Oleksandr Shvets. Thomas, je deur stond altijd open voor allerhande vragen en discussies, hartelijk dank daarvoor. Sergey, it was a pleasure being your roommate. Your enthousiasm for discussing any scientific problem was a true inspiration.

Tenslotte wil ik mijn familie en mijn vriendin Grunilda bedanken voor hun steun tijdens het schrijven van dit proefschrift.

Bibliography

[1] F. Würthner, T. E. Kaiser, and C. R. Saha-Möller, *Angew. Chem. Int. Ed.* **50**, 3376 (2011).

[2] T. Kobayashi, ed., *J-Aggregates* (World Scientific, Singapore, 2012).

[3] A. S. Davydov, *Theory of Molecular Excitons* (Plenum, New York, 1971).

[4] V. Agranovich, *Excitations in Organic Solids* (Oxford University Press, Oxford, 2009).

[5] C. E. K. Mees, *The Theory of the Photographic Process* (The MacMillan Company, New York, 1962).

[6] T. Tani, *Photographic Sensitivity* (Oxford University Press, Oxford, 1995).

[7] V. L. Bogdanov, E. N. Viktorova, S. V. Kulya, and A. S. Spiro, *JETP Lett.* **53**, 105 (1991).

[8] Y. Wang, *J. Opt. Soc. Am. B* **8**, 981 (1991).

[9] F. C. Spano and S. Mukamel, *Phys. Rev. Lett.* **66**, 1197 (1991).

[10] J. Knoester, *Chem. Phys. Lett.* **203**, 371 (1993).

[11] J. A. Klugkist, V. A. Malyshev, and J. Knoester, *J. Chem. Phys.* **127**, 164705 (2007).

[12] S. Mukhopadhyay, C. Risko, S. R. Marder, and J.-L. Brédas, *Chem. Sci.* **3**, 3103 (2012).

[13] H. van Amerongen, L. Valkunas, and R. van Grondelle, *Photosynthetic Excitons* (World Scientific, Singapore, 2000).

[14] T. Ritz, A. Damjanović, and K. Schulten, *ChemPhysChem* **3**, 243 (2002).

[15] S. Ganapathy, G. T. Oostergetel, P. K. Wawrzyniak, M. Reus, A. Gomez Maqueo Chew, F. Buda, E. J. Boekema, D. A. Bryant, A. R. Holzwarth, and H. J. M. de Groot, *Proc. Natl. Acad. Sci. U.S.A.* **106**, 8525 (2009).

[16] S. Kirstein and S. Daehne, *Int. J. Photoenergy* **2006**, 1 (2006).

[17] J. Knoester and S. Daehne, *Int. J. Photoenergy* **2006**, 1 (2006).

[18] D. G. Lidzey, D. D. C. Bradley, M. S. Skolnick, T. Virgili, S. Walker, and D. M. Whittaker, *Nature* **395**, 53 (1998).

[19] M. S. Bradley and V. Bulović, *Phys. Rev. B* **82**, 033305 (2010).

[20] Y. H. Kim, D. H. Jeong, D. Kim, S. C. Jeoung, H. S. Cho, S. K. Kim, N. Aratani, and A. Osuka, *J. Am. Chem. Soc.* **123**, 76 (2001).

[21] J. Hernando, P. A. J. de Witte, E. M. H. van Dijk, J. Korterik, R. J. M. Nolte, A. E. Rowan, M. F. García-Parajó, and N. F. van Hulst, *Angew. Chem. Int. Ed.* **43**, 4045 (2004).

[22] H. von Berlepsch, C. Böttcher, and L. Dähne, *J. Phys. Chem. B* **104**, 8792 (2000).

[23] M. C. Zwier, J. M. Shorb, and B. P. Krueger, *J. Comput. Chem.* **28**, 1572 (2007).

[24] C. Olbrich and U. Kleinekathöfer, *J. Phys. Chem. B* **114**, 12427 (2010).

[25] G. Scheibe, *Angew. Chem.* **49**, 563 (1936).

[26] G. Scheibe, *Angew. Chem.* **50**, 212 (1937).

[27] E. E. Jelley, *Nature* **138**, 1009 (1936).

[28] E. E. Jelley, *Nature* **139**, 631 (1937).

[29] J. Franck and E. Teller, *J. Chem. Phys.* **6**, 861 (1938).

[30] T. Kobayashi, ed., *J-Aggregates* (World Scientific, Singapore, 1996).

[31] E. W. Knapp, *Chem. Phys.* **85**, 73 (1984).

[32] M. Kasha. In: *Spectroscopy of the Excited State.* Ed. by B. di Bartolo. Vol. B12. New York: Plenum, 1976.

[33] S. de Boer, K. J. Vink, and D. A. Wiersma, *Chem. Phys. Lett.* **137**, 99 (1987).

[34] S. de Boer and D. A. Wiersma, *Chem. Phys. Lett.* **165**, 45 (1990).

[35] V. L. Bogdanov, E. N. Viktorova, S. V. Kulya, and A. S. Spiro, *Pis'ma Zh. Eksp. Teor. Fiz.* **53**, 100 (1990).

[36] V. Sundström, T. Gillbro, R. A. Gadonas, and A. Piskarskas, *J. Chem. Phys.* **89**, 2754 (1988).

[37] I. G. Scheblykin, O. Y. Sliusarenko, L. S. Lepnev, A. G. Vitukhnovsky, and M. van der Auweraer, *J. Phys. Chem. B* **104**, 10949 (2000).

[38] C. Spitz, J. Knoester, A. Ouart, and S. Daehne, *Chem. Phys.* **275**, 271 (2002).

[39] H. Kano and T. Kobayashi, *J. Chem. Phys.* **116**, 184 (2002).

[40] Z. Chen, V. Stepanenko, V. Dehm, P. Prins, L. Siebbeles, J. Seibt, P. Marquetand, V. Engel, and F. Würthner, *Chem. Eur. J.* **13**, 436 (2007).

[41] F. Mizutani, S. Iijima, and K. Tsuda, *Bull. Chem. Soc. Jpn.* **55**, 1295 (1982).

[42] G. McDermott, S. M. Prince, A. A. Freer, A. M. Hawthornthwaite-Lawless, M. Z. Papiz, R. J. Cogdell, and N. W. Isaacs, *Nature* **374**, 517 (1995).

[43] J. Koepke, X. Hu, C. Muenke, K. Schulten, and H. Michel, *Structure* **4**, 581 (1996).

[44] P. Jordan, P. Fromme, H. T. Witt, O. Klukas, W. Saenger, and N. Krauß, *Nature* **411**, 909 (2001).

[45] A. Zouni, H. T. Witt, J. Kern, P. Fromme, N. Krauß, W. Saenger, and P. Orth, *Nature* **409**, 739 (2001).

[46] D. E. Tronrud, J. Wen, L. Gay, and R. E. Blankenship, *Photosynth. Res.* **100**, 79 (2009).

[47] J. Pšenčík et al., *J. Bacteriol.* **191**, 6701 (2009).

[48] T. Brixner, J. Stenger, H. M. Vaswani, M. Cho, R. E. Blankenship, and G. R. Fleming, *Nature* **434**, 625 (2005).

[49] G. S. Engel, T. R. Calhoun, E. L. Read, T.-K. Ahn, T. Mančal, Y.-C. Cheng, R. E. Blankenship, and G. R. Fleming, *Nature* **446**, 782 (2007).

[50] J. Kim, S. Mukamel, and G. D. Scholes, *Acc. Chem. Res* **42**, 1375 (2009).

[51] E. Collini, C. Y. Wong, K. E. Wilk, P. M. G. Curmi, P. Brumer, and G. D. Scholes, *Nature* **463**, 644 (2010).

[52] F. Milota, J. Sperling, A. Nemeth, D. Abramavicius, S. Mukamel, and H. F. Kauffmann, *J. Chem. Phys.* **131**, 054510 (2009).

[53] Z. Wang, C. J. Medforth, and J. A. Shelnutt, *J. Am. Chem. Soc.* **126**, 15954 (2004).

[54] C. Didraga, A. Pugžlys, P. R. Hania, H. von Berlepsch, K. Duppen, and J. Knoester, *J. Phys. Chem. B* **108**, 14976 (2004).

[55] E. Lang, A. Sorokin, M. Drechsler, Y. V. Malyukin, and J. Köhler, *Nano Lett.* **5**, 2635 (2005).

[56] H. von Berlepsch, S. Kirstein, R. Hania, A. Pugžlys, and C. Böttcher, *J. Phys. Chem. B* **111**, 1701 (2007).

[57] H. von Berlepsch, K. Ludwig, S. Kirstein, and C. Böttcher, *Chem. Phys.* **385**, 27 (2011).

[58] S. M. Vlaming, R. Augulis, M. C. A. Stuart, J. Knoester, and P. H. M. van Loosdrecht, *J. Phys. Chem. B* **113**, 2273 (2009).

[59] D. M. Eisele, C. W. Cone, E. A. Bloemsma, S. M. Vlaming, C. G. F. van der Kwaak, R. J. Silbey, M. G. Bawendi, J. Knoester, J. P. Rabe, and D. A. Vanden Bout, *Nat. Chem.* **4**, 655 (2012).

[60] A. Eisfeld and J. S. Briggs, *Chem. Phys.* **281**, 61 (2002).

[61] A. Eisfeld and J. S. Briggs, *Chem. Phys.* **324**, 376 (2006).

[62] D. M. Basko, A. N. Lobanov, A. V. Pimenov, and A. G. Vitukhnovsky, *Chem. Phys. Lett.* **369**, 192 (2003).

[63] M. Bednarz, V. A. Malyshev, and J. Knoester, *Phys. Rev. Lett.* **91**, 217401 (2003).

[64] D. J. Heijs, V. A. Malyshev, and J. Knoester, *Phys. Rev. Lett.* **95**, 177402 (2005).

[65] A. V. Malyshev, V. A. Malyshev, and J. Knoester, *Phys. Rev. Lett.* **98**, 087401 (2007).

[66] R. Augulis, A. V. Malyshev, V. A. Malyshev, A. Pugžlys, J. Knoester, and P. H. M. van Loosdrecht, *J. Phys. Chem. Lett.* **1**, 2911 (2010).

[67] S. J. Marrink, E. Lindahl, O. Edholm, and A. E. Mark, *J. Am. Chem. Soc.* **123**, 8638 (2001).

[68] M. E. Siwko, A. H. de Vries, A. E. Mark, A. Kozubek, and S. J. Marrink, *Biophys. J.* **96**, 3140 (2009).

[69] M. R. Wilson, *Chem. Soc. Rev.* **36**, 1881 (2007).

[70] F. Chami and M. R. Wilson, *J. Am. Chem. Soc.* **132**, 7794 (2010).

[71] Y. V. Malyukin, B. A. Gnap, A. V. Sorokin, and S. L. Yefimova, *Opt. Mater.* **34**, 2008 (2012).

[72] M. C. A. Stuart. University of Groningen, Groningen, The Netherlands. Personal communication, 2012.

[73] D. M. Eisele, J. Knoester, S. Kirstein, J. P. Rabe, and D. A. Vanden Bout, *Nature Nanotech.* **4**, 658 (2009).

[74] J. Sperling, A. Nemeth, J. Hauer, D. Abramavicius, S. Mukamel, H. F. Kauffmann, and F. Milota, *J. Phys. Chem. A* **114**, 8179 (2010).

[75] S. C. M. Gandini, E. L. Gelamo, R. Itri, and M. Tabak, *Biophys. J.* **85**, 1259 (2003).

[76] L. Kelbauskas, S. Bagdonas, W. Dietel, and R. Rotomskis, *J. Lumin.* **101**, 253 (2003).

[77] R. Rotomskis, R. Augulis, V. Snitka, R. Valiokas, and B. Liedberg, *J. Phys. Chem. B* **108**, 2833 (2004).

[78] A. Stradomska and J. Knoester, *J. Chem. Phys.* **133**, 094701 (2010).

[79] A. V. Sorokin, I. I. Filimonova, R. S. Grynyov, G. Y. Guralchuk, S. L. Yefimova, and Y. V. Malyukin, *J. Phys. Chem. C* **114**, 1299 (2010).

[80] C. Oostenbrink, A. Villa, A. E. Mark, and W. F. van Gunsteren, *J. Comput. Chem.* **25**, 1656 (2004).

[81] C. M. Breneman and K. B. Wiberg, *J. Comput. Chem.* **11**, 361 (1990).

[82] C. Cadena and E. J. Maginn, *J. Phys. Chem. B* **110**, 18026 (2006).

[83] H. J. C. Berendsen, J. P. M. Postma, W. F. van Gunsteren, and J. Hermans. „Interaction models for water in relation to protein hydration”. In: *Intermolecular Forces.* Ed. by B. Pullman. Dordrecht: Reidel, 1981.

[84] A. D. Becke, *J. Chem. Phys.* **98**, 5648 (1993).

[85] P. J. Stephens, F. J. Devlin, C. F. Chabalowski, and M. J. Frisch, *J. Phys. Chem.* **98**, 11623 (1994).

[86] Y. Shao and *et al.*, *Phys. Chem. Chem. Phys.* **8**, 3172 (2006).

[87] B. Hess, C. Kutzner, D. van der Spoel, and E. Lindahl, *J. Chem. Theory Comput.* **4**, 435 (2008).

[88] R. W. Hockney, *Methods Comput. Phys.* **9**, 136 (1970).

[89] B. Hess, H. Bekker, H. J. C. Berendsen, and J. G. E. M. Fraaije, *J. Comput. Chem.* **18**, 1463 (1997).

[90] I. G. Tironi, R. Sperb, P. E. Smith, and W. F. van Gunsteren, *J. Chem. Phys.* **102**, 5451 (1995).

[91] H. J. C. Berendsen, J. P. M. Postma, W. F. van Gunsteren, A. DiNola, and J. R. Haak, *J. Chem. Phys.* **81**, 3684 (1984).

[92] W. Humphrey, A. Dalke, and K. Schulten, *J. Molec. Graphics* **14.1**, 33 (1996).

[93] C. Duschl, W. Frey, and W. Knoll, *Thin Solid Films* **160**, 251 (1988).

[94] H. von Berlepsch, S. Kirstein, and C. Böttcher, *J. Phys. Chem. B* **108**, 18725 (2004).

[95] H. von Berlepsch, C. Böttcher, A. Ouart, C. Burger, S. Dähne, and S. Kirstein, *J. Phys. Chem. B* **104**, 5255 (2000).

[96] H. Yoshioka and K. Nakatsu, *Chem. Phys. Lett.* **11**, 255 (1971).

[97] J. J. Garcia-Celma, L. Hatahet, W. Kunz, and K. Fendler, *Langmuir* **23**, 10074 (2007).

[98] J. N. Israelachvili, *Intermolecular and Surface Forces* (Elsevier Academic Press, Waltham, 2011).

[99] M. E.-A. Madjet, F. Müh, and T. Renger, *J. Phys. Chem. B* **113**, 12603 (2009).

[100] C. Olbrich, J. Strümpfer, K. Schulten, and U. Kleinekathöfer, *J. Phys. Chem. B* **115**, 758 (2011).

[101] N. S. Ginsberg, Y.-C. Cheng, and G. R. Fleming, *Acc. Chem. Res.* **42**, 1352 (2009).

[102] M. Şener, J. Hsin, L. G. Trabuco, E. Villa, P. Qian, C. N. Hunter, and K. Schulten, *Chem. Phys.* **357**, 188 (2009).

[103] J. Adolphs, F. Müh, M. E.-A. Madjet, M. Schmidt am Busch, and T. Renger, *J. Am. Chem. Soc.* **132**, 3331 (2010).

[104] J. Singh and E. R. Bittner, *Phys. Chem. Chem. Phys.* **12**, 7418 (2010).

[105] C. Olbrich, T. l. C. Jansen, J. Liebers, M. Aghtar, J. Strümpfer, K. Schulten, J. Knoester, and U. Kleinekathöfer, *J. Phys. Chem. B* **115**, 8609 (2011).

[106] A. Goj and E. R. Bittner, *J. Chem. Phys.* **134**, 205103 (2011).

[107] T. A. Papadopoulos, L. Muccioli, S. Athanasopoulos, A. B. Walker, C. Zannoni, and D. Beljonne, *Chem. Sci.* **2**, 1025 (2011).

[108] F. Neese, *Wiley Interdiscip. Rev.: Comput. Mol. Sci.* **2**, 73 (2012).

[109] M. E. Madjet, A. Abdurahman, and T. Renger, *J. Phys. Chem. B* **110**, 17268 (2006).

[110] E. Sigfridsson and U. Ryde, *J. Comput. Chem.* **19**, 377 (1998).

[111] E. Sigfridsson, U. Ryde, and B. L. Bush, *J. Comput. Chem.* **23**, 351 (2002).

[112] S. Mukamel, *Principles of Nonlinear Optical Spectroscopy* (Oxford University Press, New York, 1995).

[113] Y. Jing, R. Zheng, H.-X. Li, and Q. Shi, *J. Phys. Chem. B* **116**, 1164 (2012).

[114] P. Atkins and J. de Paula, *Physical Chemistry* (Oxford University Press, Oxford, 2010).

[115] C. Olbrich, J. Strümpfer, K. Schulten, and U. Kleinekathöfer, *J. Phys. Chem. Lett.* **2**, 1771 (2011).

[116] V. May and O. Kühn, *Charge and Energy Transfer Dynamics in Molecular Systems* (Wiley-VCH, Weinheim, 2004).

[117] T. Renger, A. Klinger, F. Steinecker, M. Schmidt am Busch, J. Numata, and F. Müh, *J. Phys. Chem. B* **116**, 14565 (2012).

[118] H. Tamura, E. R. Bittner, and I. Burghardt, *J. Chem. Phys.* **127**, 034706 (2007).

[119] S. M. Vlaming, V. A. Malyshev, and J. Knoester, *J. Chem. Phys.* **127**, 154719 (2007).

[120] A. G. Dijkstra, T. l. C. Jansen, and J. Knoester, *J. Chem. Phys.* **128**, 164511 (2008).

[121] Y. V. Malyukin, A. V. Sorokin, S. L. Yefimova, and A. N. Lebedenko, *J. Lumin.* **112**, 429 (2005).

[122] Y. V. Malyukin, G. S. Katrich, and K. Kemnitz, *Mol. Cryst. Liq. Crys. A* **348**, 15 (2000).

[123] B. Kopainsky, J. K. Hallermeier, and W. Kaiser, *Chem. Phys. Lett.* **83**, 498 (1981).

[124] B. Kopainsky, J. Hallermeier, and W. Kaiser, *Chem. Phys. Lett.* **87**, 7 (1982).

[125] R. F. Pasternack, C. Fleming, S. Herring, P. J. Collings, J. dePaula, G. DeCastro, and E. J. Gibbs, *Biophys. J.* **79**, 550 (2000).

[126] Y. Kitahama, T. Yago, A. Furube, and R. Katoh, *Chem. Phys. Lett.* **457**, 427 (2008).

[127] W. West and S. Pearce, *J. Phys. Chem.* **69**, 1894 (1965).

[128] A. Nemeth, V. Lukes, J. Sperling, F. Milota, H. F. Kauffmann, and T. Mancal, *Phys. Chem. Chem. Phys.* **11**, 5986 (2009).

[129] T. Aida, E. W. Meijer, and S. I. Stupp, *Science* **335**, 813 (2012).

[130] H. Fidder, J. Knoester, and D. A. Wiersma, *J. Chem. Phys.* **98**, 6564 (1993).

[131] H. von Berlepsch and C. Böttcher, *J. Phys. Chem. B* **106**, 3146 (2002).

[132] G. Lamoureux and B. Roux, *J. Chem. Phys.* **119**, 3025 (2003).

[133] G. Lamoureux, E. Harder, I. V. Vorobyov, B. Roux, and A. D. MacKerell Jr., *Chem. Phys. Lett.* **418**, 245 (2006).

[134] J. C. Phillips, R. Braun, W. Wang, J. Gumbart, E. Tajkhorshid, E. Villa, C. Chipot, R. D. Skeel, L. Kalé, and K. Schulten, *J. Comput. Chem.* **26**, 1781 (2005).

[135] W. Jiang, D. J. Hardy, J. C. Phillips, A. D. MacKerell, K. Schulten, and B. Roux, *J. Phys. Chem. Lett.* **2**, 87 (2011).

[136] S. Miyamoto and P. A. Kollman, *J. Comput. Chem.* **13**, 952 (1992).

[137] B. Dammeier and W. Hoppe, *Acta Crystallogr. Sect. B* **27**, 2364 (1971).

[138] M. R. Philpott, *J. Chem. Phys.* **55**, 2039 (1971).

[139] F. C. Spano, *J. Chem. Phys.* **116**, 5877 (2002).

[140] A. Stradomska and P. Petelenz, *J. Chem. Phys.* **131**, 044507 (2009).

[141] T. l. C. Jansen and J. Knoester, *J. Phys. Chem. B* **110**, 22910 (2006).

[142] T. l. C. Jansen and J. Knoester, *Acc. Chem. Res.* **42**, 1405 (2009).

[143] J. Roden, A. Eisfeld, W. Wolff, and W. T. Strunz, *Phys. Rev. Lett.* **103**, 058301 (2009).

[144] R. Tempelaar, C. P. van der Vegte, J. Knoester, and T. l. C. Jansen, *J. Chem. Phys.* **138**, (2013).

[145] A. Nemkevich, H.-B. Bürgi, M. A. Spackman, and B. Corry, *Phys. Chem. Chem. Phys.* **12**, 14916 (2010).

[146] P. E. M. Lopes, B. Roux, and A. D. MacKerell Jr, *Theor. Chem. Acc.* **124**, 11 (2009).

[147] G. Scheibe and L. Kandler, *Naturwissenschaften* **24/25**, 412 (1938).

[148] A. Witkowski and W. Moffitt, *J. Chem. Phys.* **33**, (1960).

[149] R. L. Fulton and M. Gouterman, *J. Chem. Phys.* **41**, (1964).

[150] M. Andrzejak and P. Petelenz, *Chem. Phys.* **335**, 155 (2007).

[151] E. Daltrozzo, G. Scheibe, K. Geschwind, and F. Haimerl, *Photogr. Sci. Eng.* **18**, 441 (1974).

[152] G. Scheibe, F. Haimerl, and W. Hoppe, *Tetrahedron Lett.* **11**, (1970).

[153] J.-L. Brédas, J. E. Norton, J. Cornil, and V. Coropceanu, *Acc. Chem. Res.* **42**, 1691 (2009).

[154] G. D. Scholes and G. Rumbles, *Nature Mat.* **5**, 683 (2006).

[155] G. Hadziioannou and P. van Hutten, eds., *Semiconducting Polymers - Chemistry, Physics, and Engineering* (VCH, Weinheim, 1999).

[156] J. C. Bolinger, M. C. Traub, T. Adachi, and P. F. Barbara, *Science* **331**, 565 (2011).

[157] M. Bednarz, V. A. Malyshev, and J. Knoester, *J. Chem. Phys.* **117**, 6200 (2002).

[158] A. G. Redfield. „The Theory of Relaxation Processes”. In: *Advances in Magnetic Resonance.* Ed. by J. S. Waugh. Vol. 1. Academic Press, 1965.

[159] Y. Tanimura and R. Kubo, *J. Phys. Soc. Jpn.* **58**, 101 (1989).

[160] A. Ishizaki and G. R. Fleming, *J. Chem. Phys.* **130**, 234111 (2009).

[161] C. P. van der Vegte, A. G. Dijkstra, J. Knoester, and T. l. C. Jansen, *J. Phys. Chem. A* **117**, 5970 (2013).

[162] H. Torii, *J. Phys. Chem. A* **110**, 4822 (2006).

[163] A. G. Dijkstra, T. l. C. Jansen, R. Bloem, and J. Knoester, *J. Chem. Phys.* **127**, 194505 (2007).

[164] A. Paarmann, T. Hayashi, S. Mukamel, and R. J. D. Miller, *J. Chem. Phys.* **130**, 204110 (2009).

[165] A. V. Malyshev, V. A. Malyshev, and F. Domínguez-Adame, *Chem. Phys. Lett.* **371**, 417 (2003).

[166] A. V. Malyshev, V. A. Malyshev, and F. Domínguez-Adame, *J. Phys. Chem. B* **107**, 4418 (2003).

[167] S. M. Vlaming, V. A. Malyshev, A. Eisfeld, and J. Knoester, *J. Chem. Phys.* **138**, 214316 (2013).

[168] H. Haken and G. Strobl, *Z. Physik* **262**, 135 (1973).

[169] J. Lemaistre, *J. Lumin.* **76-77**, 437 (1998).

[170] J. Lemaistre, *Chem. Phys.* **246**, 283 (1999).

[171] A. Papoulis, *Probability, Random Variables, and Stochastic Processes* (McGraw-Hill, 1991).

[172] C. Leforestier et al., *J. Comput. Phys.* **94**, 59 (1991).

[173] J. A. Leegwater, J. R. Durrant, and D. R. Klug, *J. Phys. Chem. B* **101**, 7205 (1997).

[174] M. Shimizu, S. Suto, and T. Goto, *J. Chem. Phys.* **114**, 2775 (2001).

[175] P. Reineker. In: *Exciton Dynamics in Molecular Crystals and Aggregates.* Vol. 94. Springer Tracts in Modern Physics. Berlin / Heidelberg: Springer, 1982.

[176] K. Kitahara and J. W. Haus, *Z. Phys. B Con. Mat.* **32**, 419 (1979).

[177] H. Ezaki and F. Shibata, *Physica A* **192**, 124 (1993).

[178] P. Rebentrost, M. Mohseni, I. Kassal, S. Lloyd, and A. Aspuru-Guzik, *New J. Phys.* **11**, 033003 (2009).

[179] I. Kassal and A. Aspuru-Guzik, *New J. Phys.* **14**, 053041 (2012).

[180] K. Kassner, *Z. Phys. B Con. Mat.* **70**, 229 (1988).

[181] I. G. Scheblykin, O. Y. Sliusarenko, L. S. Lepnev, A. G. Vitukhnovsky, and M. Van der Auweraer, *J. Phys. Chem. B* **105**, 4636 (2001).

[182] I. M. Sokolov and J. Klafter, *Chaos* **15**, 026103 (2005).

[183] J. Klafter, A. Blumen, and M. F. Shlesinger, *Phys. Rev. A* **35**, 3081 (1987).

[184] R. Metzler and J. Klafter, *Phys. Rev. E* **61**, 6308 (2000).

[185] J. Knoester, *J. Chem. Phys.* **99**, 8466 (1993).

[186] H. Fidder, J. Knoester, and D. A. Wiersma, *J. Chem. Phys.* **95**, 7880 (1991).